Precise room temperature monitoring for accurate measurements of degree-scale cosmic microwave background anisotropy at POLARBEAR-2

Daiki Tanabe

December 10, 2020

Abstract

We developed precise temperature monitoring systems for warm instruments to correct temperature fluctuation for the POLARBEAR-2 experiment. POLARBEAR-2 is an astronomical observation project to measure polarization anisotropy of the cosmic microwave background (CMB). Testing the cosmic inflation, which is an essential hypothesis of the early universe before the hot Big Bang, is one of its main targets. We need to mitigate low-frequency noise during observation of the degree scales to detect inflationary signals in B-mode polarization of the CMB. In this thesis, we focused on temperature fluctuations of instruments as sources of low-frequency noise. First, we evaluated temperature coefficients between polarization signal and temperature of dominant components. Then we calculated requirements to temperature stability by comparison with the expected sensitivity of the detector array. We found that the temperature fluctuations of the mirrors and the readout electronics located in ambient temperature areas, which were neglected in the previous experiments, become comparable with POLARBEAR-2 and other sensitive experiments' statistical array sensitivity. To correct the temperature of the warm instruments to the required noise levels, we constructed precise temperature monitoring systems by combining low-noise multimeters and sensitive thermistors. We deployed our systems to the POLARBEAR-2 telescope system at the observational site in Chile and confirmed their measurement noise was below 1 mK$\sqrt{s}$ at 50 mHz that satisfies the requirements. Then we demonstrated temperature correction and evaluated bias induced by the error of temperature coefficient of each instrument. Finally, we made forecasts of tensor-to-scalar ratio r, a characteristic parameter of inflation models, after correction with various noise levels, sampling rates, and the number of corrected components. It supports the necessity of continuous temperature monitoring during observations and signals correction using the temperature data.

Acknowledgements

Accomplishment of this thesis owes to the support of many people. First I would like to thank Prof. Masashi Hazumi. He invited me to this exciting field of the experimental cosmology and taught me the way to logically pursue the rule of nature. He also gave me lots of invaluable opportunities to deepen my admiration to what we study—the world.

I am grateful to the POLARBEAR Collaboration, represented by Principal Investigator Prof. Adrian T. Lee. In the early time of my master's program, Prof. Yuki Inoue passionately invited me to the POLARBEAR-2 experiment. All my works owe to the state-of-the-art instruments and enthusiastic members gathering in this collaboration.

I would like to offer great thanks to the senior leaders. Prof. Masaya Hasegawa supported the whole of my study and life in High Energy Accelerator Research Organization (KEK). He energetically integrated the calibration team and provided me with a lot of idea of measurement and analysis. Prof. Haruki Nishino patiently taught me everything about data-acquisition systems of POLARBEAR-2. Prof. Yuji Chinone and Prof. Akito Kusaka always gave me critical advises in data analysis.

Discussions with Dr. Satoru Takakura was essential for me to understand temperature effect on detector signal. He told me the fertile experience in POLARBEAR and taught me how to treat 1/f noise. The complementary calculations done by Dr. Neil Goeckner-Wald also inspired me a lot. Prof. Tijmen de Haan helped me characterizing thermal response of the readout electronics with his expertise.

I am thankful to Dr. Kaori Hattori and Dr. Aritoki Suzuki, who introduced me the physics of transition-edge sensor.

Development and installation of the temperature monitoring system was greatly supported by Mr. Shuhei Kikuchi, who made great effort to design a compact system and to understand thermal environment around the mirror. Dr. Fredrick Takayuki Matsuda shared his experience about temperature measurement of the mirrors of POLARBEAR. Mr. John Groh instructed me a lot of techniques to mitigate the electrical noise. Prof. Nobuhiko Katayama helped me both in analysis and in the site work, in addition to his essential support with funding for all of us.

I appreciate the support of Mr. Satoru Igarashi, Mr. Calvin Tsai, Mr.

Nolberto Oyarce and Mr. José Cortes at the Chilean site. They totally maintained the site and helped me to deploy instruments to the telescope. I will never forget the red desolation and the bluest lagoons I saw in the Atacama highland.

My study and life were enriched by the closest staffs, postdocs and students in KEK CMB group including Prof. Osamu Tajima, Dr. Ryo Nagata, Dr. Daisuke Kaneko, Dr. Yuto Minami, Dr. Taketo Nagasaki, Dr. Shugo Oguri, Dr. Junya Suzuki, Dr. Shunsuke Honda, Mr. Yoshiki Akiba, Ms. Yuuko Segawa, Ms. Sayuri Takatori, Mr. Takako Hamada, Mr. Takuro Fujino, Mr. Haruaki Hirose, Mr. Hiroki Kutsuma and Mr. Akihiro Kato. I also appreciate the tender support of the secretaries, Mrs. Junko Yamada, Mrs. Keiko Imagawa and Mrs. Yumiko Imabayashi.

Prof. Makoto Yoshida and Prof. Masahiro Tsujimoto, who are reviewers of this thesis, gave me so many meaningful comments. I deeply appreciate their review.

This research was supported by the Short-term Research Abroad & Long-term Internship Program of The Graduate University for Advanced Studies (SOKENDAI).

I would like to offer special thanks to Mrs. Hazuki Kawamura and Mr. Yoshio Kawamura for their providing me with a cosy place to keep myself connected with the town community, and later, to write Ph.D. thesis. I enjoyed conversation wandering over physics, geology, education, mental health and coffee with them.

I hope it may not be ridiculous to show some regards to my non-human family for the delight they brought to me. My immortal cat Miké and my motorcycle Ms. Serika have traveled with me around everywhere.

At the end, I thank to my parents and grandparents for their indescribable supports for a long, long time.

Contents

List of Figures

List of Tables

1

Overview of the modern cosmology

The Cosmic Microwave Background (CMB) radiation has played important roles in the development of modern cosmology. CMB is the oldest radiation in this universe and is often called an afterglow of the Big Bang. Due to this feature, it is the most reliable probe to research the ancient universe.

In this chapter, we describe the framework of standard Big Bang cosmology and the generation of CMB. Then we introduce unsolved problems of Big Bang theory and inflation hypothesis as the solution.

Description in this chapter is mainly based on *The Primordial Density Perturbation* [15], *General relativity* [16] and *Cosmic Microwave Background Radiation* [2]. Unless otherwise stated, we use natural units of $c = \hbar = k_B = 1$.

1.1 Big Bang cosmology

1.1.1 Einstein's equation

Albert Einstein derived Einstein's equation by applying general relativity to space-time. General relativity claims that physical quantities are invariant with general coordinate transformation. It requires that tensor equations describe physical laws because any analytic map of vectors or dual vectors to physical quantity (scalar number) should be a summation of multilinear maps. Einstein's equation is derived as an extension of Poisson's equation to a tensor equation.

Relationship between gravitational potential $\phi(\vec{x})$ and mass density distribution $\rho(\vec{x})$ is classically expressed by Poisson's equation;

$$\Delta\phi(\vec{x}) = 4\pi G\rho(\vec{x}), \tag{1.1}$$

where ρ on the right side is replaced to energy-momentum tensor $T^{\mu\nu}$. It

requires the left side to be a second-order tensor, too. From general relativity, the second derivative of gravitational potential is written by metric $g^{\mu\nu}$, Ricci tensor $R^{\mu\nu}$ and scalar curvature R ;

$$R^{\mu\nu} + \alpha R g^{\mu\nu} + \Lambda g^{\mu\nu} = \kappa T^{\mu\nu} \tag{1.2}$$

when α, Λ, κ are coefficients to be determined by following procedures. Due to the conservation of energy and momentum,

$$\nabla_\nu T^{\mu\nu} = \nabla_\nu (R^{\mu\nu} + \alpha R) = 0, \tag{1.3}$$

where ∇_ν is a covariant derivative. α can be estimated from Bianchi identity. Bianchi identity is a symmetry of Riemann tensors;

$$\nabla_a R_{bcd}{}^e + \nabla_b R_{cad}{}^e + \nabla_c R_{abd}{}^e = 0. \tag{1.4}$$

Contracting this by metric action from the left side, we derive

$$\nabla_b (R^{ab} - \frac{1}{2} R g^{ab}) = 0. \tag{1.5}$$

So α should be $-1/2$. We rewrite $\left(R^{\mu\nu} - \frac{1}{2} R g^{\mu\nu}\right)$ as $G^{\mu\nu}$. κ is determined from the weak gravity limit. When we express weak gravitational field using Minkowski metric $\eta^{\mu\nu}$

$$g^{\mu\nu} = \eta^{\mu\nu} + h^{\mu\nu}, \quad |h^{\mu\nu}| \ll 1, \tag{1.6}$$

due to geodesic being in proportion to $\sqrt{-g^{00}}$, $\phi = -h^{00}/2$ in the weak gravity limit. To recover Newtonian gravity, κ should be $8\pi G$. So Einstein's equation is

$$G^{\mu\nu} + \Lambda g^{\mu\nu} = 8\pi G T^{\mu\nu} \tag{1.7}$$

If $T^{\mu\nu} = 0$, there is no gravitational source so $G^{\mu\nu}$ approaches to zero. Λ is called the cosmological constant, considered as the energy of vacuum. If only we solve Einstein's equation and derive metric $g^{\mu\nu}$, we can describe space-time geometry.

1.1.2 Cosmological principle and Friedmann equations

The central premise of modern cosmology is the "cosmological principle". The cosmological principle is an assumption that our universe is spatially homogeneous and isotropic. "Homogeneous" means there is no special observing point in our universe. "Isotropic" means there is no special direction of view in our universe. Thus, our universe's geometry should be a sphere of a certain dimension or a flat surface.

Friedmann and other scientists derived an analytic solution of Einstein's equation for metric under the cosmological principle. A Homogeneous and isotropic spherical spacetime results in the following metric:

$$ds^2 = -dt^2 + a^2(t)\left[\frac{dr^2}{1-Kr^2} + r^2(d\theta^2 + \sin^2\theta d\phi^2)\right] \tag{1.8}$$

This metric is called the Friedmann-Lemaître-Robertson-Walker (FLRW) metric. K is a curvature of spacetime, and its value is $+1$ or -1 or 0. $K = +1, -1, 0$ corresponds to closed, open, and flat universe. $a(t)$ is a scale factor, scaling the relative size of the universe. If $a(t)$ is doubled, the curvature of the universe becomes half, and the proper distance between two points is doubled. The appearance of time-dependent $a(t)$ indicates that the FLRW metric describes the expanding or shrinking universe. Conventionally we define $a(t)$ at present, written as a_0, to be 1. Substituting the FLRW metric into Einstein's equation, we can derive Friedmann equations. Since the Ricci tensor becomes a diagonal matrix, the energy-momentum tensor also becomes diagonal and is written as

$$T^{\mu\nu} = \begin{pmatrix} \rho & 0 & 0 & 0 \\ 0 & \frac{1-Kr^2}{a^2}P & 0 & 0 \\ 0 & 0 & \frac{1}{a^2\rho^2}P & 0 \\ 0 & 0 & 0 & \frac{1}{a^2\rho^2\sin^2\theta}P \end{pmatrix}, \tag{1.9}$$

where ρ and P can be considered as energy density and pressure of the ideal fluid. The FLRW metric implicitly assumes that the matter distribution of our universe is almost ideal fluid. Using these quantities, Friedmann equations are

$$\left(\frac{\dot{a}}{a}\right)^2 + \frac{K}{a^2} - \frac{\Lambda}{3} = \frac{8\pi G}{3}\rho, \tag{1.10}$$

$$2\frac{\ddot{a}}{a} + \left(\frac{\dot{a}}{a}\right)^2 + \frac{K}{a^2} - \Lambda = -8\pi G P. \tag{1.11}$$

Current observations show that the universe is almost flat. Substituting $K = 0$ and $\Lambda = 0$ to Eq. (1.10), we obtain

$$\left(\frac{\dot{a}}{a}\right)^2 = \frac{8\pi G}{3}\rho. \tag{1.12}$$

Friedmann equations describe the evolution of the whole universe itself.

1.1.3 Hubble-Lemaître law

Here we denote the Hubble rate

$$H(t) \equiv \frac{\dot{a}}{a} \tag{1.13}$$

and write Hubble rate at present as H_0. It is called the Hubble constant.

In 1927, Lemaître predicted that galaxies would go away from the earth with the velocity in proportion to their distance if the universe is expanding. Hubble confirmed it by observing Cepheid variables in 1929. For a celestial body far enough from the earth, it goes away with the velocity

$$v = H(t)r \tag{1.14}$$

where r is the distance. This relationship is called the Hubble-Lemaître law. Since r changes by the expansion of the universe, we can write

$$r = a(t)\boldsymbol{x}, \tag{1.15}$$

where the $\boldsymbol{x}$ is called the comoving coordinate and does not change by the scale.

The Hubble constant H_0 is determined by observations and expressed as

$$H_0 = 100\ h\ \text{km s}^{-1}\text{Mpc}^{-1}, \tag{1.16}$$

where $h = 0.6774 \pm 0.0046$.
The inverse of H_0 is called the Hubble time,

$$H_0^{-1} = 3.086 \times 10^{17} h^{-1}\ \text{s} = 9.778 \times 10^9 \text{h}^{-1}\ \text{years} \approx 1.4 \times 10^{10}\ \text{years} \tag{1.17}$$

where a year is 365.25 days $= 3.156 \times 10^7$ seconds. The Hubble time gives an approximate age of the universe.

The product of the light velocity and the Hubble time is the Hubble length,

$$cH_0^{-1} = 2998\ h^{-1}\ \text{Mpc} \approx 4282.86\ \text{Mpc}. \tag{1.18}$$

The Hubble length gives an approximate observable diameter of the universe.

When the space expands, the wavelength of the light also expands. This is called redshift and written as

$$1 + z \equiv \frac{\lambda_0}{\lambda_1} = \frac{a_0}{a}, \tag{1.19}$$

where λ_0 is the observed wavelength today and λ_1 is that at a certain period in the past. If we assume that expansion of wavelength is only due to expansion of space, it can be expressed with the scale $a(t)$. The value of z is zero at present and the larger z indicates the older time.

1.1.4 Big Bang theory

Applying energy conservation $\nabla_\mu T^{\mu 0} = 0$ to the energy-momentum tensor in Eq. (1.9) gives

$$\dot{\rho} + 3\frac{\dot{a}}{a}(\rho + P) = 0 \tag{1.20}$$

This also can be derived from Eq. (1.10) and Eq. (1.11). we can consider $\beth = P/\rho$ to be an equation of state. We obtain $\beth = 1/3$ for relativistic radiation from the Stefan-Boltzmann law, $\beth = 0$ for non-relativistic matter, and $\beth = -1$ for the cosmological constant. If $\beth$ is a constant, Eq. (1.20) can be integrated to be

$$\rho = \rho_0 \left(\frac{\dot{a}}{a}\right)^{3(1+\beth)}, \tag{1.21}$$

where ρ_0 is energy density at present. From Eq. (1.12), we obtain $\rho_0 = \frac{3H_0^2}{8\pi G} \simeq 1.87 \times 10^{-26} h^2$ kg/m^{-3}. It is very close to the energy density of the completely flat universe called critical density. The energy density of radiation decreases as a^{-4} and that of matter as a^{-3}. While our universe is matter-dominant at present, this equation suggests once it was radiation-dominant. Adding expansion discovered by Hubble, we are led to an idea that the universe was a tiny, hot, and high-density "fireball" in the past. This ancient state and the following expansion is called the Big Bang.

The Big Bang's observational pieces of evidence are recession velocities of galaxies, the Big Bang nucleosynthesis, and the Cosmic Microwave Background (CMB). The hot and high-density universe is necessary to generate H, He, Li and unstable nuclei, which became materials of heavier elements. Furthermore, the Big Bang theory predicts that the CMB is black body radiation. In the hot and high-density universe, radiation is dominant. However, the energy density of radiation decreases with a^{-4} as the universe expands and at a certain period realizes thermal equilibrium with the matter. The energy distribution of photons follows the Planck distribution. Since electrons scatter these photons, they cannot go straight until electrons are trapped by protons and construct neutral hydrogen atoms. When the universe cools down enough, the photons become to be able to run freely. This radiation is the CMB. In 1994, the COBE satellite reported that the CMB monopole and dipole components precisely obey the Planck distribution (Figure 1.1). The CMB is observed as black body radiation of 2.725 K today, but it should have been much hotter in the past. As the universe expands, the number density of photons decreases by a^{-3}, and radiation temperature also decreases by a^{-1}.

There were long arguments between the Big Bang theory and the steady-state theory. Traditionally, the universe was considered to be static with neither a beginning nor an end. The steady-state theory claimed that new matters were generated one after another to compensate for the decrease of matter density in the expanding universe. However, the pieces of evidence mentioned above proved the validity of the Big Bang theory.

To see the outline of the evolution of the universe, we check the time dependence of $a(t)$. Using the Friedmann equation (1.12), we obtain

$$\frac{H^2(t)}{H_0^2} = \frac{\rho}{\rho_0} = \frac{1}{\rho_0}\left[\frac{\rho_{m0}}{a^3} + \frac{\rho_{r0}}{a^4}\right], \tag{1.22}$$

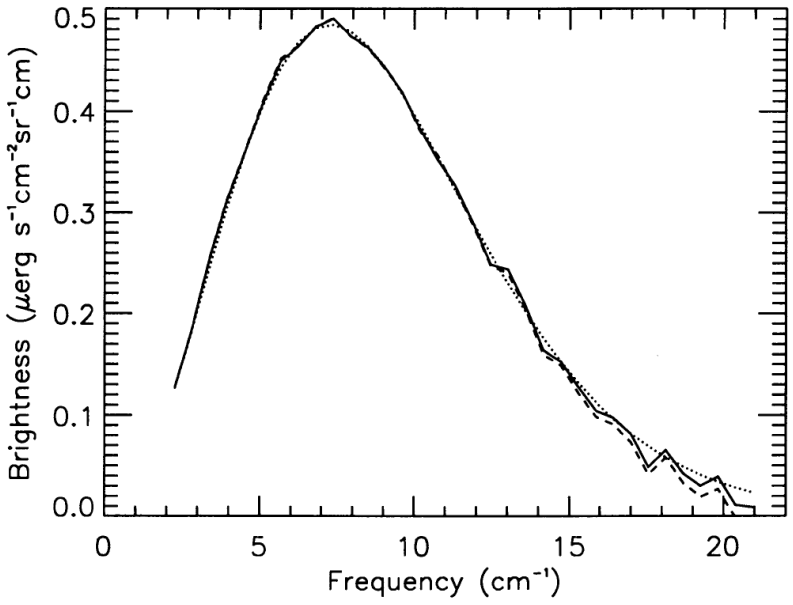

Figure 1.1: Distribution of the CMB monopole component [1]. *Solid line*: spectrum measured by far infrared absolute spectrophotometer (FIRAS) loaded on the COBE satellite. *Dotted line*: fit of derivative of Planck distribution. *Dashed line*: predicted spectrum by csc |b| Galactic spatial model.

where ρ_{m0} and ρ_{r0} are the energy densities of matter and radiation at present. This derivative equation leads to

$$\begin{cases} a \propto t^{\frac{2}{3}}, & \dot{a} \propto t^{-\frac{1}{3}}, & \ddot{a} \propto -t^{-\frac{4}{3}} & \text{(matter only)} \\ a \propto t^{\frac{1}{2}}, & \dot{a} \propto t^{-\frac{1}{2}}, & \ddot{a} \propto -t^{-\frac{3}{2}} & \text{(radiation only)} \end{cases} \tag{1.23}$$

Namely, the universe, which contains only matter and radiation, keeps decelerated expansion. We know, however, that the expansion of our universe is accelerated. Precise tests of the Hubble-Lemaître law using type Ia supernovae confirmed accelerated expansion. It is consistent with the acceleration due to the cosmological constant.

1.2 ΛCDM model and evolution of the universe

Components of the universe

The current standard cosmological theory is called the ΛCDM model. It includes the cosmological constant Λ and cold dark matter (CDM). The cosmological constant is also called dark energy. Cold dark matter is an

Parameter	TT, TE, EE+lowP+lensing+ext.
$\Omega_B h^2$	0.02230 ± 0.00014
$\Omega_{DM} h^2$	0.1188 ± 0.0010
Ω_Λ	0.6911 ± 0.0062
Δ_R^2	$2.142 \pm 0.049 \times 10^{-9}$
n_s	0.9667 ± 0.0040
τ	0.066 ± 0.012

Table 1.1: Six parameters of the ΛCDM estimated at 68% C.L. from CMB power spectra measured by Planck, in combination with gravitational lensing and external data; baryon acoustic oscillation (BAO), joint light-curve analysis (JLA) of type Ia supernovae and the Hubble constant [11].

unidentified matter that is indirectly observed. It interacts with other particles only through gravity and weak interaction. The rotation velocity of spiral galaxies was the first clue that suggested the existence of dark matter.

Now we normalize energy density ρ by critical density $\rho_0 \equiv 3H^2/8\pi G$ and make dimensionless parameters,

$$\Omega_r \equiv \frac{\rho_r}{\rho_0}, \quad \Omega_m \equiv \frac{\rho_m}{\rho_0}, \quad \Omega_\Lambda \equiv \frac{\Lambda}{8\pi G \rho_0}, \quad \Omega_K \equiv -\frac{K}{H^2}. \tag{1.24}$$

These are called density parameters. Then the Friedmann equation (1.10) under $K = 0$ is written as

$$H^2(z) = H_0^2 \left[\Omega_{r,0}(1+z)^4 + \Omega_{m,0}(1+z)^3 + \Omega_{\Lambda,0} + \Omega_{K,0}(1+z)^2 \right], \tag{1.25}$$

where Ω_m consists of baryon Ω_B and cold dark matter Ω_{DM}. These are parts of six parameters of the ΛCDM model. Parameters Ω_B, Ω_{DM} and Ω_Λ are related to the components of the universe. Curvature perturbation Δ_R^2 and spectral index n_s represent initial conditions of the universe, predicted by inflation models. Optical depth τ is a parameter of reionization. Current values of them are shown in Table 1.1.

Here we discuss three epochs in the evolution of the universe; matter-radiation equality, recombination, and reionization.

1.2.1 Matter-radiation equality

Matter-radiation equality is defined as an epoch when the energy density of radiation and matter become equal, i.e.

$$1 = \frac{\rho_r}{\rho_m} = \frac{\rho_{r0}(1+z_{eq})^4}{\rho_{m0}(1+z_{eq})^3} = \frac{\Omega_r}{\Omega_m}(1+z_{eq}). \tag{1.26}$$

Here Ω_r can be calculated with a grand canonical ensemble;

$$\rho_r = g \int \frac{d^3p}{(2\pi\hbar)^3} \, pc \frac{1}{e^{\frac{pc}{k_B T}} \pm 1} = g \frac{\pi^2}{30} \frac{(k_B T)^4}{\hbar^5 c^3} \times \begin{cases} 1 & \text{(boson)} \\ 7/8 & \text{(fermion)} \end{cases} \tag{1.27}$$

in the relativistic limit, and g is a degree of freedom of relativistic particles. For photons it means polarization states, i.e. $g = 2$. For neutrinos, we have to consider generations, helicity and entropy change by annihilations of electron and positron. The total effective degree of freedom, including photons and relativistic neutrinos, is

$$g_* = 2 + 3 \cdot 2 \cdot \left(\frac{4}{11}\right)^{\frac{4}{3}} \cdot \frac{7}{8} \simeq 3.36. \tag{1.28}$$

Using this $g_* = 3.36$ and $T = 2.725$ K at prsent, Eq. (1.27) leads $\rho_r \simeq 7.74 \times 10^{-31}$ kg/m^3. Then we obtain Ω_r by normalizing ρ_r by the critical density ρ_0 as

$$\Omega_r = \frac{\rho_r}{\rho_0} = 4.14 \times 10^{-5} \; h^{-2}. \tag{1.29}$$

Here we used $c = 3 \times 10^8$ m/s and $h = 6.63 \times 10^{-34}$ J·s explicitly in order to make the unit the same as ρ_0.

On the other hand, the present energy density is observed to be $\Omega_m \simeq 0.315 \pm 0.007$ [11]. Therefore the redshift at matter-radiation equality is

$$z_{eq} \simeq 1 + z_{eq} = \frac{\Omega_m}{\Omega_r} \simeq 3.5 \times 10^3. \tag{1.30}$$

1.2.2 Recombination

When the universe cools down below the bound-state energy of the hydrogen's ground state, namely 13.6 eV, electrons are trapped by protons. However, photons are still scattered by electrons because the number of photons is much larger than electrons and high energy photons ionize the neutral hydrogen atoms again. Photons start to travel freely when the universe becomes cooler. This epoch of hydrogen atoms is called recombination, and the release of photons is called decoupling. These two are altogether called the last-scattering epoch.

To discuss the interaction between photon, electron and proton, we introduce optical depth

$$\tau \equiv \sigma_T c \int_t^{t_0} n_e(t) dt, \tag{1.31}$$

where σ_T is the Thomson scattering cross-section and $n_e(t)$ is the number density of free electrons. We induced c explicitly for physical calculation. The probability that a CMB photon travels freely since t to t_0 is $P(t) = e^{-\tau(t)}$, with $P(t_0) = 1$.

We define ionization fraction $\chi(z) \equiv n_e/(n_p + n_{1s})$, where n_p and n_{1s} is the number density of protons and neutral hydrogen atoms at the ground state. Using $n_e(z) = n_{e,0}(1+z)^3$, the optical depth is written as a function of z,

$$\tau(z) = 0.75(n_{p,0} + n_{1s,0})\sigma_T c \int_0^z (1+z')^2 \frac{dz'}{H(z')}\chi(z'). \tag{1.32}$$

We used $dz = (1+z)H(z)dt$ and $n_{e,0} = 0.75(n_{p,0} + n_{1s,0})$.

When electrons, protons and neutral hydrogen atoms at the ground state are in ionization equilibrium $p^+ + e^- \rightleftarrows H + \gamma$, the relationship between their number density is expressed by Saha's equation,

$$\frac{n_p n_e}{n_{1s}} = \frac{g_p g_e}{g_{1s}} \left(\frac{m_p}{m_H}\frac{m_e k_B T}{2\pi\hbar^2}\right)^{\frac{3}{2}} \exp\left(-\frac{13.6}{k_B T}\right), \tag{1.33}$$

where $g_p = 2$, $g_e = 2$, $g_{1s} = 4$ are numbers of spin states. We can rewrite this with χ as

$$\frac{\chi^2}{1-\chi} = \frac{1}{n_p + n_{1s}} \left(\frac{m_e k_B T}{2\pi\hbar^2}\right)^{\frac{3}{2}} \exp\left(-\frac{13.6}{k_B T}\right). \tag{1.34}$$

When we use the ratio of the number density of baryons and photons $\eta = n_B/n_\gamma = 2.73 \times 10^{-8}\Omega_B h^2$ and $n_\gamma = 411(1+z)^3$ cm^{-3}, Eq. (1.34) is

$$\frac{\chi^2}{1-\chi} = \frac{2.53 \times 10^6}{\eta} \tilde{T}^{-\frac{3}{2}} \exp\left(-\frac{1}{\tilde{T}}\right), \tag{1.35}$$

where $\tilde{T} \equiv k_B T/13.6$ eV. Solving Eq. (1.35), we obtain

$$\chi(T) = \frac{2}{1 + \sqrt{1 + 1.58 \times 10^{-6}\eta \tilde{T}^{3/2} \exp\left(-1/\tilde{T}\right)}} \tag{1.36}$$

Substituting $\Omega_B h^2 = 0.022$ and $\chi = 0.5$, we obtain $T \approx 3700$ K.

The ratio between the mean free time of CMB photons and the Hubble time is

$$\frac{H}{\sigma_T n_e c} = \frac{H_0\sqrt{\Omega_M(1+z)^3}}{\sigma_T c \cdot 0.75\chi(z)} \tag{1.37}$$

At $z \approx 1100$, which corresponds to $T \approx 3000$ K, this ratio becomes to 1 and CMB starts to travel freely. This epoch is the last-scattering surface.

More precise last-scattering time is calculated using visibility function

$$g(t) \equiv \frac{dP}{dt} = -\dot{\tau}(t)e^{-\tau(t)} = \sigma_T n_e(t) c e^{-\tau(t)}, \tag{1.38}$$

which is the probability that a CMB photon is scattered in the time interval dt and since then travels freely until today. The redshift z which gives the maximum value of g is the last-scattering time. If we consider the difference from equilibrium caused by the universe expansion, the last-scattering time is $z = 1090$ and $T = 2974$ K.

1.2.3 Reionization

In spite of the recombination, most hydrogens are ionized again at low redshift. This is called reionization and makes observations of distance galaxies challenging.

When we consider matter and cosmological constant, Eq. (1.25) is

$$H^2 = H_0^2 \left[\Omega_{m,0}(1+z)^3 + (1-\Omega_{m,0})\right]. \tag{1.39}$$

On the other hand, Eq. (1.24) leads to

$$\Omega_m(z)(1+z)^{-3}H^2 = \Omega_{m,0}H_0^2. \tag{1.40}$$

Combining Eq. (1.39) and (1.40), we obtain

$$\Omega_m(z) = \Omega_{m,0}\frac{(1+z)^3}{1-\Omega_{m,0}+(1+z)^3\Omega_{m,0}}. \tag{1.41}$$

Using Eq. (1.40), optical depth τ in Eq. (1.32) is written as

$$\tau(z) = \tau^* \int_0^z (1+z')^{1/2}\sqrt{\frac{\Omega_m(z')}{\Omega_{m,0}}}\chi(z')dz', \tag{1.42}$$

where τ^* is

$$\tau^* = 0.75\frac{3H_0\Omega_B\sigma_T c}{8\pi G m_b}. \tag{1.43}$$

Here we used $\Omega_B = (8\pi G/3H_0^2) \times m_B n_{B,0}$.

We assume an instantaneous reionization, which has $\chi(z) = 1$ for $z < z_{\rm ion}$ and $\chi(z) = 0$ otherwise. Using Eq. (1.41), integrating Eq. (1.42) gives

$$\begin{aligned}\tau &\simeq \frac{2\tau^*}{3\Omega_{m,0}}\left[\left(1-\Omega_{m,0}+\Omega_{m,0}(1+z_{\rm ion})^3\right)^{1/2} - 1\right] \\ &\simeq 2.2\times 10^{-3}(1+z_{\rm ion})^{3/2}.\end{aligned} \tag{1.44}$$

Substituting $\tau = 0.066$, we obtain $z_{\rm ion} \simeq 9$. The probability that a CMB photon is scattered again at the reionization is $1-e^{-\tau} \simeq \tau$ when τ is small.

1.3 Inflation hypothesis

1.3.1 Accelerating expansion

The Big Bang cosmology and ΛCDM model successfully explain many observational data but there are some mysteries beyond the ΛCDM model. Frequently-mentioned mysteries are the horizon problem, the flatness problem, the monopole problem and the problem of the origin of the density perturbation.

The horizon problem appeared with highly isotropic nature of CMB. The temperature of CMB would be isotropic only in the area which once was in the causal relation. The size of the area is "particle horizon", defined as a distance in which light can travel in time t;

$$d_p(t) \equiv a(t) \int_0^t \frac{dt'}{a(t')}. \tag{1.45}$$

Points far apart beyond the particle horizon can not have causal relation. In the decelerated expanding universe, assuming $\ddot{a} < 0$, namely, $a \propto t^n$ $(0 < n < 1)$, we obtain

$$d_p(t) = \frac{t}{1-n} \propto \frac{n}{1-n}\frac{a}{\dot{a}} = \frac{n}{1-n} H^{-1}(t). \tag{1.46}$$

This shows that the particle horizon was smaller in the past than now. However, the fluctuation of CMB is too small over all directions. Now our universe is in an accelerated expansion but the acceleration period is still too short to explain this. This puzzle is called the horizon problem.

The flatness problem claims the universe is too flat. The density parameter of curvature, measured by Planck [11], is $\Omega_K = 0.0008^{+0.0040}_{-0.0039}$. We can obtain its time development from Eq. (1.25), i.e. $\Omega = -K/H(t)^2$. Since it increases as decelerated expansion, it should have been moreover small in the past. This problem is also called fine-tuning problem.

The monopole problem is the absence of magnetic monopoles. When a symmetry of three-component scalar field such as $SO(3)$ or $SO(3) \times SO(2) \times U(1)$ (GUT) is violated, magnetic monopoles are generated as topological defects. It is predicted that the energy density of magnetic monopoles should be more than CDM but there is no magnetic monopole observed.

Inflation hypothesis is a solution to solve these problems of the Big Bang cosmology. It assumes accelerated expansion,

$$\ddot{a} > 0 \tag{1.47}$$

in the primordial universe. It is equivalent to

$$\frac{d}{dt}\frac{1}{aH} < 0, \tag{1.48}$$

which means that the comoving Hubble length decreases. This is also written as

$$-\frac{\dot{H}}{H^2} < 1, \tag{1.49}$$

which means that H varies slowly on the Hubble timescale on the assumption that $\dot{H} < 0$. If $|\dot{H}| \ll H^2$, H is approximately a constant during inflation and the expansion is almost exponential, $a \propto e^{Ht}$. A universe with constant

H is called a de Sitter universe. Another equivalent formula is derived by Eq. (1.10) and Eq. (1.11) as

$$\rho + 3P < 0 \tag{1.50}$$

where $\Lambda = 0$. The negative pressure is the feature of inflation. For exponential expansion, $H(t)$ has to be constant.

The horizon problem is explained that the whole universe was within the particle horizon during inflation. It makes it natural that the CMB has uniform temperature in any angle. The flatness problem is solved by the curvature density parameter Ω_K decreasing due to constant $H(t)$ and increasing $a(t)$. The particle problem is solved by re-heating after inflation. Inflaton field, which is a quantum field to cause inflation, collapses after inflation and generates entropy to re-heat the universe. The origin of density perturbation is regarded as a quantum perturbation of inflaton field.

At the end of the inflation, the whole energy density is locked in the inflaton field. Phase defections and curvature perturbation are diluted. This energy density must be released to cause Big Bang. This process is called reheating. Reheating lasts until the whole energy changes to the radiation in the thermal equilibrium. The temperature at the end of the reheating is called reheating temperature.

1.3.2 Inflaton field

Here we analyze the dynamics of inflaton field. We assume "canonically normalized" scalar fields dominated by Einstein's gravity with the Lagrangian density,

$$\mathcal{L} = -\frac{1}{2}\sum_n^N \partial^\mu \phi_n \partial_\mu \phi_n - V(\phi_1 \cdots \phi_N) \tag{1.51}$$

where $V(\phi_1 \cdots \phi_N)$ is a potential function of all fields. From the Euler-Lagrangian equation, the equations of fields are

$$-\Box\phi_n + \frac{\partial V}{\partial \phi_n} = 0. \tag{1.52}$$

Assuming FLRW metric and homogeneous fields, they are

$$\ddot{\phi_n} + 3H\dot{\phi_n} + V'(\phi) = 0. \tag{1.53}$$

The energy-momentum tensor is derived as a Noether current of the fields.

$$\begin{aligned} T^\mu_\nu &= -\frac{\partial \mathcal{L}}{\partial(\partial_\mu \phi_n)}\partial_\nu \phi_n + \delta^\mu_\nu \mathcal{L} - \frac{\partial \mathcal{L}}{\partial(\partial_\mu \phi_n)}\delta\phi_n \\ &= \sum_n^N \partial^\mu \phi_n \partial_\mu \phi_n - \delta^\mu_\nu \left(\frac{1}{2}\sum_n^N \partial^\alpha \phi_n \partial_\alpha \phi_n + V(\phi_1 \cdots \phi_N)\right) \end{aligned} \tag{1.54}$$

For homogeneous fields, energy density and pressure are

$$\begin{aligned} \rho = T^{00} = g^{00}T^0_0 = \frac{1}{2}\sum_n^N \dot{\phi_n}^2 + V, \\ P = T^{11} = T^{22} = T^{33} = \frac{1}{2}\sum_n^N \dot{\phi_n}^2 - V. \end{aligned} \tag{1.55}$$

If the variation of the field is slight ($V < -\sum \dot{\phi_n}^2/2$), the inflationary condition $P < -\rho/3$ is satisfied.

Here we consider single-field inflation and call ϕ inflaton. When we substitute ρ into Friedmann's equation Eq. (1.12), we obtain

$$3M_{\rm Pl}^2 H^2 = V(\phi) + \frac{1}{2}\dot{\phi}^2. \tag{1.56}$$

When we combine Eq. (1.56) and Eq. (1.53), we obtain

$$2M_{\rm Pl}^2 \dot{H} = -\dot{\phi}^2. \tag{1.57}$$

1.3.3 Slow-roll inflation

Here we assume

$$\frac{|\dot{H}|}{H^2} \ll 1, \tag{1.58}$$

which means that inflation is almost exponential. Considering Eq. (1.56) and Eq. (1.57), this condition also means $\dot{\phi} \ll 1$ and $3M_{\rm Pl}^2 H^2 \simeq V$. Taking a first time derivative of the exponential condition, we obtain an approximation

$$3H\dot{\phi} \simeq -V'(\phi). \tag{1.59}$$

Comparing from Eq. (1.53), this corresponds to $|\ddot{\phi}| \ll 3H|\dot{\phi}|$, which means $\dot{\phi}$ varies little for Hubble time.

Taking a second time derivative of the exponential condition, we obtain an approximation

$$\ddot{\phi} \simeq -\frac{\dot{H}}{H^2}\dot{\phi} - \frac{V''\dot{\phi}}{3H}. \tag{1.60}$$

We introduce slow-roll parameters ϵ and η to formulate slow-roll approximation. From Eq. (1.53), Eq. (1.59) and Eq. (1.59), we define slow-roll parameters

$$\epsilon(\phi) \ll 1 \quad \text{where} \quad \epsilon \equiv \frac{M_{\rm Pl}^2}{2}\left(\frac{V'}{V}\right)^2, \tag{1.61}$$

$$|\eta(\phi)| \ll 1 \quad \text{where} \quad \eta \equiv M_{\rm Pl}\frac{V''}{V} \simeq \frac{V''}{3H^2}. \tag{1.62}$$

We call $\epsilon(\phi) \ll 1$ and $|\eta(\phi)| \ll 1$ as flatness conditions.

1.3.4 Primordial perturbations

When we assume inflaton, it is natural to concern its quantum filed perturbations. These perturbations are considered as origins of matter density anisotropy, curvature perturbation and primordial gravitational waves.

The Einstein-Hilbert action of single scalar field is

$$S = \int d^4x\sqrt{-g}\left(\frac{1}{2}M_{\rm Pl}^2 R - \frac{1}{2}\partial_\mu\phi\partial^\mu\phi - V(\phi)\right) \tag{1.63}$$

Substituting metric perturbation into this action gives the power spectrum of each perturbation.

The perturbed metric from flat timespace can be written by scalar, vector and tensor component as

$$\begin{aligned} ds^2 = a^2(\eta)\Big\{&-(1+2A)d\eta^2 + 2(\nabla_i B - C_i)d\eta dx^i \\ &+ \left[(1+2D)\delta_{ij} + 2\nabla_i\nabla_j E + 2\nabla_i F_j + h_{ij}\right]dx^i dx^j\Big\}. \end{aligned} \tag{1.64}$$

Here we use conformal time

$$\eta = \int \frac{1}{a}dt. \tag{1.65}$$

In order to keep each components independent, we impose zero-divergence condition $\nabla^i C_i = \nabla^i F_i = 0$ and transverse-traceless condition

$$\nabla^\mu h_{\mu\nu} = 0, \quad h^\mu{}_\mu = 0. \tag{1.66}$$

Since $h_{\mu\nu}$ has two degree of freedom in the space part under the transverse-traceless condition, we can separate it into two components like $h_{ij} = h_+\epsilon_{ij}^+ + h_\times\epsilon_{ij}^\times$. Here ϵ_{ij}^+ and $\epsilon_{ij}^\times$ are unit polarization matrices which have the following orthogonal relationship,

$$\epsilon_{ij}^S(\mathbf{k})\epsilon_{ij}^{S'}(\mathbf{k}')^* = 2\delta_{SS'}\delta(\mathbf{k}+\mathbf{k}')\mathbf{I}, \tag{1.67}$$

where $\mathbf{I}$ is the third-dimensional unit matrix.

When we transform each coordinate variable as $t \to t+\alpha$, $x^i \to x^i + \delta^{ij}\partial_j\beta$, scalar and tensor components change their values. Therefore A, B, D, E and h_{ij} are not gauge invariant. We can construct gauge invariant quantities as

$$\Phi \equiv A - \frac{1}{a}\left[a(E'-B)\right]', \quad \Psi \equiv -D + aH(E'-B). \tag{1.68}$$

Φ can be translated to the gravitational potential and Ψ is the curvature perturbation. Another two gauge invariant quantities are possible.

$$\mathcal{R} \equiv \Psi - \frac{H}{\bar\rho + \bar P}\delta q \quad \left(\delta q \equiv a(\rho+P)(v+B),\ v^\mu = \frac{\partial x^\mu}{\partial t}\right), \tag{1.69}$$

$$\zeta \equiv -\Psi - \frac{H}{\dot{\phi}}\delta\rho. \tag{1.70}$$

This $\mathcal{R}$ is equivalent to Ψ under comoving gauge $\delta\phi = 0$, and $\zeta = \Psi$ under uniform density gauge $\delta\rho = 0$ or superhorizon limit $k \ll aH$.

If we adopt comoving gauge, perturbation of space components of metric are

$$ds^2 = a^2(\eta)\left[(1-2\mathcal{R})\delta_{ij} + h_{ij}\right]dx^i dx^j. \tag{1.71}$$

Scalar power spectrum

First we calculate the power spectrum of scalar perturbation. Substituting Eq. (1.71) into Eq. (1.63) and taking second perturbation of $\mathcal{R}$ leads

$$S = \frac{1}{2}\int d\eta d^3x a^2 Q_s \left[\dot{\mathcal{R}}^2 - c_s^2(\partial\mathcal{R})^2\right], \tag{1.72}$$

$$Q_s \equiv \frac{\dot{\phi}}{2H^2}\left(\frac{\partial\mathcal{L}}{\partial X} + 2X\frac{\partial^2\mathcal{L}}{\partial X^2}\right), \quad c_s^2 \equiv \frac{\frac{\partial\mathcal{L}}{\partial X}}{\frac{\partial\mathcal{L}}{\partial X} + 2X\frac{\partial^2\mathcal{L}}{\partial X^2}}, \quad X \equiv -g^{\mu\nu}\partial_\mu\phi\partial_\nu\phi. \tag{1.73}$$

Here c_s means the propagation velocity of the scalar perturbation. For the most potentials which do not have the multiple power of the kinetic term, $c_s = 1$. Next we quantize $\mathcal{R}$. We can define Fourier expansion and creation-annihilation operators as

$$\mathcal{R}(\eta, \mathbf{x}) = \frac{1}{(2\pi)^3}\int d^3\mathbf{k}\mathcal{R}(\eta, \mathbf{k})e^{i\mathbf{k}\cdot\mathbf{x}}, \tag{1.74}$$

$$\mathcal{R}(\eta, \mathbf{k}) = u(\eta, \mathbf{k})a(\mathbf{k}) + u^*(\eta, -\mathbf{k})a(-\mathbf{k}). \tag{1.75}$$

Note that here a is an annihilation operator, not a scale factor. These creation-annihilation operators satisfy the following commutation relationship,

$$\left[a(\mathbf{k}), a^\dagger(\mathbf{k}')\right] = (2\pi)^3\delta^{(3)}(\mathbf{k}-\mathbf{k}'), \quad \left[a(\mathbf{k}), a(\mathbf{k}')\right] = \left[a^\dagger(\mathbf{k}), a^\dagger(\mathbf{k}')\right] = 0. \tag{1.76}$$

Substituting Eq. (1.74) and Eq. (1.75) into Eq. (1.72) gives the equation of mode function

$$u'' + \frac{(a^2Q_s)'}{a^2Q_s}u' + c_s^2k^2u = 0. \tag{1.77}$$

The mode function defined in Eq. (1.74) and Eq. (1.75) satisfies this equation. We can change the variable to simplify the equation as

$$v \equiv zu, \quad z \equiv a\sqrt{2Q_s}, \tag{1.78}$$

$$v'' + \left(c_s^2k^2 - \frac{z''}{z}\right)v = 0. \tag{1.79}$$

When we assume the almost de-Sitter universe ($H = const.$) and Bunch-Davies vacuum ($u(\eta, \mathbf{k}) \to e^{-i\mathbf{k}\eta}$ at $\eta \to -\infty$), the solution of v is

$$v = \frac{iaHe^{-ic_sk\eta}}{\sqrt{2c_s^3k^3}}(1 + ic_sk\eta) \simeq \begin{cases} \frac{e^{-ic_sk\eta}}{\sqrt{2c_sk}}, & (c_sk \gg aH), \\ \frac{-iaH}{\sqrt{2k^3}} & (c_sk \ll aH). \end{cases} \tag{1.80}$$

These solutions means the scalar perturbation oscillate at $c_sk \gg aH$ (inside the horizon) and attenuate at $c_sk \ll aH$ (superhorizon). This attenuation is also called classicalization or freeze-out.

Using these results, we can calculate the power spectrum as a stochastic property of the perturbations. The power spectrum at the horizon exit is

$$< \mathcal{R}(\mathbf{k})\mathcal{R}(\mathbf{k}') > \equiv < 0|\mathcal{R}(0, \mathbf{k})\mathcal{R}(0, \mathbf{k}')|0 > = (2\pi)^3\frac{2\pi^2}{k^3}\mathcal{P}_\mathcal{R}(k)\delta^{(3)}(\mathbf{k} + \mathbf{k}'), \tag{1.81}$$

$$\mathcal{P}_\mathcal{R}(k) = \frac{H_k^2}{8\pi^2Q_sc_s^3} = \frac{H_k^2}{8\pi^2M_{\rm Pl}\epsilon c_s}. \tag{1.82}$$

It is useful to evaluate scale dependence of scalar power spectrum by the spectral index,

$$n_s - 1 \equiv \left.\frac{d\ln\mathcal{P}_\mathcal{R}}{d\ln k}\right|_{c_sk=aH} = -6\epsilon + 2\eta. \tag{1.83}$$

Tensor power spectrum

The power spectrum of the tensor perturbation is derived in the similar calculation as the scalar power spectrum. Substituting Eq. (1.71) into Eq. (1.63) and taking second perturbation of h_{ij} leads

$$S = \frac{1}{2}\int d\eta d^3x a^2Q_t\left[\dot{h_ij}^2 - (\partial h_{ij})^2\right], \quad Q_t \equiv \frac{M_{\rm Pl}}{4}. \tag{1.84}$$

We can quantize h_{ij} by

$$h(\eta, \mathbf{x}) = \frac{1}{(2\pi)^3}\int d^3\mathbf{k}\sum_{S=+,\times}\epsilon_{ij}^{(S)}(\mathbf{k})h(\eta, \mathbf{k})^{(S)}e^{i\mathbf{k}\cdot\mathbf{x}}. \tag{1.85}$$

Polarization tensors $\epsilon_{ij}^{(S)}$ work as creation-annihilation operators. Substitution of Eq. (1.85) into Eq. (1.84) gives the wave equation

$$h^{(S)\prime\prime} + 2aHh^{(S)\prime} + k^2h^{(S)} = 0. \tag{1.86}$$

If we define $\phi_\mathbf{k}^{(S)} \equiv zh_\mathbf{k}^{(S)}$ and $z \equiv a\sqrt{2Q_t}$, the above equation is

$$\phi^{(S)\prime\prime} + \left(k^2 - \frac{z''}{z}\right)\phi^{(S)} = 0. \tag{1.87}$$

The solution of this equation is

$$\phi = \frac{iaHe^{-ik\eta}}{\sqrt{2k^3}}(1+ik\eta) \simeq \begin{cases} \frac{e^{-ik\eta}}{\sqrt{2k}}, & (k \ll aH), \\ \frac{-iaH}{\sqrt{2k^3}} & (k \gg aH). \end{cases} \tag{1.88}$$

Also this solution freeze-out at the superhorizon limit as the same as the scalar perturbation.

Including the degree of freedom of polarization, the power spectrum of the tensor perturbation is defined as

$$4 < h_{(S)}(\mathbf{k})h_{(S)}(\mathbf{k}') >= (2\pi)^3 \frac{2\pi^2}{k^3}\mathcal{P}_h(k)\delta^{(3)}(\mathbf{k}-\mathbf{k}'), \tag{1.89}$$

$$\mathcal{P}_h(k) = \frac{H_k^2}{2\pi^2 Q_t} = \frac{2H_k^2}{\pi^2 M_{\rm Pl}}. \tag{1.90}$$

Power spectra Eq. (1.82) and Eq. (1.90) give the tensor-to-scalar ratio,

$$r \equiv \frac{\mathcal{P}_h(k=aH)}{\mathcal{P}_\mathcal{R}(c_s k = aH)} = 16 c_s \epsilon. \tag{1.91}$$

1.3.5 Inflationary potentials

Here we investigate chaotic inflation, the representative inflationary model. For the analysis of inflationary potentials, it is convenient to consider ϕ itself as a time variable. Dividing both sides of Eq. (1.57) by $\dot{\phi}$, we obtain the relationship

$$\dot{\phi} = -2M_{\rm Pl}^2 H'(\phi). \tag{1.92}$$

Using this $H(\phi)$ and Eq. (1.60), e-fold number where pivot scale k_0 exit the horizon at the time of $\phi = \phi_0$ is written as

$$N = \frac{\ln a_{\rm end}}{\ln a_0} = -\frac{1}{2M_{\rm Pl}^2}\int_{\phi_0}^{\phi_{\rm end}} \frac{H}{H'}d\phi = \frac{1}{M_{\rm Pl}^2}\int_{\phi_{\rm end}\frac{H}{H'}}^{\phi_0} \frac{V}{V'}d\phi. \tag{1.93}$$

Since inflationary potential V determines tensor-to-scalar ratio r and spectral index n, we can test the inflation models by measuring these quantities. The potentials which have the form of $V \propto \phi^\alpha (\alpha = 2, 4, \cdots)$ are called chaotic inflation. Here we consider the case of $\alpha = 2$. The flatness conditions are satisfied if $\phi \ll M_{\rm PL}$. Inflation ends up at the time of $\phi \sim M_{\rm PL}$. The field equation Eq. (1.53) is written as

$$\ddot{\phi} + 3H\dot{\phi} + m^2\phi = 0, \tag{1.94}$$

where m is the angular frequency. If we assume $m \gg H$ therefore ignore the dumping term $3H\dot{\phi}$, the solution is $\phi \propto \phi_0 \cos mt$ where ϕ_0 is an initial amplitude. It is convenient for oscillating solution to consider the mean

values in a period. Writing mean value with bar, the energy density and pressure are

$$\bar{\rho} = \overline{\frac{1}{2}\dot{\phi} + V} = \overline{m^2\phi_0^2 \cos^2 mt} = \frac{1}{2}m^2\phi_0^2, \tag{1.95}$$

$$\bar{P} = 0. \tag{1.96}$$

These conditions indicate the matter-like fluid. Since $\bar{\rho}$ is in proportion to a^{-3} for matter, we see that $\phi_0 \propto a^{-3/2}$.

Important inflationary parameters are calculated as

$$\epsilon = \frac{M_{\rm Pl}^2}{2}\left(\frac{V'}{V}\right) = \frac{\alpha^2}{2}\left(\frac{M}{\phi}\right)^2, \quad \eta = M_{\rm Pl}^2\left(\frac{V''}{V}\right) = \alpha(\alpha-1)\frac{M^2}{\phi^2}, \tag{1.97}$$

$$N = \frac{1}{M_{\rm Pl}}\int_{\alpha M}^{\phi_0} \frac{\phi}{\alpha} d\phi = \frac{\phi_0^2}{2\alpha M^2}, \tag{1.98}$$

$$n_s - 1 = -6\epsilon + 2\eta = -\frac{\alpha+2}{2N}, \tag{1.99}$$

$$r = 16 c_s \epsilon = 16\epsilon = \frac{4\alpha}{N}. \tag{1.100}$$

Existing observations has rejected $\alpha = 4$. Substituting $\alpha = 2$ and $N = 50$ gives $n - 1 = -0.04$ and $r = 0.16$.

1.4 Anisotropy of the CMB

1.4.1 Thomson scattering at the last-scattering epoch

The scalar and tensor perturbations, which originate from inflaton and froze out at the horizon exit, make temperature anisotropy in the last-scattering surface.

As we saw in section 1.2.2, the photons start to run freely after the recombination or the last-scattering epoch and reach to us as CMB. Before the last-scattering, the photons are frequently scattered by the electrons. Since the peak wavelength of blackbody radiation at 3000 K ($\sim 1 \times 10^{-6}$ m) is shorter than the Compton wavelength of electron (2.4×10^{-12} m), this scattering is the Thomson scattering. The Thomson scattering makes polarization on the scattered photon. If the temperature around an electron is isotropic, photons with the same intensity come from all directions and the polarization is canceled (Figure 1.2). On the other hand, if there is quadrupole temperature isotropy, the polarization remains and can be observed (Figure 1.3). The polarization lines of the light emissions make a pattern on the celestial sphere. This "field" of the pattern can be separated into the even-parity component which is called the E-mode and the odd-parity component as the B-mode (Figure 1.4).

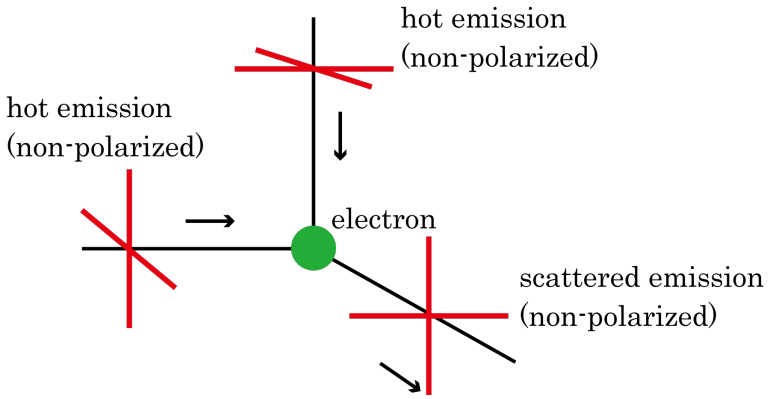

Figure 1.2: Non-polarized light from temperature isotropy.

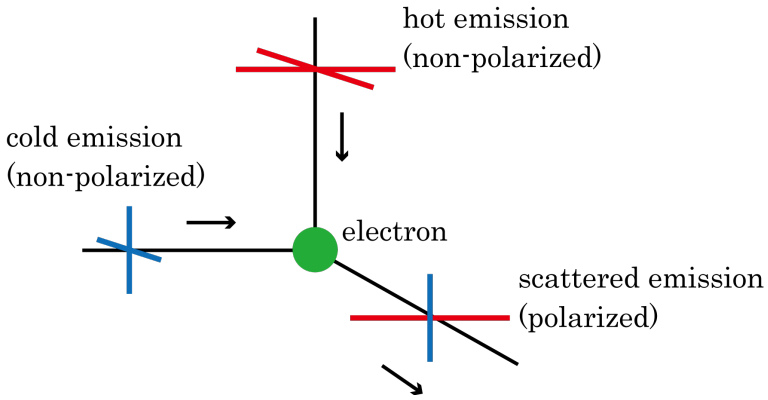

Figure 1.3: Polarized light from quadrupole temperature anisotropy.

At the end of the last-scattering epoch, the CMB have the polarization pattern which is originate to the temperature anisotropy on the last-scattering surface. In addition, on the way to the today's earth its polarization pattern is affected by the gravitational potentials and free electrons generated by reionization.

1.4.2 Stokes parameters and their correlation

The distribution of polarization on the celestial sphere is expressed by the Stokes parameters. In a Cartesian coordinates, the Stokes-Q indicates the polarization along given two axes and the Stokes-U represents the two directions which forms 45° angle to the Stokes-Q axes (Figure 1.5).

Here we describe the electric fields which oscillates in the direction of x-axis and y-axis as E_x and E_y. Similarly we write the ones which oscillates

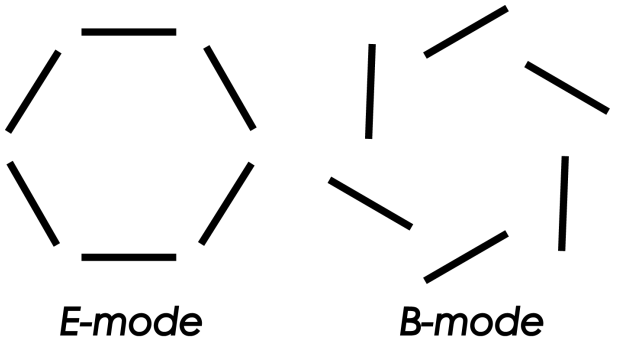

Figure 1.4: The image of the E-mode and B-mode pattern.

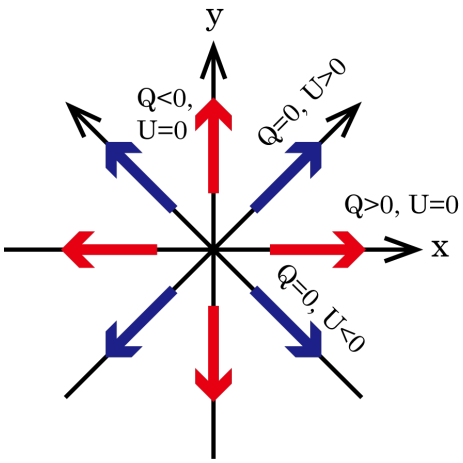

Figure 1.5: The image of the Stokes-Q and U parameters.

in 45° and 135° as E_a and E_b. Then the Stokes-Q and U parameters are defined as $Q \propto E_x^2 - E_y^2$ and $U \propto E_a^2 - E_b^2$. The whole intensity of the light is written as $T \propto E_x^2 + E_y^2 + E_a^2 + E_b^2$. Since the Stokes-Q and U are the same as themselves when they are rotated by 180°, they are 2-spin quantities. Their transforms by rotation angle φ are written in a simple form

$$\tilde{Q} + i\tilde{U} = (Q + iU)\exp(-2i\varphi) \tag{1.101}$$

Next we construct E-mode and B-mode from the Stokes parameters. The Stokes parameters are observable but change their value by the rotation. Since the physical quantities should be coordinate invariant, we need rotation invariant quantities that related to the polarization.

We first adopt the small-angle approximation, that considers a small area that can be regarded as a flat plane on the celestial sphere. We write position

vector from the center of the celestial sphere as $\boldsymbol{\theta} = (x, y) = (\theta\cos\phi, \theta\sin\phi)$. To obtain coordinate invariant quantities, we consider the Fourier transform of Stokes-Q and U,

$$\begin{aligned} Q(\boldsymbol{\theta}) + iU(\boldsymbol{\theta}) &= \int \frac{d^2\ell}{(2\pi)^2} a_\ell \exp(i\boldsymbol{\ell}\cdot\boldsymbol{\theta}), \\ a_{\boldsymbol{\ell}} &= -{}_2a_{\boldsymbol{\ell}} \exp(2i\phi_\ell), \quad \boldsymbol{\ell} \equiv (\ell\cos\phi_\ell, \ell\sin\phi_\ell), \end{aligned} \tag{1.102}$$

where ϕ_ℓ is an azimuth in the Fourier space and $\boldsymbol{\ell}$ means wavelength vectors. When the coordinate system is rotated for angle φ, the azimuth ϕ_ℓ transforms as $\phi_\ell \to \tilde{\phi}_\ell = \phi_\ell - \varphi$ then cancels the transformation of Eq. (1.101). It keeps ${}_2a_{\boldsymbol{\ell}}$ invariant. Therefore Eq. (1.102) can be rewritten as

$$Q(\boldsymbol{\theta}) \pm iU(\boldsymbol{\theta}) = -\int \frac{d^2\ell}{(2\pi)^2} {}_{\pm2}a_\ell \exp(\pm 2i\phi_\ell + i\boldsymbol{\ell}\cdot\boldsymbol{\theta}). \tag{1.103}$$

The functions $\exp(\pm 2i\phi_\ell + i\boldsymbol{\ell}\cdot\boldsymbol{\theta})$ is called 2-spin harmonic functions because they are basis of Fourier expansion of 2-spin quantity.

Here we define E-mode and B-mode as ${}_{\pm2}a_{\boldsymbol{\ell}} \equiv -(E_{\boldsymbol{\ell}} \pm iB_{\boldsymbol{\ell}})$. Then Eq. (1.103) is

$$\begin{aligned} Q(\boldsymbol{\theta}) \pm iU(\boldsymbol{\theta}) &= \int \frac{d^2\ell}{(2\pi)^2} (E_{\boldsymbol{\ell}} \pm B_{\boldsymbol{\ell}}) \exp(\pm 2i\phi_\ell + i\boldsymbol{\ell}\cdot\boldsymbol{\theta}), \\ E_{\boldsymbol{\ell}} \pm B_{\boldsymbol{\ell}} &= \int d^2\theta (Q \pm iU)(\boldsymbol{\theta}) \exp(\mp 2i\phi_\ell - i\boldsymbol{\ell}\cdot\boldsymbol{\theta}). \end{aligned} \tag{1.104}$$

The relationship between each Q, U and E, B is

$$\begin{aligned} E_{\boldsymbol{\ell}} &= \int d^2\theta \left[Q(\boldsymbol{\theta})\cos(2\phi_\ell) + U(\boldsymbol{\theta})\sin(2\phi_\ell)\right] \exp(-i\boldsymbol{\ell}\cdot\boldsymbol{\theta}), \\ B_{\boldsymbol{\ell}} &= \int d^2\theta \left[-Q(\boldsymbol{\theta})\sin(2\phi_\ell) + U(\boldsymbol{\theta})\cos(2\phi_\ell)\right] \exp(-i\boldsymbol{\ell}\cdot\boldsymbol{\theta}). \end{aligned} \tag{1.105}$$

The directions of the E-mode and the B-mode polarization are shown in Figure 1.6. The E-mode polarization is horizontal or vertical to the wavenumber vector. On the other hand, the B-mode tilts 45° against the wavenumber vector.

The two-point correlation functions between E, B and temperature T are the followings;

$$\begin{aligned} &< E_{\boldsymbol{\ell}} E^*_{\boldsymbol{\ell}'} > = (2\pi)^2 \delta_D^{(2)}(\boldsymbol{\ell} - \boldsymbol{\ell}') C_\ell^{EE}, \quad < B_{\boldsymbol{\ell}} B^*_{\boldsymbol{\ell}'} > = (2\pi)^2 \delta_D^{(2)}(\boldsymbol{\ell} - \boldsymbol{\ell}') C_\ell^{BB}, \\ &< T_{\boldsymbol{\ell}} E^*_{\boldsymbol{\ell}'} > = < T^*_{\boldsymbol{\ell}} E_{\boldsymbol{\ell}'} > = (2\pi)^2 \delta_D^{(2)}(\boldsymbol{\ell} - \boldsymbol{\ell}') C_\ell^{TE}. \end{aligned} \tag{1.106}$$

Here $C_\ell^{TE,EE,BB}$ are power spectra. Other two-point correlations, $< E_{\boldsymbol{\ell}} B^*_{\boldsymbol{\ell}'} >$ and $< T_{\boldsymbol{\ell}} B^*_{\boldsymbol{\ell}'} >$ changes their sign by parity transform. Therefore, if the

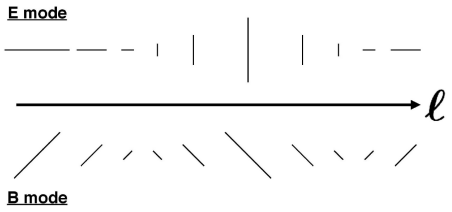

Figure 1.6: The image of the E-mode and B-mode polarization along the given wavenumber vector $\boldsymbol{\ell}$ [2].

probability density function of the primordial perturbation is parity invariant, $< E_\ell B^*_{\ell'} >=< T_\ell B^*_{\ell'} >= 0$. On the contrary, if the primordial physical processes were not parity invariant or photons are affected by parity variant phenomena after the last-scattering epoch, $< E_\ell B^*_{\ell'} >$ and $< T_\ell B^*_{\ell'} >$ have non-zero values. These parity variant phenomena include mis-calibration of polarization angle of the CMB detectors. When the polarization angle changes from α to $\alpha + \Delta\alpha$ in a celestial area, the observed polarization modes and their power spectra are

$$\begin{aligned}
&E_\ell^{\rm obs} \pm iB_\ell^{\rm obs} = (E_\ell \pm iB_\ell)\exp(\pm 2i\Delta\alpha),\\
&C_\ell^{TE,{\rm obs}} = C_\ell^{TE}\cos(2\Delta\alpha), \quad C_\ell^{TB,{\rm obs}} = C_\ell^{TE}\sin(2\Delta\alpha),\\
&C_\ell^{EE,{\rm obs}} = C_\ell^{EE}\cos^2(2\Delta\alpha) + C_\ell^{BB}\sin^2(2\Delta\alpha),\\
&C_\ell^{BB,{\rm obs}} = C_\ell^{EE}\sin^2(2\Delta\alpha) + C_\ell^{BB}\cos^2(2\Delta\alpha),\\
&C_\ell^{EB,{\rm obs}} = \frac{1}{2}\left(C_\ell^{EE} - C_\ell^{BB}\right)\sin(4\Delta\alpha).
\end{aligned} \tag{1.107}$$

To define the E-mode and the B-mode for the whole celestial sphere, we should take a system that locates the observer in the center of the celestial sphere. Taking an unit vector $\mathbf{e}_1$ to the direction of the polar angle and $\mathbf{e}_2$ to the azimuth, the basis $\mathbf{e}_\pm \equiv (\mathbf{e}_1 \pm i\mathbf{e}_2)/\sqrt{2}$ lead the definition for the celestial sphere.

To evaluate the CMB power spectra, scale-invariant spectra as below are traditionally used.

$$\mathcal{C}_\ell \equiv \frac{\ell\,(\ell+1)}{2\pi} C_\ell, \tag{1.108}$$

$$\mathcal{N}_\ell \equiv \frac{\ell\,(\ell+1)}{2\pi} w^{-1} W_\ell^{-1}. \tag{1.109}$$

It is for the reason that the $\mathcal{C}_\ell^{TT}$ generated by gravitational potential on the last-scattering surface is theoretically scale-invariant.

1.4.3 The sources of the E-mode and the B-mode

The quadrupole temperature anisotropy on the last-scattering surface is caused by the anisotropic stress of the photon-baryon fluid. Since the photons are frequently scattered by the electrons, the photons and the electrons moved like mixture fluid. The protons and the helium nuclei were also mixed in this fluid. The primordial scalar and tensor perturbations shake this fluid to make acoustic waves. The acoustic waves make the quadrupole temperature anisotropy and then E-mode polarization. The power spectra of the polarization caused by the acoustic waves are dumped in the small angle scale because the acoustic waves are attenuated by the viscosity of the photon-baryon fluid. This is called Silk dumping. Its effects are seen in the angular scale of $\ell \gtrsim 100$ of the power spectrum.

After the last-scattering epoch, the gravitational potentials of large scale structures causes gravitational lensing effect. This distorts the polarization direction of the CMB and create the E-mode from the B-mode (also the B-mode from E-mode). The lensing polarization is seen in the small angular scale of $\ell \gtrsim 1000$.

In addition, the free electrons generated by reionization scatter the CMB photons to create new polarization patterns. The temperature distribution of CMB have changed from that in last-scattering epoch because of the gravitational potentials. Such energy drift caused by gravitational potentials is called Sachs-Wolfe effect. In this case, the effects from all the gravitational potentials after the last-scattering epoch are integrated so they are called Integrated Sachs-Wolfe effect. The polarization from reionization is seen in the large angular scale, $\ell \lesssim 10$.

The B-mode polarization in the last-scattering epoch is generated by only tensor perturbation, namely, the gravitational waves. Note that the gravitational waves generates both the E-mode and the B-mode. After the last-scattering epoch, the E-mode can change to the B-mode by the gravitational lensing effect (the lensing B-mode). Also the reionization generates the B-mode.

The power spectra of the temperature anisotropy, the E-mode and the B-mode based on today's observations are shown in Figure 1.7. The information of the B-mode from the gravitational waves is necessary to determine the tensor-to-scalar ratio r. On the other hand, the lensing B-mode helps to determine the summation of the mass of the neutrino's three generations because the neutrinos escape from the galaxies to smooth the gravitational potentials.

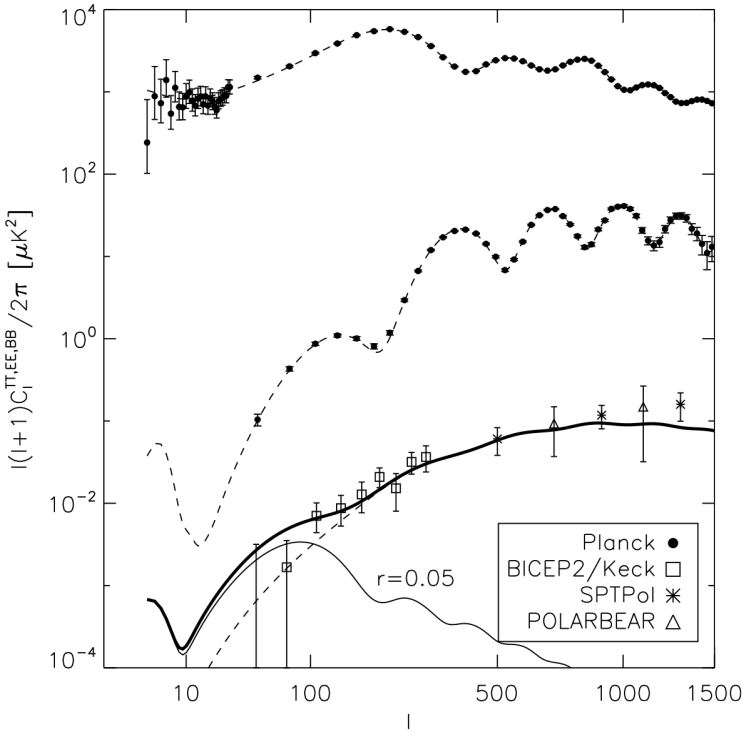

Figure 1.7: The power spectra of the temperature anisotropy, the E-mode and the B-mode of the CMB. The upper dashed line is the temperature anisotropy, the middle dashed line is the E-mode, the bottom dashed line is the lensing B-mode. The regular solid line is the gravitational waves B-mode and the bold solid line is the summation of the lensing and gravitational waves B-mode [2].

2

General methods for CMB observation

2.1 Ground, balloon and satellite-based telescopes

CMB observations have been performed on ground, in the sky with balloons or in space with artificial satellites. Ground-based experiments can deploy large telescopes and long observational time. However, they are disturbed by the atmosphere and cannot observe the whole sky. Balloons are relatively less expensive, and can observe through thin air but the observational duration is short. Satellites are free from the air disturbance and can observe the whole sky, but costs more than ground-based telescopes and has size limitation. Ground-based telescopes are suitable to investigate the small scale structure of the CMB, while satellites can observe the full sky with high sensitivity.

2.2 Target frequency and locations

The observational frequency of the CMB is selected by considering the Planck's law and absorption by water vapor. The CMB is easily absorbed by water vapor in the air. It is because the energy of the millimeter wave with frequency of tens of GHz corresponds to the energy gap of rotational states of an H_2O molecule. The frequencies with weak absorption are called "atmospheric windows" (Figure 2.1). The observations on the ground should choose these windows.

Molecules in the air itself also emit radiation. Since the condition of the air always varies and sometimes makes clouds, it becomes a source of $1/f$ noise in CMB observations. Furthermore, structure of the air makes observations at large angular scales challenging. At a higher elevation angle, a telescope is forced to see the CMB through thicker layers of atmosphere. To eliminate the low frequency noise, some strategies are developed. Polariza-

tion modulation technique using a half wave plate has been introduced for large angular scale observations.

To decrease absorption by water vapor, telescopes of ground-based CMB observations should be located in a dry area. Two main places are the Atacama highland in Chile and the South Pole. The South Pole has drier atmosphere but the Atacama highland provides a broader observable area of the sky due to the earth rotation. POLARBEAR and ACTpol are in Atacama, while BICEP2/Keck Array, SPTpol and several balloon experiments are at the South Pole.

Foreground radiation is another source of external noise. It includes synchrotron radiation and thermal dust emissions, which are two dominant sources of foreground. Synchrotron radiation is emitted from electrons moving in the magnetic field of galaxies and its intensity is proportional to $\nu^{-3} \sim \nu^{-2}$, where ν is the frequency of synchrotron radiation. Thermal dust emissions follow ν^2 and tend to be aligned with the galactic magnetic field so they are polarized. Since their frequency dependences are different from that of CMB (Figure 2.2), multi-frequency observation is useful to distinguish CMB from them. However, observations of CMB polarization are difficult above ~ 250 GHz from anywhere on earth [5], because of high loading from atmosphere and from optical elements, and low ℓ atmospheric noise.

2.3 Optics

Optical system for a CMB telescope is designed to satisfy the purpose of observation. To observe smaller structure of the sky, a telescope with higher resolution is required. A large aperture provides higher resolution but often results in a narrow field of view. It is because light is diffracted on the edge of a lens or an aperture and the field of view of the optical system with sufficient resolution is limited. The optical performance of a CMB telescope is often characterized by a diffraction limited field of view (DLFOV). We use the Strehl ratio, a ratio of the peak intensity from a point source on a given optical system to that of ideal non-aberration system, to define the DLFOV. If the Strehl ratio is larger than 0.8 at the particular point on a focal plane, the system is regarded to be diffraction limited at that point.

Optical systems are classified into refractor-based and reflector-based telescopes. In a refractor-based system, its optical axis is centered and goes straight from the focal plane to the window. BICEP has implemented a refractive-only system, while some other experiments combine reflectors to a refractor-based system to achieve a high throughput (the total amount of light entering to the system) and high resolution [5]. For CMB observations, Gregorian configuration, which has a parabolic primary reflector and an elliptical secondary reflector, is widely adopted.

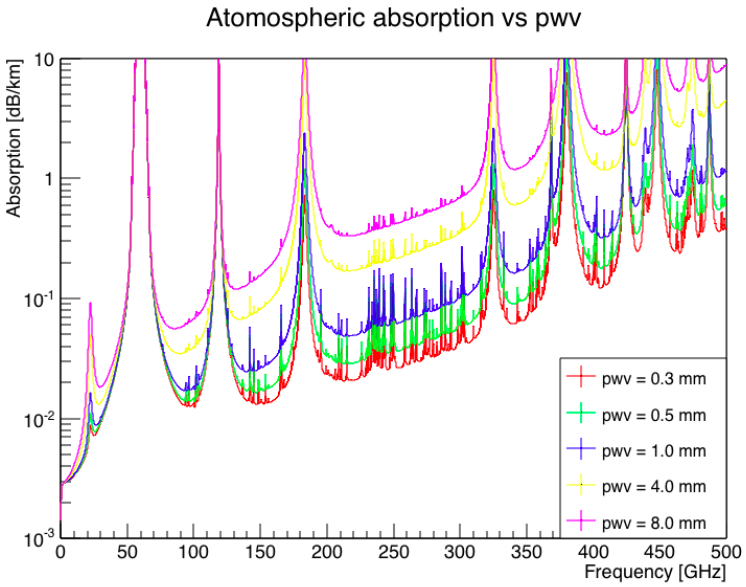

Figure 2.1: Absorption vs frequency by the atmosphere in 5520 m altitude, calculated with AATM model [3]. Precipitable water vapor (pwv) is an index of water vapor in the atmosphere, which means the total amount of water vapor included in the atmosphere per unit area on th ground.

Optical configurations to cancel aberrations optimally are described by Dragone [17][18][19]. EBEX (balloon), WMAP (satellite), and POLARBEAR (Figure 2.3) are based on Gregorian Dragone configuration, which cancels astigmatism aberration [17]. QUIET (ground-based, Atacama) (Figure 2.4) adopted the cross-Dragone configuration [19]. The Gregorian Dragone configuration does not require a large secondary mirror and allow us to implement a baffle to block off the stray light, while the cross-Dragone can achieve a larger field of view.

Purified alumina are widely used as a material of both lenses and filters. A Large refractive index of alumina contributes to compact optical systems. In many cases, inside of the receiver is cooled down to use superconducting detectors and to mitigate emission from receiver itself.

2.4 Detectors

Since intensity of CMB polarization is tiny, we have to observe so many photons that we can statistically determine it. Aligning huge numbers of detectors with high sensitivity is the basic strategy of recent CMB observations. To improve sensitivity of detectors, superconducting materials play

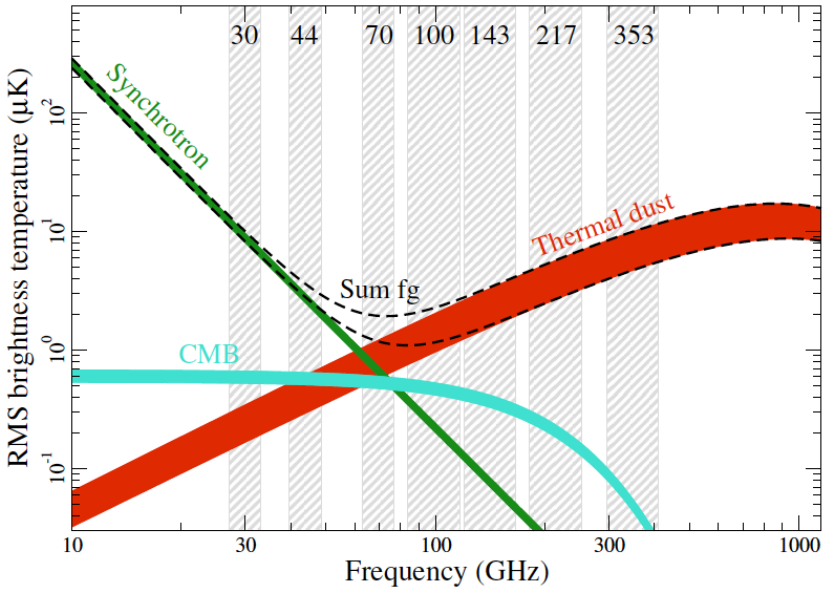

Figure 2.2: Frequencies of polarized emissions from various sources. Each component is smoothed to an angular resolution of $40'$ [4].

an important role.

The transition edge sensor (TES) bolometer is the most popular detector for CMB observation today. The main component of TES bolometer is a superconducting metal piece weakly linked to a thermal bath (Figure 2.5). The thermal bath is cryogenic but a TES is biased by voltage and kept on a transition edge. When a photon enters the TES, its energy turns into lattice vibration and raises the temperature of TES slightly. On the transition edge, resistance of the TES is very sensitive to temperature and (Figure 2.6). Then, increased resistance brings bias power down and the TES goes back to initial operating point on the transition edge. This mechanism is called electro-thermal feedback and realizes short time constant.

In addition to the TES itself, multiplexing readout methods also have been developed. The number of TES bolometers in the current CMB observations tend to reduce statistical uncertainties because the sensitivity of each TES has almost reached the photon noise limit (Figure 2.7). There are many projects for CMB observations that plan to have $\mathcal{O}(1000) \sim \mathcal{O}(10000)$ TESes. Since the size of each TES detector pixel can be as small as a few mm, it is easy to make a detector array. There is a risk of heat transfer, however, through readout lines into the receiver. Some methods have been proposed to readout signals of many TESes with small number of lines. Time-division multiplexing (TDM) makes slight delay between signals from

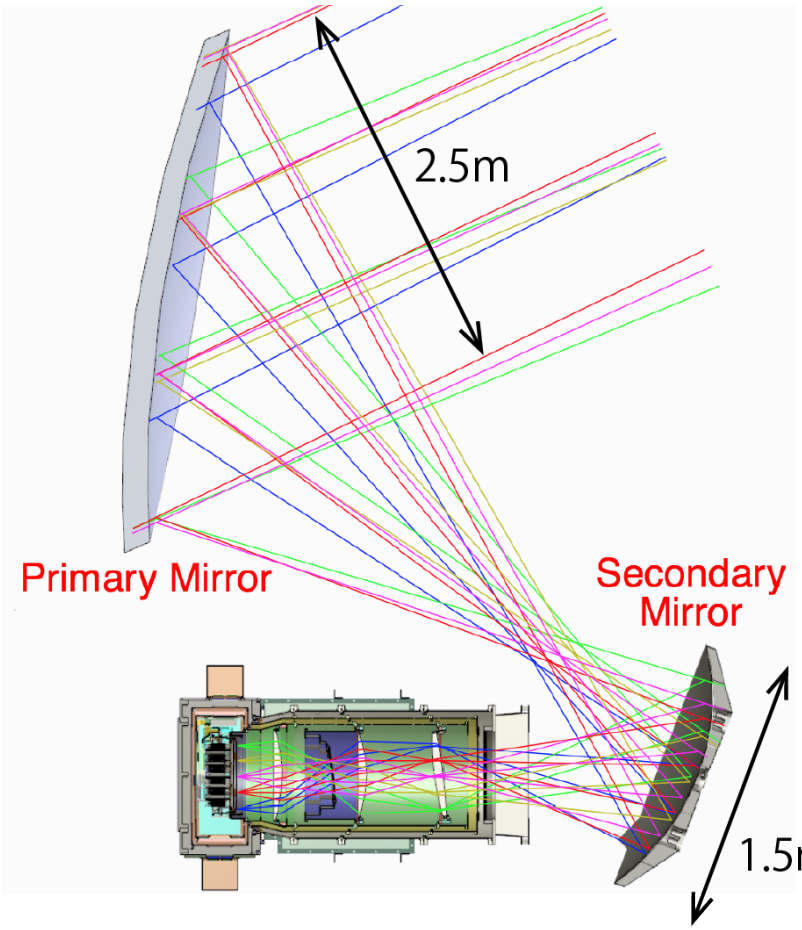

Figure 2.3: Optical design of telescope and receiver of POLARBEAR-2.

TESes [22]. The main disadvantage of TDM is that noise increases in proportion to a square root of the number of multiplexed TESes. Code-division multiplexing (CDM) is another method that modulates signals by orthogonal functions by a code, typically the Walsh code [23]. Frequency-division multiplexing (FDM), or frequency-domain multiplexing, modulates signals by different frequencies. CDM and FDM has no noise increase with the number of multiplexed TESes. Details of FDM readout system used in POLARBEAR-2 are described in Section 3.3.3.

For observations in low frequencies ($\lesssim$ 100 GHz), a high electron mobility transistor (HEMT) is often used as a detector. A HEMT consists of lamination layers of doped and undoped semiconductors. Undoped layers behave as conductive bands for electrons. It does not discard information of phase, so it can be used for interferometers.

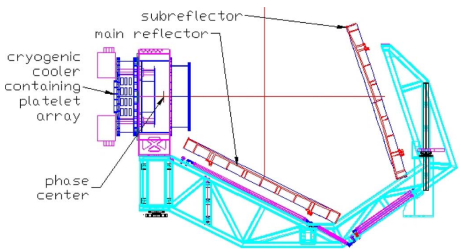

[1] Optical design of QUIET telescope [20].

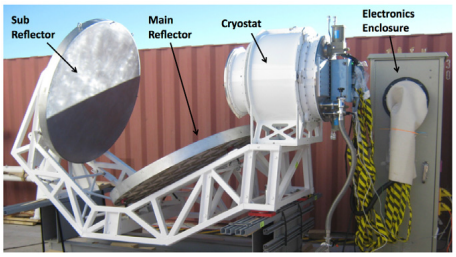

[2] Picture of QUIET telescope [21].

Figure 2.4: Optical design and photo image of QUIET telescope.

Interferometers have several advantages for CMB observation. It can easily adjust angular resolution by changing baseline. Moreover, it can filter out atmospheric fluctuations because it takes correlations of detected signals with each other. One of the disadvantage of interferometer is a high cost. QUBIC is a planned interferometric CMB experiment.

From the viewpoint of multiplexing, microwave kinetic inductance detectors (MKIDs) are expected to be introduced for next generation CMB experiments. The MKID has an antenna, a superconducting resonator and a feedline (Figure 2.8). When photons enter the antenna, Cooper pairs in the resonator are broken. Then, the inductance of the resonator increases and the resonance amplitude and phase change. Since the resonance frequency can be adjusted with the length of resonator, the MKID is suitable to frequency-domain multiplexing. It allow us to readout $\mathcal{O}(1000)$ detectors by a single feedline. Although MKID has not been used for CMB observation yet, there are a few projects that are in preparation and plan to observe CMB B-mode using MKIDs, including the GroundBIRD experiment.

2.5 Uncertainty of power spectra and tensor-to-scalar ratio

The statistical uncertainty of CMB power spectra is caused by various noise of detector array and uncertainty of beam shape. Noise on the detector array and amount of observation sample determine map depth, denoted by w, as

$$w_T = \frac{1}{\mathrm{NET}^2} \frac{t_{\mathrm{obs}}}{4\pi f_{\mathrm{sky}}}, \tag{2.1}$$

where the subscript T indicates temperature. NET is a noise-equivalent temperature of array, f_{sky} is a fraction of sky coverage and t_{obs} is an observation time. A map depth for polarization is calculated by NEPol, theoretically

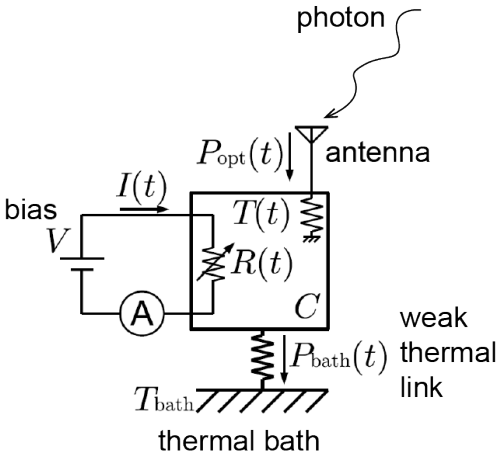

Figure 2.5: Simplified picture of TES circuit.

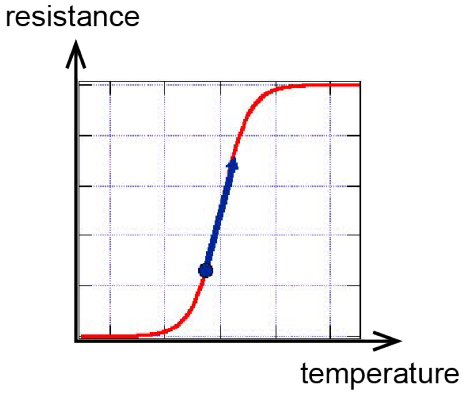

Figure 2.6: Principle of TES. Incoming photons generate phonon in the superconducting film and raise the temperature slightly. A small change of temperature is translated to a large change of resistance.

$\sqrt{2}$ times as NET, instead of NET. On the other hand, when we assume that the beam of detector has Gaussian shape, it determines the window function W_ℓ as

$$W_\ell = \exp\left[-\ell\left(\ell+1\right)\frac{\theta^2_{\rm FWHM}}{8\log 2}\right], \tag{2.2}$$

where $\theta_{\rm FWHM}$ is a FWHM of beam of each detector. The total noise is often expressed as $N_\ell \equiv w^{-1}W_\ell^{-1}$.

Using these parameters, the statistical uncertainty of C_ℓs are estimated by the Knox formula [24][25][26],

$$\Delta C_\ell^{TT} = \sqrt{\frac{2}{\left(2\ell+1\right)f_{\rm sky}}}\left[C_\ell^{TT} + w_T^{-1}W_\ell^{-1}\right], \tag{2.3}$$

$$\Delta C_\ell^{EE} = \sqrt{\frac{2}{\left(2\ell+1\right)f_{\rm sky}}}\left[C_\ell^{EE} + w_P^{-1}W_\ell^{-1}\right], \tag{2.4}$$

$$\Delta C_\ell^{BB} = \sqrt{\frac{2}{\left(2\ell+1\right)f_{\rm sky}}}\left[C_\ell^{BB} + w_P^{-1}W_\ell^{-1}\right], \tag{2.5}$$

$$\Delta C_\ell^{TE} = \sqrt{\frac{2}{\left(2\ell+1\right)f_{\rm sky}}}\left[\left(C_\ell^{TE}\right)^2 + \left(C_\ell^{TT} + w_T^{-1}W_\ell^{-1}\right)\left(C_\ell^{EE} + w_P^{-1}W_\ell^{-1}\right)\right]^{\frac{1}{2}}, \tag{2.6}$$

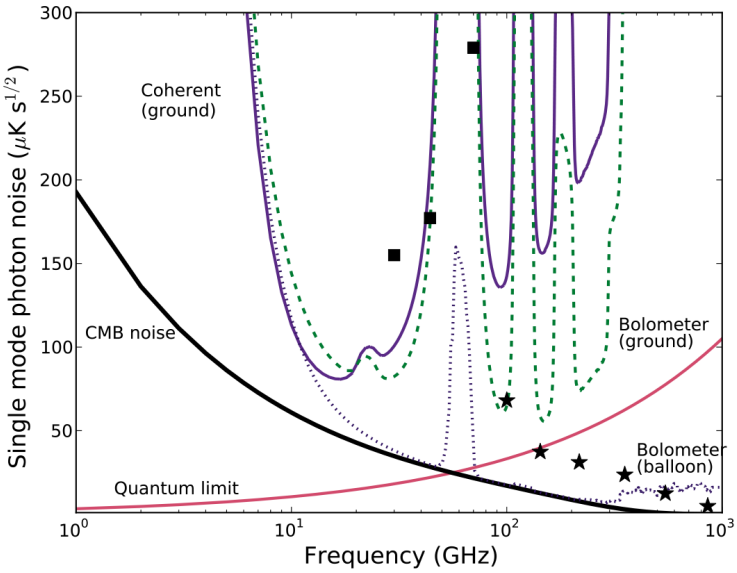

Figure 2.7: Single mode photon noise of CMB observations [5]. Squares and stars are reported noise intensities of Planck. Square is coherent receiver noise and star is bolometer noise.

$$\Delta C_\ell^{EB} = \sqrt{\frac{2}{(2\ell+1)\, f_{\rm sky}}} \left[\left(C_\ell^{EB} \right)^2 + \left(C_\ell^{EE} + w_P^{-1} W_\ell^{-1} \right) \left(C_\ell^{BB} + w_P^{-1} W_\ell^{-1} \right) \right]^{\frac{1}{2}}. \tag{2.7}$$

Although the cosmological parameters including r are derived by likelihood analysis of CMB power spectra, the statistical uncertainty of these parameters can be analytically estimated by Fisher matrix $\mathbf{F}$ [27]. The element of $\mathbf{F}$ is

$$F_{ij} \equiv \sum_{\ell=\ell_{\rm min}}^{\ell_{\rm max}} \frac{2\ell+1}{2} f_{\rm sky} {\rm tr} \left(\boldsymbol{C}_\ell{}^{-1} \frac{\partial \boldsymbol{C}_\ell}{\partial p_i} \boldsymbol{C}_\ell{}^{-1} \frac{\partial \boldsymbol{C}_\ell}{\partial p_j} \right), \tag{2.8}$$

with different cosmological parameters θ_i, θ_j, and covariance matrix

$$\boldsymbol{C}_\ell \equiv \begin{pmatrix} \bar{C}_\ell^{TT} + N_\ell^{TT} & \bar{C}_\ell^{TE} & 0 & C_\ell^{Td} \\ \bar{C}_\ell^{TE} & \bar{C}_\ell^{EE} + N_\ell^{EE} & 0 & C_\ell^{Ed} \\ 0 & 0 & \bar{C}_\ell^{BB} + N_\ell^{BB} & 0 \\ C_\ell^{Td} & C_\ell^{Ed} & 0 & C_\ell^{dd} + N_\ell^{dd} \end{pmatrix} \tag{2.9}$$

where the index d (deflection) indicates the gravitational lenging component and $\bar{C}_\ell$s are spectra after removing it. Statistical uncertainty of a cosmological parameter is derived just as

$$\sigma\left(p_i\right) = \sqrt{|\boldsymbol{F}^{-1}|_{ii}}. \tag{2.10}$$

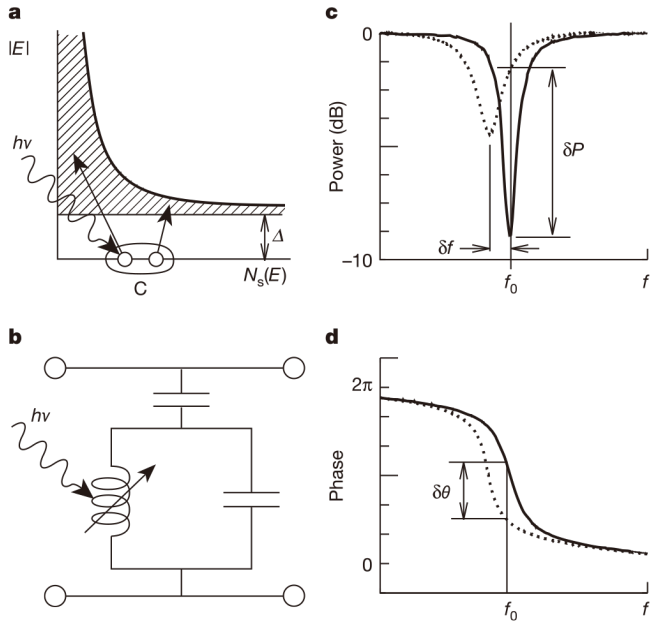

Figure 2.8: Principles of MKID. (a) Photons with energy higher than a band gap Δ can break Cooper pairs and excite quasiparticles. (b) Simplified picture of MKID circuit. Excitation of quasiparticles changes the inductance. (c) Change of signal amplitude. (d) Change of signal phase [6].

We describe tensor-to-scalar ratio r as an example of cosmological parameter. When only B-mode is used for deriving r, and other parameters are fixed, the uncertainty of r is [25]

$$\begin{aligned}\sigma(r) &= \left[\sum_\ell \left(\frac{\partial \bar{C}_\ell^{BB}}{\partial r}\right)^2 \frac{1}{\left(\Delta \bar{C}_\ell^{BB}\right)^2}\right]^{-\frac{1}{2}} \\ &= \left[\sum_\ell \left(\bar{C}_\ell^{BB}(r=1)\right)^2 \frac{(2\ell+1) f_{\rm sky}}{2} \frac{1}{\left(\bar{C}_\ell^{BB} + w_P^{-1} W_\ell^{-1}\right)^2}\right].\end{aligned} \tag{2.11}$$

In the transformation from the first line to the second, we used the relation that C_ℓ^{BB} originated to the primordial gravitational waves is in proportion to r. In an estimation based on a fiducial value $r = 0$, this formula is

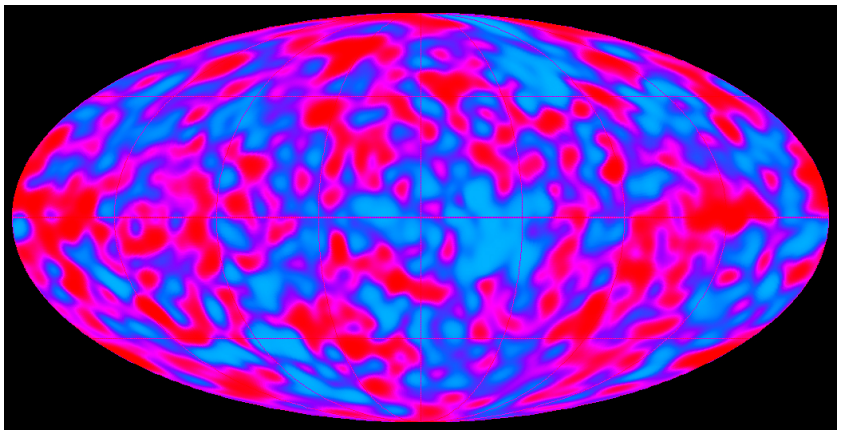

Figure 2.9: The full sky map of CMB anisotropy measured by COBE. Galactic radiation and dipole component are subtracted.

simplified to

$$\sigma\left(r=0\right)=\left[\sum_{\ell}\frac{\left(2\ell+1\right)f_{\mathrm{sky}}}{2}\left(\frac{\bar{C}_{\ell}^{BB}\left(r=1\right)}{w_{P}^{-1}W_{\ell}^{-1}}\right)^{2}\right]^{-\frac{1}{2}}. \tag{2.12}$$

2.6 Current status of B-mode observation

The first CMB detection was done by Penzias and Wilson in 1964 [28]. They unexpectedly detected the CMB by an ground-based antenna. Temperature anisotropies of CMB were discovered by the COBE satellite [29]. Figure 2.9 shows the full sky map of CMB anisotropies. Since then many experimental projects have measured CMB and updated cosmological parameters.

Balloon experiments were also in the mainstream of CMB observation. The MAXIMA experiment in Northern America and the BOOMERANG experiment around the South Pole investigated details of temperature anisotropies, especially the first peak at $\ell \sim 200$. Also ground-based interferometers, such as CAT and Cosmic Background Imager, contributed to measure small structures of CMB temperature anisotropies. The full sky map of CMB anisotropy has been updated by WMAP (Figure 2.10) and Planck (Figure 2.11).

DASI was an interferometer that first discovered the polarization of CMB [30]. After the discovery, development of detector technologies was rapid and precise measurement of CMB polarization on ground is possible today.

The frontier of CMB observation today is at the B-mode polarization and the main interest is testing the inflation hypothesis. The tensor-to-

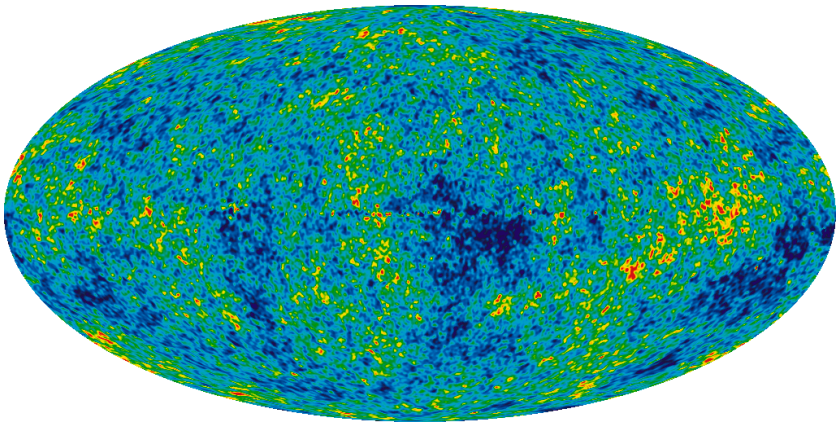

Figure 2.10: The full sky map of CMB anisotropy measured by WMAP.

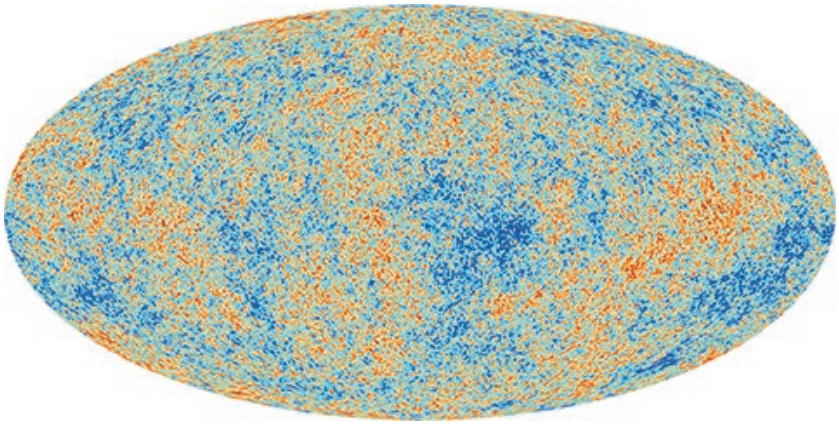

Figure 2.11: The full sky map of CMB anisotropy measured by Planck.

scalar ratio r has not been determined yet, but only an upper limit has been obtained. The most recent constraint is $r < 0.06$ (95% C.L.), yielded by combination of the BICEP2/Keck Array observation plus Planck's low-ℓ and other data [7]. Figure 2.12 shows the constraint on r and spectral index n_s. The constraint $r < 0.06$ already rejects most of chaotic inflation models.

The sum of neutrino masses, $\sum_\nu m_\nu$, is another motivation of CMB B-mode observations. Ground-based telescopes are trying to reconstruct gravitational lensing potential by observing small angular scales. The sum of the neutrino masses of three generations is constrained to $\sum_\nu m_\nu < 0.16$ eV from CMB and external data at present [31].

The current status of CMB B-mode observation and predicted power spectrum are shown in Figure 2.13. High ℓ regions have been searched by many projects. POLARBEAR-1 has reported the first direct evidence for

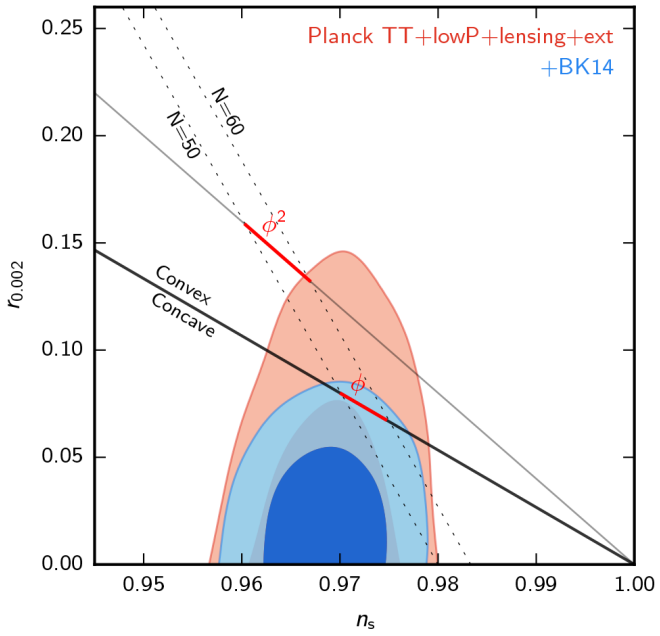

Figure 2.12: Constraints in the r vs n_s plane yielded by the BICEP2/Keck Array plus Planck and other data [7].Chaotic inflation models are constrained from the constraints on r, n_s and N.

gravitational lensing B-mode signal in 2014, based on only CMB data. The B-mode polarization originating from primordial gravitational waves has not been detected yet.

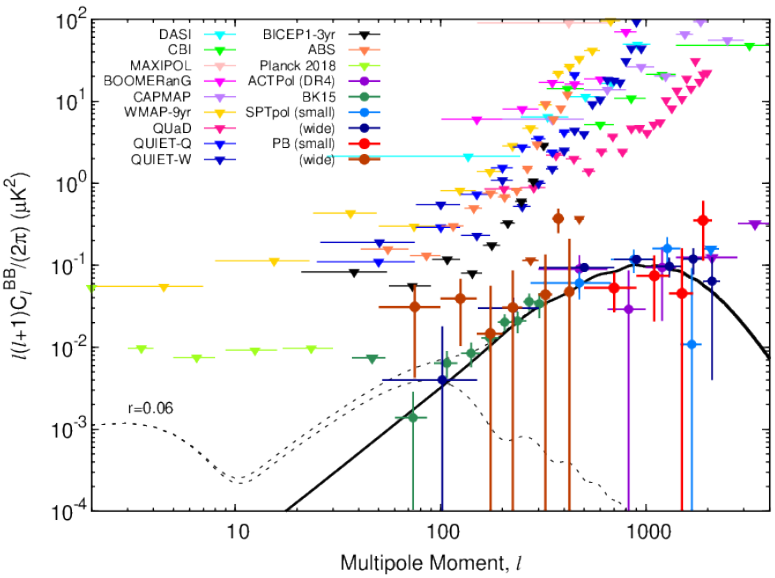

Figure 2.13: Current status of CMB B-mode research (on courtesy of Dr. Yuji Chinone).

3

POLARBEAR-2 experiment

POLARBEAR-2 (or PB2) is a ground-based CMB observational experiment. It is an upgrade of POLARBEAR (or PB or PB1), which has been observing the CMB B-mode since 2012 in the Atacama highland, Chile. POLARBEAR uses an off-axis telescope with Gregorian configuration, named Huan Tran Telescope after the project manager (Figure 3.1).

3.1 Science goals of POLARBEAR-2

POLARBEAR-2 has two major science goals. One is to constrain the tensor-to-scalar ratio r. From the large angular scale observations, POLARBEAR-2 expects to search or constrain r down to 0.01 (95% C.L.). The other is to constrain the sum of neutrino masses $\sum_\nu m_\nu$. Small angular scale observations are expected to enable POLARBEAR-2 to search for or constrain $\sum_\nu m_\nu$ down to 90 meV (68% C.L.) [13]. Sensitivity of POLARBEAR-2 on r is shown in Figure 3.2.

3.2 Observational tactics

3.2.1 Reflective telescope

POLARBEAR-2 uses an off-axis reflective telescope, which has the same design as one used for POLARBEAR. It is located at James Ax Observatory on Mt. Cerro Toco in the Atacama highland, northern Chile, and its altitude is 5,200 m (Figure 3.3).

Telescope of POLARBEAR-2 has a $\sim$4 meters diameter primary mirror and a 1.5 meter diameter secondary mirror. The diameter of the beam projected to the primary mirror is 2.5 m. It also has baffles around the primary mirror and between primary and secondary mirror, in order to mitigate sidelobes and stray light. A large primary mirror provides high resolution required for observing small angular scales. Rays are focused at

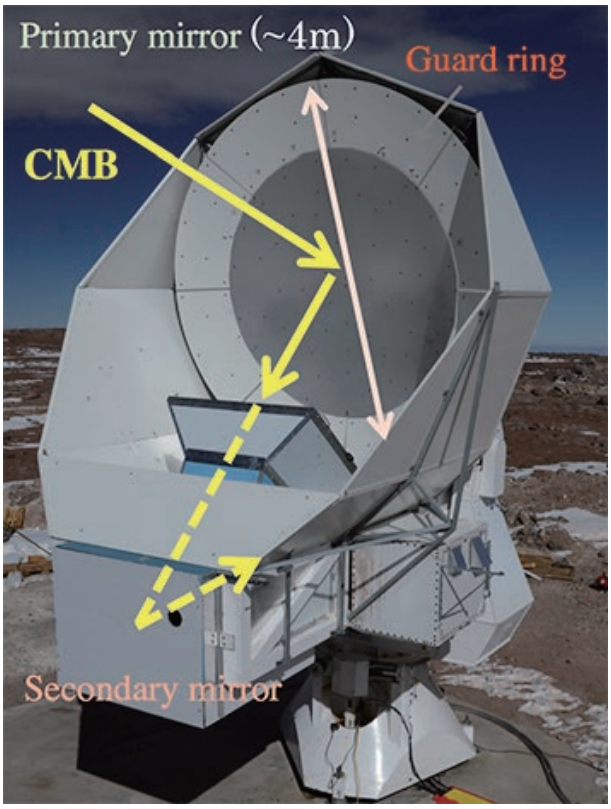

Figure 3.1: Huan Tran Telescope used in POLARBEAR. POLARBEAR-2 uses the same design and location of two mirrors.

the primary focus between the primary and secondary mirror, then reflected by the secondary mirror and enter into the receiver. The telescope has a 4.8° field of view as a whole [14].

Our telescope can observe large areas of the sky by controlling its boresight direction both in elevation and azimuth axes. Its observational method is called the constant elevation scan (CES) strategy, which keeps the same elevation and repeats a horizontal swing. Since the atmospheric condition is always changing, radiation from the air generates $1/f$ noise. With the CES strategy, we modulate signals by its swings and then mitigate the $1/f$ noise caused by the atmospheric fluctuation.

A large primary mirror and CESes enable POLARBEAR-2 to study both large and small angular scales, which is necessary to detect primordial gravitational waves and gravitational lensing. POLARBEAR-2 is expected to be sensitive to the angular scale of $25 \leq \ell \leq 2500$. Effective separation of the lensing B-mode from the large angular scale B-mode, called delensing, will further improve sensitivity to the inflationary B-mode.

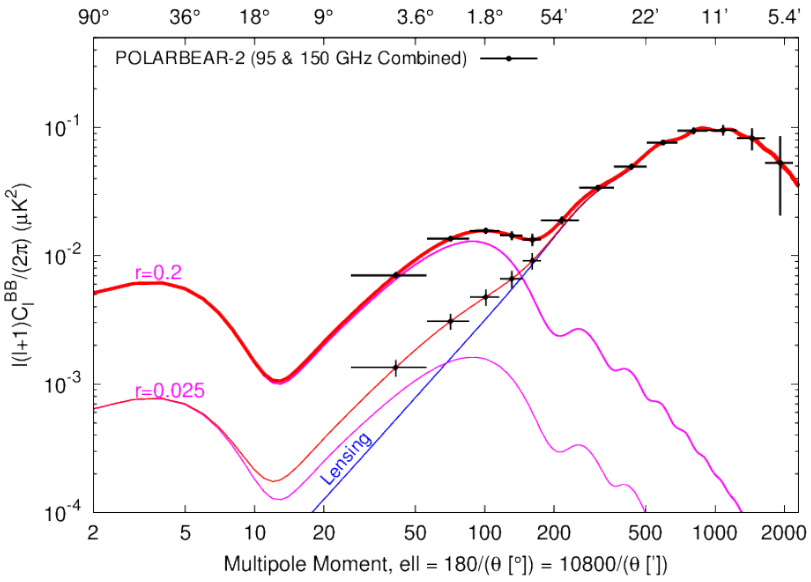

Figure 3.2: Simulated power spectra and expected sensitivities of POLARBEAR-2.

Main specifications of the telescope are summarized in Table 3.1.

3.2.2 Analysis pipeline

Acquired observation data are analyzed in a procedure shown in Figure 3.4. First the raw time-ordered data, which is modulated by a polarization modulator called half-wave plate (HWP), is demodulated. Then various calibrations are performed to the demoulated TODs. It includes calibrations of gain, offset, polarization angle and pointing. Based on calibrated time-ordered data, then sky maps of temperature and polarization are drawn. The data are validated through the null tests. In the null tests, we check internal consistency by splitting the data by various conditions, such as good and bad weather, and compare the spectra computed from them. Finally cross correlation of the maps are calculated to derive power spectra of CMB.

3.3 POLARBEAR-2 receiver

The POLARBEAR-2 receiver has the following features:

- 7,588 TES bolometers. (6 times of POLARBEAR.)
- Large cryogenic optical system. (Twice larger in diameter than POLARBEAR.)

Description	Specification	Achieved performance
Maximum Az/El velocity	4°/s	4°/s
Maximum Az/El acceleration	2°/s^2	2°/s^2
Azimuth travel	±200°	±200°
Elevation travel	+40° to +90°	+40° to +90°
Pointing reconstruction error	10 arcsec	12 arcsec

Table 3.1: Performance of POLARBEAR-2 telescope: specifications and achieved performance [12]. POLARBEAR has been actually using elevation travel above +30°.

Figure 3.3: Overview of the observational site of POLARBEAR-2 in Chile. The receiver of POLARBEAR is upgraded to those of POLARBEAR-2 and two more telescopes are built.

- Two-frequency-band (dichroic) detector array for 95 GHz and 150 GHz. (Only 150 GHz at POLARBEAR.)

A large number of detectors reduce statistical uncertainty but require a large focal plane to mount detectors. Large optical elements are also needed. POLARBEAR-2 has a 365 mm diameter focal plane that is connected to a cold head of cryogenic system at 270 mK.

Inside of this receiver it keeps vacuum and is cooled stepwisely. There are 300 K, 50 K, 4K shells and 2 K, 350 mK, 250 mK stages. The focal plane and detector array are put on the 250 mK stage. The 4 K shell is cooled by a pulse tube cooler (PTC), using superfluid ^{4}He. The 250 mK stage is cooled by a sorption cooler, using ^{4}He and ^{3}He.

We employ dichroic detectors array to mitigate contamination from galac-

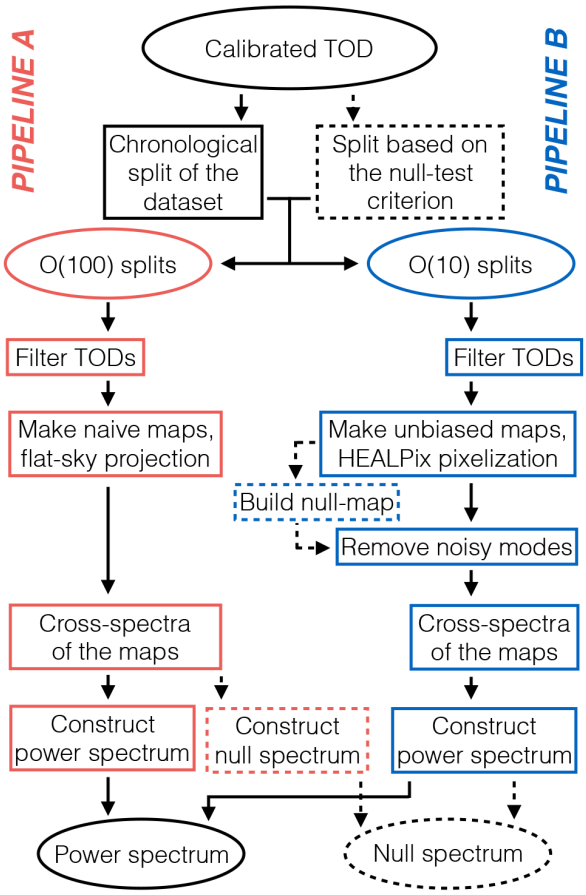

Figure 3.4: Analysis pipeline of POLARBEAR-2 data [8].

tic dust emission [32]. Since intensity of polarized synchrotron radiation from galactic dust depends on frequency, multiband observation is useful to separate it from CMB.

Specifications of POLARBEAR-2 receiver are summarized in Table 3.2. Angular resolutions are 5.2 and 3.5 arcmin FWHM for 95 GHz and 150 GHz, respectively [14]. Noise equivalent temperature (NET) of each TES bolometer is expected to be 360 $\mu\mathrm{K}\sqrt{\mathrm{s}}$. NET of the total array is 5.8 $\mu\mathrm{K}\sqrt{\mathrm{s}}$ in each frequency and 4.1 $\mu K\sqrt{s}$ in combination of them [13].

3.3.1 Optical elements

The POLARBEAR-2 receiver (Figure 3.5) can be divided into two parts. A tube-shaped front part is called “optics tube” and a box part including focal plane is called “backend”. Here we describe optical elements in the optics tube from its sky-side to ground-side.

Description	POLARBEAR-2	POLARBEAR-1
Frequency	90 GHz & 150 GHz	150 GHz
Number of TES	7588	1274
Diameter of Focal Plane	365 mm	190 mm
NET (TES)	360/360 $\mu K\sqrt{\text{s}}$ (90/150 GHz)	480 $\mu K\sqrt{\text{s}}$
NET (array)	4.1 $\mu K\sqrt{\text{s}}$	23 $\mu K\sqrt{\text{s}}$
FDM Multiplexing number	40	8
Field of view	4.8°	2.3°
Angular resolution	5.2/3.5 arcmin. (90/150 GHz)	3.5 arcmin.
Sky coverage	1.6%	65%
Observing time	3 years	2 years
Observation efficiency	18%	18%

Table 3.2: Specifications of POLARBEAR and POLARBEAR-2 [12][13][14].

Warm half-wave plate

A warm half-wave plate (WHWP) is a continuously rotating sapphire plate for modulating polarization angle of entering light. It is set in front of the window of the receiver and rotating at 2 Hz. Since sapphire is made of birefringent material, it shifts the phase of light dependently on its polarization state. It results in a change of the polarization angle of the outgoing light. By rotating the WHWP with a frequency higher than $1/f$ knee, the frequency where the $1/f$ noise becomes equal to white noise, the WHWP reduces $1/f$ noise originated by fluctuation of the atmosphere and enables each bolometer to measure polarization without pair-difference analysis [33]. Since the rotation frequency of polarization is four times as fast as the WHWP rotation, a rotation at 2 Hz results in the polarization modulation at 8 Hz.

Zotefoam window

POLARBEAR-2 receiver's window that faces to the sky is covered with high-density polyethylene foam manufactured by ZOTEFOAMS. It keeps the vacuum inside the receiver and is transparent to millimeter waves, while it absorbs infrared light.

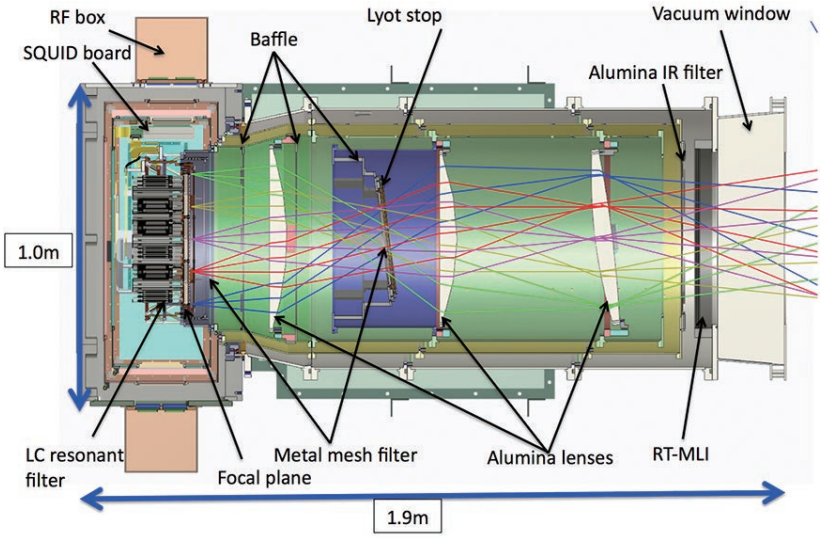

Figure 3.5: A cross section of the POLARBEAR-2 rceiver. Simulated light rays are also shown.

RT-MLI

Thermal radiation at 300 K from the zotefoam window enters RT-MLI. RT-MLI consists of 10 layers of 3 mm thick styrofoams. Styrofoams are polystyrene foams manufactured by The Dow Chemical Company. They let millimeter waves pass but absorb infrared light. RT-MLI works as an thermal insulator and mitigates the thermal load that enters to the alumina filter [9]. Between the 300 K window and the 50 K alumina filter, thermal radiation cooled to 180 K through RT-MLI. The results of temperature simulation and measurement are shown in (Figure 3.6).

Alumina filter

There is a 430 mm diameter filter made with alumina cooled to 50 K. Infrared light is reduced through this filter but millimeter wave passes.

A pulse tube cooler (PTC) is connected here.

Field lens

The optics tube has three alumina lenses cooled to 4 K. Their surfaces are coated with anti-reflection (AR) coating. Since alumina has a high refractive index and birefringence, even millimeter wave is partly reflected. Two layers of AR coating are applied and they correspond to two observed frequencies of CMB (Figure 3.7). The field lens is 440 mm in diameter.

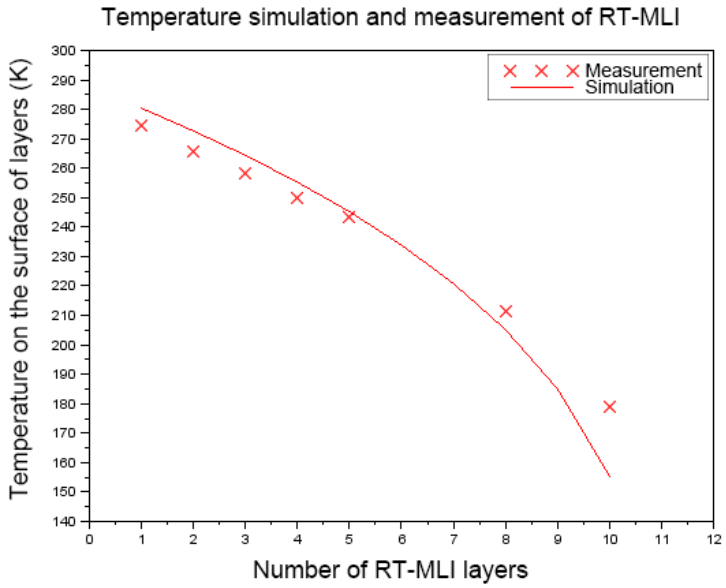

Figure 3.6: Temperature simulation and measurement against the number of RT-MLI layers. Temperatures of the most inner layer are shown. It is based on the model equation suggested in [9].

Aperture lens

The aperture lens is 400 mm in diameter. It adjusts the amount of light.

Collimator lens

The collimator lens is 500 mm in diameter and corrects the aberration to make parallel rays.

Lyot stop

Lyot stop is an aperture which is fringed with blackbody absorbers (Figure 3.8). It is placed between the aperture lens and the collimator lens. The absorbers define the beam edge to control sidelobes. They are made of KEK black, the material of black body developed at KEK [34].

Metal mesh filter

Metal mesh filters (MMFs) are infrared filters [35]. They are mesh layers of polypropylene coated by copper. Large MMFs with a cut-off frequency of 261 and 360 GHz are placed in the 4 K shell. Also MMFs with a cut-off

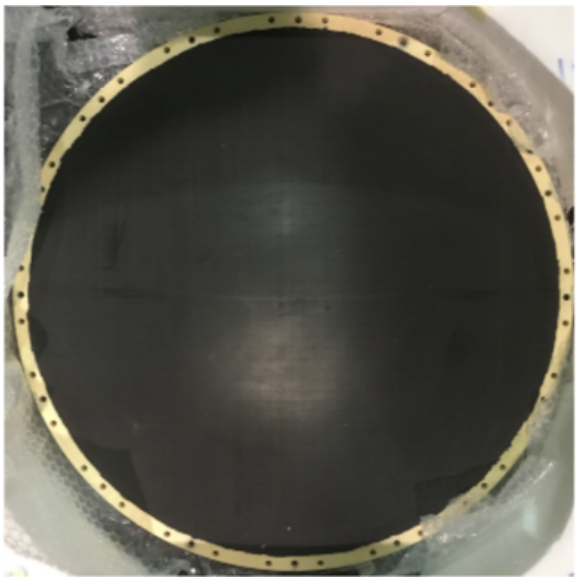

Figure 3.7: An alumina lens with AR coating.

frequency of 171 GHz are placed at the 350 mK stage just in front of the focal plane.

3.3.2 Detectors array

7,588 TES bolometers of POLARBEAR-2 are placed on a 365 mm diameter focal plane cooled to 0.3 K (Figure 3.9). The focal plane is a copper structure supported by the 250 mK stage surrounded by the ring-shaped 350 mK stage, 2 K stage and 4 K stage. Each stage is supported by Vespel resin insulators. A sorption cooler cools these cryogenic parts.

The TES bolometers are distributed into 7 wafers (Figure 3.10). Each wafer has 271 pixels and each pixel has 4 bolometers, corresponding to two polarization angles and two observed frequencies (Figure 3.11).

A hemisphere-shaped, AR-coated lens covers each pixel. It is called lenslet and collects light to an antenna on the pixel. POLARBEAR-2 adopts the sinuous antenna desgin, which is sensitive to a broad frequency range, instead of a slot antenna of POLARBEAR. Incident photons are captured by the sinuous antenna and go through 95 and 150 GHz bandpass filters. Then photons are thermalized in lead lines made of superconducting Nb and resistive Ti. Finally TES bolometers absorb the heat. Polarization is detected as the difference between signals from orthogonal bolometers in the same pixel.

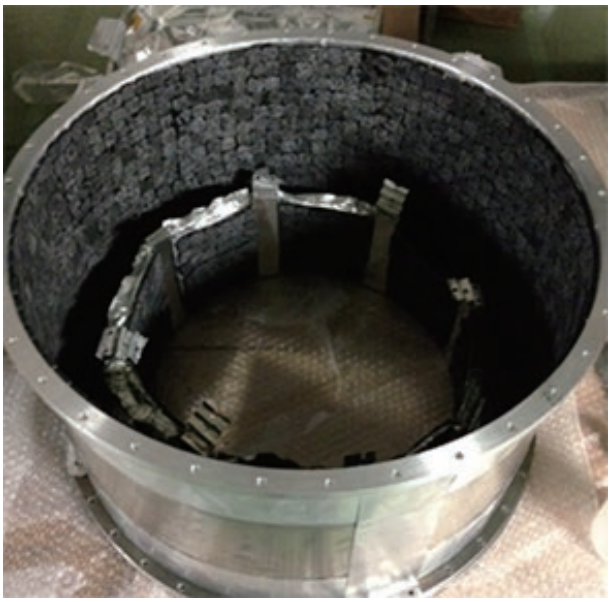

Figure 3.8: Lyot stop.

3.3.3 Readout system

Behind the wafers, cases of circuit boards called focal plane towers are connected. From here the readout chain starts. The readout chain of POLARBEAR-2 consists of the elements as follows:
TES bolometers → LC filters → SQUIDs → SQUID controllers → Ice-Boards.

NbTi stripline

TES bolometers and the 4 K shell are connected by NbTi alloy striplines. These striplines are 10 μm thin and superconducting at 4 K.

LC filter

Different resonant frequencies are assigned to TES bolometers by LC filters and signals are merged into a small number of lines. This method is called frequency domain multiplexing (FDM). LC filters consists of inductors and capacitors. The resonant frequency is determined by variation of capacitance, while inductors have all the same inductance. The signals can be distinguished by demodulation later. While POLARBEAR has read out 8 bolometers by a line, POLARBEAR-2 reads out 40 bolometers. POLARBEAR-2 owes this improvement partly to the new LC filters.

Figure 3.9: Focal plane of POLARBEAR-2.

SQUID

Signals from TES bolometers are amplified by superconducting quantum interference devices (SQUIDs). SQUIDs are low-noise amplifiers with low impedance that matches TES bolometers ($\sim 1\Omega$). They are cooled to 4 K.

POLARBEAR-2 uses DC-SQUIDs that have two superconductor half-loops connected by Josephson junctions (Figure 3.12). When a coil is placed near a SQUID, magnetic flux passing through the loop are quantized. Then, the wave functions of electrons in the loop generate phase shifts across the Josephson junctions. The Josephson effect tells that currents flow over Josephson junctions. The phase shifts depend on the quantized magnetic flux. The SQUID can convert magnetic flux to current.

For impedance matching to back-end readout circuits, 100 SQUIDs are accumulated into an array and implemented on a chip. One chip can read out 40 TES bolometers. 8 chips are loaded on a SQUID card. SQUID cards inside the cryostat are connected to SQUID controller boards located outside the cryostat.

SQUID controller board

SQUID controller boards control currents for biasing SQUIDs. They are in a metal box attached outside the receiver and shielded from radio-frequency (RF) waves. Between SQUID controller boards and back-end readout cables, we place filters called Pi filters. TES wafers and SQUIDs are fabricated at University of California, Berkeley [36].

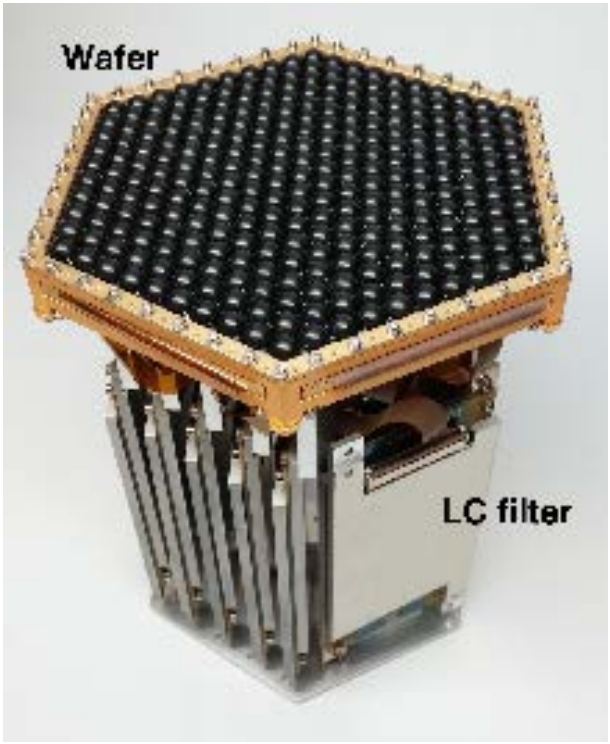

Figure 3.10: A detector wafer and the LC filters.

IceBoard

IceBoards are integrated readout boards developed by McGill University. They tune TES bolometers and SQUIDs, acquire signals from TESes, and digitize them.

Since responsivities of SQUIDs are non-linear, they require feedback to be used as linear amplifiers. POLARBEAR-2 adopts Digital Active Nulling (DAN) feedback [37]. Compared to the analog feedback technique used in POLARBEAR, DAN realizes a wider frequency for FDM. DAN signals are generated by IceBoards.

3.4 Overview of calibration

The properties of the receiver must be monitored and calibrated in observation phase at the site. KEK leads the development of calibrators and time-ordered data (TOD) calibration using those devices.

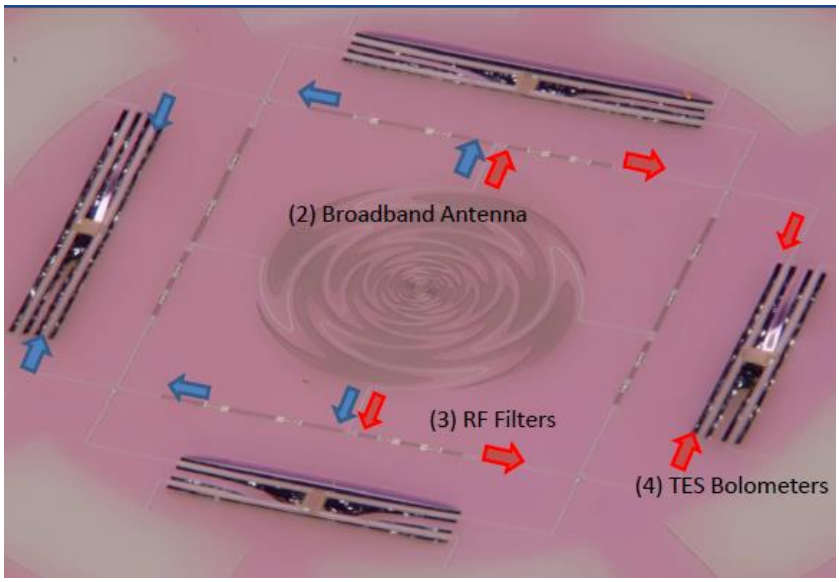

Figure 3.11: A picture of a detector with a sinuous antenna, RF filters and 4 TES bolometers to detect two polarization states for two frequencies.

Low-frequency temperature fluctuation: Temperature monitors

The temperature fluctuation of instruments modulates the detector signal in various ways. It causes $1/f$ noise and suppress the sensitivity at low frequency. We evaluated the temperature dependence of the signal for major components and developed temperature monitors to calibrate the fluctuation. Later we discuss it in detail.

Gain: Stimulator

POLARBEAR-2 uses a artificial microwave source, called a stimulator, for gain calibration. It is placed behind of the secondary mirror and emits radiation through a small hole on the secondary mirror. It is heated to 700 K and its emission is chopped with a frequency that optimizes TESes' responsivity. This calibration is scheduled before and after each CMB scan set. A new stimulator for POLARBEAR-2 was developed at KEK (Figure 3.13. The "Gain" in this context means a conversion coefficient between a current signal from a TES and the temperature of the CMB.

Optical efficiency: El-nod

The optical efficiency is defined as a ratio of the incremental power measured by a detector to that entering from the window. It is measured by nodding

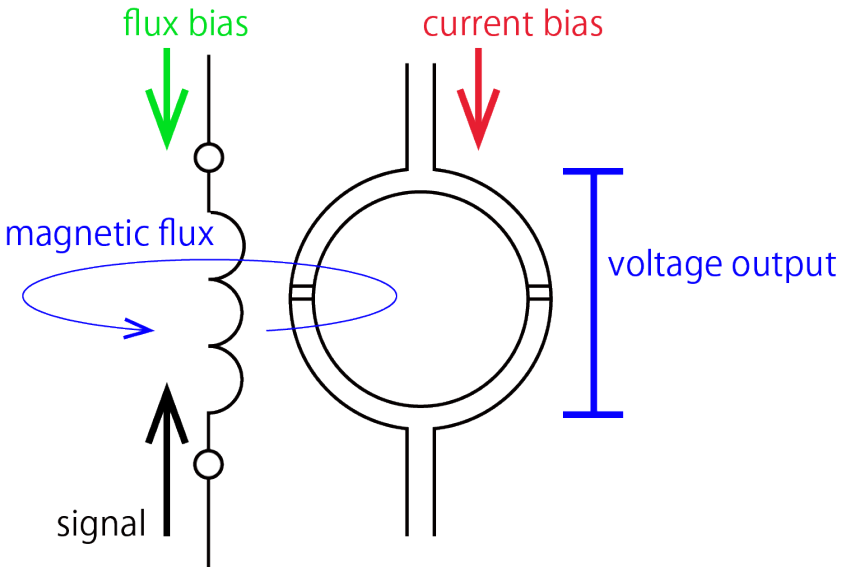

Figure 3.12: A brief sketch of SQUID.

movement of the telescope so called “el-nod". Since this movement changes depth of the atmosphere which the receiver sees, it enables us to evaluate the optical efficiency by modulation of the incident power.

Beam shape: Beam mapper

The shapes of beams of TESes are measured mainly by planets. Jupiter and Venus are used as reference microwave sources. AlThough light enters from the sky to detectors, it is convenient to discuss characters of detectors in a picture of a “beam" emitted from each detector sweeps the sky. Shapes of the beams are expected to be close to the Gaussian distribution. We measure centers, FWHMs, and shapes of the beams by showing the planets to TESes.

Readout assignment: Coherent source

A TES for POLARBEAR-2 is designed to be sensitive to a frequency band centered at 90 or 150 GHz, and two TESes are coupled in a pixel to be sensitive to an orthogonal polarization angles like + shape or × shape. The fMUX readout strategy, however, makes confusion in channel assignment of the TESes because it does not assign one lead to one detector mechanically. The frequency band and polarization angle of TESes are confirmed by a coherent source (Figure 3.14). It is designed at KEK to emit polarized light from rotatable source. It can quickly check the character of TESes because it excites pre-tuned TESes.

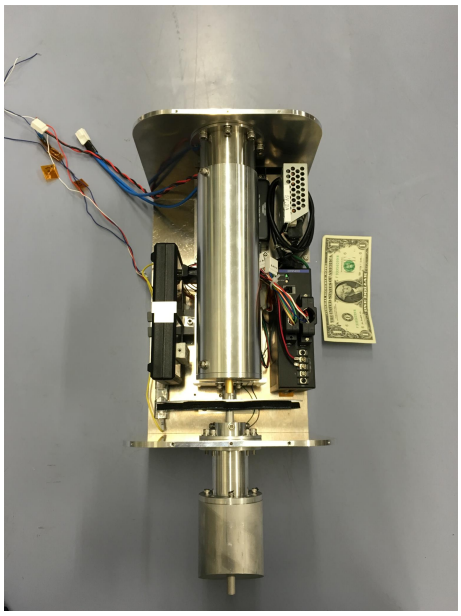

Figure 3.13: Stimulator.

Polarization angle: Tau-A and Wire grid

The polarization angle of TES array is calibrated by Tau-A (Crab Nebula, suprnova remnant) and an artificial wire grid. Tau-A is a polarized microwave source. It modulates light and is useful to check TESes' accuracy for polarization angle measurements. Especially liquid nitrogen is used to check polarization angles.

3.5 Readout operation

3.5.1 Tuning of TES and SQUID

TESes and SQUIDs must be tuned at the best operational point. The operational point of TES is parameterized by fractional resistance, or "R_{frac}", which is the ratio between the resistance in its transition edge and that in the normal conduction. TESes should be tuned to the R_{frac} that realizes the fastest response and the largest number of available TESes. The Operational point of SQUID is determined as the steepest point in the V-ϕ curve, which is the relationship between the output voltage and the magnetic flux.

The tuning process is controlled by IceBoards but there is a challenge of keeping many TESes in the transition edge without completely dropping them into a superconducting state. A TES which dropped into a superconducting state is called “latched" and cannot be used for observation until

Figure 3.14: Coherent source for checking band and polarization angle.

the next tuning.

3.5.2 Fridge control

The cryostat fridge has to be controlled to realize the fastest cooling and longest "hold time". Components in the POLARBEAR-2 receiver below 4 K are cooled by a CRC10-033 sorption cooler designed and manufactured by Simon Chase Ltd. Its cooling process consists of ^{4}He cycle followed by ^{3}He cycle.

Hold time, a duration that the each cryogenic stage in the cryostat is at the target temperature, lasts as long as liquid ^{3}He remains and vaporizes. In order to repeat the standard 24 hours schedule, the hold time needs to be 18 hours, which is 24 hours minus the typical fridge cycle time of 6 hours. When all ^{3}He vaporizes, the temperature of the cryostat starts rising so we have to run a new cycle again.

3.6 Housekeepings

The housekeeping data of receiver and telescope are acquired by various monitoring systems, compressed on site and distributed to Japan and US as well as detector data. Many new monitoring instruments were added for POLARBEAR-2 in order to investigate the effect from the observational environment and to check the stability of the observation. The collected data include instrumental temperature, weather, pointing of the telescope, pressure of Helium, heater voltage of the refrigerator, spinning velocity of the WHWP, power of the stimulator, status of the power generators and others.

A central "aggregator" module communicates to many other modules and compress the data into an integrated package assigned to each observation.

The large measurement devices are installed in boxes hanging on the two sides of the receiver. These boxes are called "saddlebag". Two "MUX" (multiplex) saddlebags hold IceBoards and temperature monitoring system for them, and other two "AUX" (auxiliary) saddlebags are filled with many temperature monitors and miscellaneous monitoring devices.

Since the sampling rate of these housekeeping is relatively slower than that of detector readout, an entire data-acquisition (DAQ) system for housekeeping is named "slowdaq".

3.6.1 Thermometry

For our upsized cryostat of POLARBEAR-2, we need to monitor temperature of many components carefully. The temperature data is referred for many purposes; monitoring the cooling status, confirming the heat links, evaluating the effect of telescope vibration and correcting the variation of detector signal. We use different types of thermometers and measurement modules for various temperature area.

As we mention in Chapter 5.1, PS302J thermistors manufactured by Littelfuse Inc. are attached in 300 K area in addition to onewire thermistors used in POLARBEAR. The thermistors are read by a Keysight 34980A digital multimeter and a 34925A opt-isolator. The 300 K area includes mirrors, telescope booms and readout electronics.

The receicer cryostat has three thermal layers of 50 K, 4 K and 0.3 K. We use lead wires made of phosphor bronze in order to mitigate thermal injection to the cryostat. The 50 K area is measured by Lakeshore PT-103 resistance temperature sensors and Lakeshore 218 diode temperature monitors. The 4 K area is measured by Lakeshore DT-670 diode temperature sensors by the same measurement modules. For 0.3 K area, Lakeshore RX-102A or RX-202A resistance temperature sensors were installed. These RX- type thermometers are made of Ruthenium oxide. They are read by a Lakeshore 370 AC resistance bridge and a 3716 scanner. The thermometer locations on the telescope and sensor types are listed in Table 3.3.

3.7 Extension to Simons Array and beyond

POLARBEAR-2 is planned to be a part of the Simons Array project. The Simons Array is an experiment which will observe the CMB B-mode with three telescopes in the Atacama highland. Three telescopes have already been built. The first receiver (POLARBEAR-2a) will be mounted on one of them in 2018. Other two receivers (POLARBEAR-2b and POLARBEAR-2c) are in preparation in US and will be mounted on remaining two telescopes later. POLARBEAR-2a and POLARBEAR-2b are sensitive to both of 90

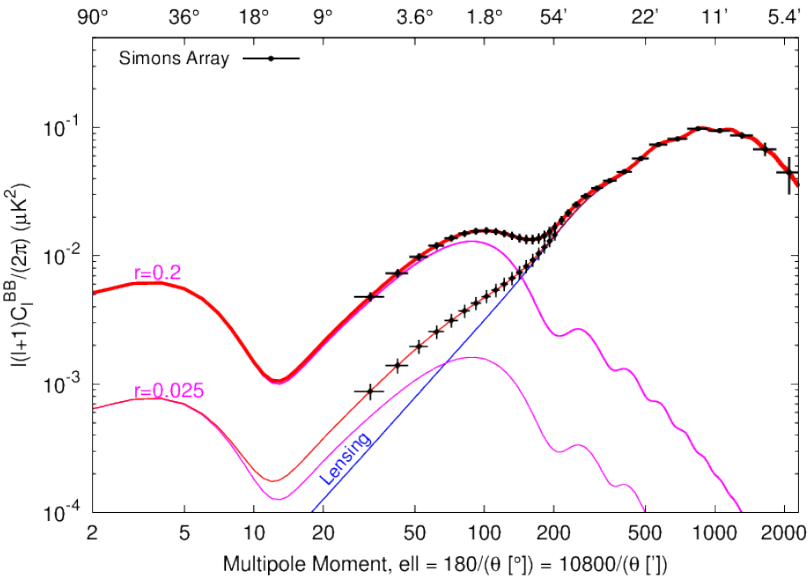

Figure 3.15: Simulated power spectra and expected sensitivities of Simons Array.

and 150 GHz. POLARBEAR-2c is sensitive to 150 and 220 GHz. The Simons Array will carry out observation for three years. From three years data with three telescopes, we expect to search for r down to 0.006 and $\sum_\nu m_\nu$ down to 40 meV [14]. Sensitivity of the Simons Array to r is shown in Figure 3.15.

Furthermore, the POLARBEAR group is planning to collaborate with the ACT group to establish the Simons Observatory project in the future.

Temperature	location	Thermometer	Module
300 K	primary mirror secondary mirror RF box MUX1 readout crate MUX2 readout crate	thermistor×12, onewire×2 thermistor×12 thermistor×3 thermistor×2 thermistor×2	Keysight 34980A +34925A
50 K	optics tube PTC head optics tube PTC heat link optics tube back left optics tube back right optics tube middle tube IR filter left IR filter right backend PTC head backend bottom	PT103	Lakeshore 218×2
4 K	optics tube PTC head optics tube PTC heat link optics tube black body aperture lens Lyot stop field lens IR filter optics tube middle tube optics tube back left optics tube back right Lyot black body Collimator lens backend PTC head backend PTC heat link backend front backend bottom backend right backend harness backend Cu bar left backend Cu bar right SQUID card	DT-670	Lakeshore 218×4
0.3 K	350 mK stage 2 K ring 250 mK support 250 mK stage 2 K jig LC card 350 mK jig metal mesh filter LC tower	RX-102A RX-102A RX-102A RX-102A×3, RX-202A×1 RX-102A RuO_2 sensors×2 RX-102A RX-202A RX-102A	Lakeshore 370 +3716

Table 3.3: Thermometer locations on the POLARBEAR-2 telescope system.

4

Requirements to the temperature monitor

4.1 Principle to calculate requirements

The detector signal is modulated by the temperature of various instruments. In this chapter, we describe dominant components and their mechanisms of modulating detector signal.

- Focal plane: Thermal conduction and responsivity of TES
- Lyot stop: Optical loading
- Mirror: Polarization generated by reflection & polarized emission
- Readout electronics: Gain fluctuation of converters and filters

We want to suppress the noise originating from temperature fluctuation below the statistical array sensitivity level. Since these noises correlate among all detectors, we cannot mitigate it by just averaging the signals. We require the temperature stability to be lower than the ratio between the polarization sensitivity of a detector array and the signal temperature dependence.

$$\mathrm{NSD}\left[\mathrm{T_{instr}}\right] < \frac{\text{array sensitivity (NEPol)}}{\text{temperature coefficient} = \mathrm{A_{instr}} \equiv \Delta\mathrm{T_{signal}}/\Delta\mathrm{T_{instr}}}. \quad (4.1)$$

When the instrumental temperature fluctuation $\Delta\mathrm{T_{instr}}$ is smaller than the absolute temperature, we can express the temperature dependence as a single coefficient. The requirement is obtained as noise spectrum density (NSD) at a frequency of interest, in a unit of $\mathrm{K}\sqrt{\mathrm{s}}$.

The frequency of interest is determined by the typical angular scale of inflationary B-mode and a telescope scan speed. Since the inflationary B-mode is expected to have a bump at $\ell \sim 100$ (1.8° scale), we need to know the

power spectrum around this angular scale to verify the inflationary signal. We impose requirements on $\ell \sim 50$ (3.6° scale), which is a larger neighbor point of $\ell \sim 100$. To measure the correlation of B-mode in this angular scale, we need to focus on the frequency corresponding to the observation of 7.2°. Note that the metric of ℓ is an angle between peak and valley, being different from that of waves because ℓ is originally a degree of spherical harmonics functions. The azimuthal scan speed of POLARBEAR was $0.4°/s$ so that it takes 20 seconds to scan this angular scale [38].

In the following sections, we calculate each instrument's temperature coefficient to obtain requirements at 50 mHz.

4.2 Signal models

The detector signal is a product of input power and gain [39], plus the bias current, $I_{\rm elec}$, generated by readout electronics to keep the TES at the transition edge. Its general form is

$$d = g\left[\Delta P\left[\Delta T\right]\right] \times \Delta P\left[\Delta T\right] + \Delta N, \tag{4.2}$$

where g is a gain or a responsivity from incident power to current. The fluctuation of incident power, ΔP, is a function of various temperature fluctuation denoted by ΔTs. The gain depends on the incident power through the TES non-linearity. The last term, ΔN, is white noise.

We use the stimulator to calibrate the gain before and after each observation. It fluctuates by some instrumental effects during an observation. We describe it as follows in terms of the sky signal, the focal plane temperature, readout temperature, and the detector's non-linearity,

$$g = g_0\left\{1 + A_{\rm resp}\Delta T_{\rm bath} + A_{\rm read}\Delta T_{\rm elec} + g_1\left(\Delta P_{\rm int} + \Delta P_{\rm pol,HWP}\right)\right\}. \tag{4.3}$$

Here, g_0 is a gain baseline, which we can calibrate, $\Delta T_{\rm bath}$ is temperature fluctuation of the focal plane working as a thermal bath for detectors, and $\Delta T_{\rm elec}$ is temperature fluctuation of readout electronics. A parameter $A_{\rm resp}$[1] is a coefficient between the bath temperature and the TES responsivity, and $A_{\rm read}$ is a coefficient of the readout gain. The $\Delta P_{\rm int}$ and $\Delta P_{\rm pol}$ are unpolarized and polarized incident power except for offset-like unpolarized loading. They cause gain fluctuation through the first-order coefficient of TES non-linearity, g_1. The non-linearity has been estimated to be $g_1 = -0.17(-0.42)\%/\mathrm{K}$ at 90(150) GHz for POLARBEAR-2 [39]. Since these values depend on the model of TES, we use conservatively $g_1 \simeq -1\%/\mathrm{K}$.

As the sources of the incident power fluctuation, we consider those from the sky temperature $T_{\rm sky}$, the focal plane temperature $T_{\rm bath}$, the Lyot stop

[1] In the following, the unit of coefficients denoted by A-s is an inverse of time.

temperature $T_{\rm Lyot}$, the mirror temperature $T_{\rm mirror}$, and the spatial fluctuation of CMB polarization, ΔQ. In the following, we discuss the relationship between them and the signal fluctuation by introducing temperature coefficients.

Each component's contribution slightly differs whether we use a rotating half-wave plate (HWP) or not. With an HWP, the unpolarized and polarized signals are obtained from each detector by demodulation. When an HWP rotates with a frequency f, the polarization is modulated with $2f$ and $4f$. We can also obtain the unpolarized signal, $0f$, by applying a low-pass filter. The performance of HWP used for POLARBEAR is described by Takakura et al. [33]. In a case without an HWP, we obtain a polarized signal by taking the difference of detector pair in the same pixel.

4.2.1 With HWP

The unpolarized incident power, $\Delta P_{\rm int}$, is

$$\Delta P_{\rm int} = B_{\rm refl}\Delta T_{\rm sky} + B_{\rm drop}\Delta T_{\rm bath} + B_{\rm Lyot}\Delta T_{\rm Lyot} + B_{\rm mirror,I}\Delta T_{\rm mirror}. \quad (4.4)$$

Here, $B_{\rm refl}$, $B_{\rm drop}$, $B_{\rm Lyot}$, and $B_{\rm mirror,I}$ are dimensionless coefficients for the intensity component of reflection of the sky radiation, an effect of power drop from a TES to the focal plane, radiation from Lyot stop, and intensity emission from the mirror, respectively. Also, fluctuation of the bias current applied to TESs is accounted for in the unpolarized signal.

We use the demodulated signal from $4f$ as the polarized signal. Here we write it as d_P. It is described as

$$\Delta P_{\rm pol,HWP} = C_{\rm pol} + \Delta Q + B_{\rm leak}\Delta T_{\rm sky} + B_{\rm mirror,P}\Delta T_{\rm mirror}, \quad (4.5)$$

where $C_{\rm pol}$ is a stable (DC) component of polarization generated from the reflection of the sky radiation and emission from the mirror. The coefficient $B_{\rm leak}$ is a parameter of optical leakage, which is the fraction of polarization generated from sky temperature by reflection on the mirror surface, as we explain later. The coefficient $B_{\rm mirror,P}$ is for the mirror's polarized emission.

Therefore the unpolarized and polarized signals are

$$\begin{aligned} d_I &= g\cdot\Delta P_{\rm int} + A_{\rm bias}\Delta T_{\rm read}I_{\rm bias} + \Delta N_0 \\ &= g_0\left\{1 + A_{\rm resp}\Delta T_{\rm bath} + A_{\rm read}\Delta T_{\rm read} + g_1\left(\Delta P_{\rm int} + \Delta P_{\rm pol,HWP}\right)\right\}\cdot\Delta P_{\rm int} \\ &\quad + A_{\rm bias}\Delta T_{\rm read}I_{\rm bias} + \Delta N_0 \\ &\simeq g_0\left(1 + g_1 C_{\rm pol}\right)\left\{B_{\rm refl}\Delta T_{\rm sky} + B_{\rm drop}\Delta T_{\rm bath} + B_{\rm Lyot}\Delta T_{\rm Lyot}\right. \\ &\quad \left. + B_{\rm mirror,I}\Delta T_{\rm mirror}\right\} + A_{\rm bias}\Delta T_{\rm read}I_{\rm bias} + \Delta N_0, \end{aligned} \quad (4.6)$$

$$
\begin{aligned}
d_{P,\mathrm{HWP}} &= g \cdot \Delta P_{\mathrm{pol,HWP}} + \Delta N_4 \\
&= g_0 \left\{1 + A_{\mathrm{resp}} \Delta T_{\mathrm{bath}} + A_{\mathrm{read}} \Delta T_{\mathrm{read}} + g_1 \left(\Delta P_{\mathrm{int}} + \Delta P_{\mathrm{pol,HWP}}\right)\right\} \cdot \Delta P_{\mathrm{pol,HWP}} + \Delta N_4 \\
&\simeq g_0 \left\{C_{\mathrm{pol}} + \Delta Q + B_{\mathrm{leak}} \Delta T_{\mathrm{sky}} + B_{\mathrm{mirror,P}} \Delta T_{\mathrm{mirror}} + A_{\mathrm{resp}} C_{\mathrm{pol}} \Delta T_{\mathrm{bath}}\right. \\
&\quad + A_{\mathrm{read}} C_{\mathrm{pol}} \Delta T_{\mathrm{read}} + g_1 C_{\mathrm{pol}} \left(C_{\mathrm{pol}} + \Delta Q + \left(B_{\mathrm{refl}} + B_{\mathrm{leak}}\right) \Delta T_{\mathrm{sky}}\right. \\
&\quad \left.\left. + B_{\mathrm{drop}} \Delta T_{\mathrm{bath}} + B_{\mathrm{Lyot}} \Delta T_{\mathrm{Lyot}} + \left(B_{\mathrm{mirror,I}} + B_{\mathrm{mirror,P}}\right) \Delta T_{\mathrm{mirror}}\right)\right\} + \Delta N_4. \\
&= g_0 \left\{\left(1 + g_1 C_{\mathrm{pol}}\right) \left(C_{\mathrm{pol}} + \Delta Q\right) + \left\{B_{\mathrm{leak}} + g_1 C_{\mathrm{pol}} \left(B_{\mathrm{refl}} + B_{\mathrm{leak}}\right)\right\} \Delta T_{\mathrm{sky}}\right. \\
&\quad + A_{\mathrm{read}} C_{\mathrm{pol}} \Delta T_{\mathrm{read}} + \left(A_{\mathrm{resp}} + g_1 B_{\mathrm{drop}}\right) C_{\mathrm{pol}} \Delta T_{\mathrm{bath}} + g_1 B_{\mathrm{Lyot}} C_{\mathrm{pol}} \Delta T_{\mathrm{Lyot}} \\
&\quad \left. + \left\{B_{\mathrm{mirror,P}} + g_1 C_{\mathrm{pol}} \left(B_{\mathrm{mirror,I}} + B_{\mathrm{mirror,P}}\right)\right\} \Delta T_{\mathrm{mirror}}\right\} + \Delta N_4.
\end{aligned}
\tag{4.7}
$$

We ignored all square terms of fluctuation indicated by Δ. The bias current applied to TESs in the temperature unit, I_{bias}/g_0, is designed to be $\sim$20 K at POLARBEAR-2. Its fluctuation arises from the temperature fluctuation of readout electronics, ΔT_{read}, with a coefficient A_{bias}. White noise in d_I and $d_{P,\mathrm{HWP}}$ is represented by ΔN_0 and ΔN_4, respectively.

Since we obtain d_I and $d_{P,\mathrm{HWP}}$ from the same detector, we can perform principal component analysis (PCA) to cancel the unknown ΔT_{sky}. It reduces some of other temperature coefficients which appear in $d_{P,\mathrm{HWP}}$.

$$
\begin{aligned}
\frac{d_{\mathrm{PCA}}}{g_0} &\equiv \frac{d_{P,\mathrm{HWP}}}{g_0} - \frac{B_{\mathrm{leak}} + g_1 C_{\mathrm{pol}} \left(B_{\mathrm{refl}} + B_{\mathrm{leak}}\right)}{\left(1 + g_1 C_{\mathrm{pol}}\right) B_{\mathrm{refl}}} \frac{d_I}{g_0} \\
&= \left(1 + g_1 C_{\mathrm{pol}}\right) \left(C_{\mathrm{pol}} + \Delta Q\right) \\
&\quad + \left\{\left(A_{\mathrm{resp}} + g_1 B_{\mathrm{drop}}\right) C_{\mathrm{pol}} - \frac{B_{\mathrm{leak}} + g_1 C_{\mathrm{pol}} \left(B_{\mathrm{refl}} + B_{\mathrm{leak}}\right)}{\left(1 + g_1 C_{\mathrm{pol}}\right) B_{\mathrm{refl}}} B_{\mathrm{drop}}\right\} \Delta T_{\mathrm{bath}} \\
&\quad + \left\{g_1 B_{\mathrm{Lyot}} C_{\mathrm{pol}} - \frac{B_{\mathrm{leak}} + g_1 C_{\mathrm{pol}} \left(B_{\mathrm{refl}} + B_{\mathrm{leak}}\right)}{\left(1 + g_1 C_{\mathrm{pol}}\right) B_{\mathrm{refl}}} B_{\mathrm{Lyot}}\right\} \Delta T_{\mathrm{Lyot}} \\
&\quad + \left\{B_{\mathrm{mirror,P}} + g_1 C_{\mathrm{pol}} \left(B_{\mathrm{mirror,I}} + B_{\mathrm{mirror,P}}\right) - \frac{B_{\mathrm{leak}} + g_1 C_{\mathrm{pol}} \left(B_{\mathrm{refl}} + B_{\mathrm{leak}}\right)}{\left(1 + g_1 C_{\mathrm{pol}}\right) B_{\mathrm{refl}}} B_{\mathrm{mirror,I}}\right\} \Delta T_{\mathrm{mirror}} \\
&\quad + \left\{A_{\mathrm{read}} C_{\mathrm{pol}} - \frac{B_{\mathrm{leak}} + g_1 C_{\mathrm{pol}} \left(B_{\mathrm{refl}} + B_{\mathrm{leak}}\right)}{\left(1 + g_1 C_{\mathrm{pol}}\right) B_{\mathrm{refl}}} A_{\mathrm{bias}} \frac{I_{\mathrm{bias}}}{g_0}\right\} \Delta T_{\mathrm{read}} \\
&\quad + \frac{\Delta N_4}{g_0} - \frac{B_{\mathrm{leak}} + g_1 C_{\mathrm{pol}} \left(B_{\mathrm{refl}} + B_{\mathrm{leak}}\right)}{\left(1 + g_1 C_{\mathrm{pol}}\right) B_{\mathrm{refl}}} \Delta N_0.
\end{aligned}
\tag{4.8}
$$

We can treat this as a polarization signal. Each bracket before the temperature fluctuation ΔT-s are the ultimate temperature coefficients which affects on the signal.

With gain reconstruction

When we continuously run the stimulator during an observation and perform gain calibration, we can convert signal current to temperature unit by $1/g = 1/g_0\{1 + A_{\mathrm{resp}} \Delta T_{\mathrm{bath}} + A_{\mathrm{read}} \Delta T_{\mathrm{read}} + g_1(\Delta P_{\mathrm{int}} + \Delta P_{\mathrm{pol,HWP}}) + \Delta g_{\mathrm{meas}}\}$ instead of $1/g_0$. Some temperature coefficient changes due to DC polariza-

tion and uncertainty of gain calibration $\Delta g_{\rm meas}$ is added.

$$\begin{aligned}\frac{d_I}{g} &\simeq \frac{d_I}{g_0}\left\{1 - A_{\rm resp}\Delta T_{\rm bath} - A_{\rm read}\Delta T_{\rm read} - g_1(\Delta P_{\rm int} + \Delta P_{\rm pol,HWP}) - \Delta g_{\rm meas}\right\} \\ &\simeq \left(1 - g_1^2 C_{\rm pol}^2\right)\left\{B_{\rm refl}\Delta T_{\rm sky} + B_{\rm drop}\Delta T_{\rm bath} + B_{\rm Lyot}\Delta T_{\rm Lyot}\right. \\ &\quad \left. + B_{\rm mirror,I}\Delta T_{\rm mirror}\right\} + A_{\rm bias}\Delta T_{\rm read}\frac{I_{\rm bias}}{g_0}\left(1 - g_1 C_{\rm pol}\right) + \frac{\Delta N_0}{g_0}\left(1 - g_1 C_{\rm pol}\right), \end{aligned} \tag{4.9}$$

$$\begin{aligned}\frac{d_{P,\rm HWP}}{g} &\simeq \frac{d_{P,\rm HWP}}{g_0}\left\{1 - A_{\rm resp}\Delta T_{\rm bath} - A_{\rm read}\Delta T_{\rm read} - g_1(\Delta P_{\rm int} + \Delta P_{\rm pol,HWP}) - \Delta g_{\rm meas}\right\} \\ &\simeq \left(1 - g_1^2 C_{\rm pol}^2\right)\left(C_{\rm pol} + \Delta Q\right) - \left(1 + g_1 C_{\rm pol}\right) C_{\rm pol}\Delta g_{\rm meas} \\ &\quad + \left[-2g_1^2 C_{\rm pol}^2\left(B_{\rm leak} + B_{\rm refl}\right) + B_{\rm leak}\left(1 - g_1 C_{\rm pol}\right)\right]\Delta T_{\rm sky} \\ &\quad -2g_1 C_{\rm pol}^2\left(A_{\rm resp} + g_1 B_{\rm drop}\right)\Delta T_{\rm bath} - 2g_1^2 C_{\rm pol}^2 B_{\rm Lyot}\Delta T_{\rm Lyot} - 2g_1 C_{\rm pol}^2 A_{\rm read}\Delta T_{\rm read} \\ &\quad + \left[-2g_1^2 C_{\rm pol}^2\left(B_{\rm mirror,I} + B_{\rm mirror,P}\right) + B_{\rm mirror,P}\left(1 - g_1 C_{\rm pol}\right)\right]\Delta T_{\rm mirror} \\ &\quad + \frac{\Delta N_4}{g_0}\left(1 - g_1 C_{\rm pol}\right). \end{aligned} \tag{4.10}$$

$$\begin{aligned}\frac{d_{\rm GRPCA}}{g} &= \frac{d_{P,\rm HWP}}{g} - \frac{-2g_1^2 C_{\rm pol}^2\left(B_{\rm leak} + B_{\rm refl}\right) + B_{\rm leak}\left(1 - g_1 C_{\rm pol}\right)}{\left(1 - g_1^2 C_{\rm pol}^2\right) B_{\rm refl}}\frac{d_I}{g} \\ &\quad \left(1 - g_1^2 C_{\rm pol}^2\right)\left(1 + \Delta Q\right) - \left(1 + g_1 C_{\rm pol}\right) C_{\rm pol}\Delta g_{\rm meas} \\ &\quad + \left[-2g_1 C_{\rm pol}^2\left(A_{\rm resp} - g_1 B_{\rm drop}\frac{B_{\rm leak}}{B_{\rm refl}}\right) - B_{\rm leak}\left(1 - g_1 C_{\rm pol}\right)\frac{B_{\rm drop}}{B_{\rm refl}}\right]\Delta T_{\rm bath} \\ &\quad + \left[2g_1^2 C_{\rm pol}^2 B_{\rm Lyot}\frac{B_{\rm leak}}{B_{\rm refl}} - B_{\rm leak}\left(1 - g_1 C_{\rm pol}\right)\frac{B_{\rm Lyot}}{B_{\rm refl}}\right]\Delta T_{\rm Lyot} \\ &\quad + \left[-2g_1 C_{\rm pol}^2\left\{A_{\rm read} - g_1\left(B_{\rm leak} + B_{\rm refl}\right)\frac{A_{\rm bias}}{B_{\rm refl}}\frac{I_{\rm bias}}{g_0}\frac{1}{1 + g_1 C_{\rm pol}}\right\}\right. \\ &\quad \left. - B_{\rm leak}\frac{1 - g_1 C_{\rm pol}}{1 + g_1 C_{\rm pol}}\frac{A_{\rm bias}}{B_{\rm refl}}\frac{I_{\rm bias}}{g_0}\right]\Delta T_{\rm read} \\ &\quad + \left[B_{\rm mirror,P}\left(1 - g_1 C_{\rm pol}\right) - 2g_1^2 C_{\rm pol}^2\left(B_{\rm mirror,P} - \frac{B_{\rm leak}}{B_{\rm refl}}B_{\rm mirror,I}\right)\right. \\ &\quad \left. - B_{\rm leak}\left(1 - g_1 C_{\rm pol}\right)\frac{B_{\rm mirror,I}}{B_{\rm refl}}\right]\Delta T_{\rm mirror} \\ &\quad + \frac{1 - g_1 C_{\rm pol}}{g_0}N_4 - \frac{-2g_1^2 C_{\rm pol}^2\left(B_{\rm leak} + B_{\rm refl}\right) + B_{\rm leak}\left(1 - g_1 C_{\rm pol}\right)}{g_0\left(1 + g_1 C_{\rm pol}\right)}N_0. \end{aligned} \tag{4.11}$$

In this case, a requirement to the $\Delta g_{\rm meas}$ is calculated as well as temperature fluctuation.

4.2.2 Without HWP

In a case without HWP, the unpolarized incident power is same as the Eq. (4.4)(4.6) in the with-HWP case but polarization signal slightly differs. The stable polarization $C_{\rm pol}$ is not demodulated so that it is compensated by detector tuning. Instead, difference caused by post-detectoral components,

such as thermal conductance between a detector and the focal plane, are induced by pair difference. The polarized incident power is

$$\Delta P_{\rm pol,pair} = \Delta Q + B_{\rm leak}\Delta T_{\rm sky} + B_{\rm mirror,P}\Delta T_{\rm mirror} + \delta_{\rm cond} B_{\rm drop}\Delta T_{\rm bath}, \quad (4.12)$$

where $\delta_{\rm cond}$ is the variation of dynamic thermal conductance between pair detectors. We assume that $\delta_{\rm cond}$ is at most 20% (See Sec. 4.3.2).

At the signal level, difference of bias current from the readout electronics, $\delta_{\rm bias}$, is seen as polarization. In addition, the unpolarized signal leaks into polarization signal through uncertainty of relative gain, $\delta_{\rm pair}$, which is a ratio of gains of orthogonal detector pair in a pixel. Therefore the polarized signal is

$$\begin{aligned}
d_{P,\rm pair} &= g\cdot\Delta P_{\rm pol,pair} + A_{\rm bias}\Delta T_{\rm read}\delta_{\rm bias} + \delta_{\rm pair} g\cdot\Delta P_{\rm int} + \Delta N_4 \\
&= g_0\left\{1 + A_{\rm resp}\Delta T_{\rm bath} + A_{\rm read}\Delta T_{\rm read} + g_1\left(\Delta P_{\rm int} + \Delta P_{\rm pol,pair}\right)\right\}\cdot\Delta P_{\rm pol,pair} \\
&\quad + A_{\rm bias}\Delta T_{\rm read}\delta_{\rm bias} + \delta_{\rm pair} g_0\left\{1 + A_{\rm resp}\Delta T_{\rm bath} + A_{\rm read}\Delta T_{\rm read}\right. \\
&\quad \left. + g_1\left(\Delta P_{\rm int} + \Delta P_{\rm pol,pair}\right)\right\}\cdot\Delta P_{\rm int} + \Delta N_4 \\
&\simeq g_0\left(\Delta Q + B_{\rm leak}\Delta T_{\rm sky} + B_{\rm mirror,P}\Delta T_{\rm mirror} + \delta_{\rm cond}B_{\rm drop}\Delta T_{\rm bath}\right) \\
&\quad + A_{\rm bias}\Delta T_{\rm read}\delta_{\rm bias} + \delta_{\rm pair} g_0\left\{B_{\rm refl}\Delta T_{\rm sky} + B_{\rm drop}\Delta T_{\rm bath}\right. \\
&\quad \left. + B_{\rm Lyot}\Delta T_{\rm Lyot} + B_{\rm mirror,I}\Delta T_{\rm mirror}\right\} + \Delta N_4 \\
&= g_0\left\{\Delta Q + \left\{B_{\rm leak} + \delta_{\rm pair}B_{\rm refl}\right\}\Delta T_{\rm sky} + \left(\delta_{\rm cond} + \delta_{\rm pair}\right)B_{\rm drop}\Delta T_{\rm bath}\right. \\
&\quad \left. + \delta_{\rm pair}B_{\rm Lyot}\Delta T_{\rm Lyot} + A_{\rm read}\delta_{\rm bias}\Delta T_{\rm read}\right\} \\
&\quad + \left(B_{\rm mirror,P} + \delta_{\rm pair}B_{\rm mirror,I}\right)\Delta T_{\rm mirror} + \Delta N_4.
\end{aligned} \quad (4.13)$$

For seasons without HWP in POLARBEAR experiment, its statistical uncertainty $\delta_{\rm pair}$ has been estimated to be 0.5% [8]. We also estimate $\delta_{\rm bias}$ as 1 K from the experience of POLARBEAR.

The gain reconstruction does not change the coefficients there is no appearance of DC polarization and we ignore all square terms of fluctuation.

4.3 Temperature coefficient of each component

4.3.1 Gain

TES responsivity $A_{\rm resp}$

The gain fluctuation caused by bath temperature, corresponding to the focal plane temperature, is calculated from a model of TES. Here we estimate it by calculation and compare it with measurement.

The responsivity S, a derivative of bias current over optical loading, is [32]

$$S = -\frac{1}{V_{\rm elec}}\frac{\mathcal{L}}{\mathcal{L}+1}\frac{1}{1+i\omega\tau}, \quad (4.14)$$

where $V_{\rm elec}$ is a bias voltage, $\mathcal{L}$ is a loop gain, ω is frequency of perturbation which can be ignored for low-frequency noise and τ is a time constant. Loop

gain is a parameter of strength of electro-thermal feed back of TES, defined as

$$\mathcal{L} \equiv \frac{P_{\rm bath}\alpha}{GT_c}, \quad \alpha \equiv \frac{T_{\rm TES}}{R_{\rm TES}}\frac{\partial R_{\rm TES}}{\partial T_{\rm TES}}, \tag{4.15}$$

where $T_{\rm TES}$, $R_{\rm TES}$ are temperature and resistance of TES, G is thermal conductance between TES and the thermal bath, T_c is a superconducting transition temperature of TES. The $P_{\rm bath}$ is a heat flow from TES to thermal bath with temperature $T_{\rm bath}$ [40],

$$P_{\rm bath} = \frac{G}{nT_{\rm TES}^{n-1}}\left(T_{\rm TES}^n - T_{\rm bath}^n\right), \tag{4.16}$$

where n is an index of thermal conductivity. It takes $n-1=1$ for the case where electrons carries heat, and $n-1=3$ for heat transfer by phonon [32].

A TES is operated near the transition temperature, $T_{\rm TES} = T_c$. From Eqs. (4.14)(4.15)(4.16), a temperature dependence fraction of TES responsivity is

$$\frac{1}{S}\frac{dS}{dT_{\rm bath}} = -\frac{T_{\rm bath}^{n-1}}{T_c^n}\frac{\alpha}{\mathcal{L}\left(\mathcal{L}+1\right)} \equiv A_{\rm resp}. \tag{4.17}$$

Designed parameters for POLARBEAR-2 are $\alpha = 200$, $n = 4$, $V_{\rm elec} = 2.3\mu$V, $\mathcal{L} = 15$, $T_c = 400$mK, $T_b = 270$mK. Substituting these values into Eq. (4.17), we obtain $A_{\rm resp} = -0.64$/K.

Readout gain $A_{\rm read}$, $A_{\rm bias}$

The warm readout system has temperature dependence in digitizing and amplifying components. We use Ice system developed in McGill university as readout electronics at room temperature [41]. It consists of IceBoard motherboards, mezzanine boards and SQUID controller boards (SQCB). A mezzanine board, which is located on an IceBoard, communicates with a field-programmable gate array (FPGA). A SQCB biases the SQUIDs and amplifies the signal from the SQUIDs. All SQCBs are settled in a RF-shielded metal box right on the receiver.

There are briefly two signal paths called "carrier" and "nuller." The "carrier" is voltage bias applied to TESes, which is generated by a mezzanine board. The $A_{\rm bias}$ corresponds to its temperature coefficient. The "nuller" copies current flowing on the TESes and provides feedback to the bias voltage on SQUIDs, thanks of the digital active nulling (DAN) method [37]. The $A_{\rm read}$ is the temperature coefficient of this signal. Fig. 4.1 shows a diagram of this readout system. The carrier are applied through analog-to-digital converters (ADCs). and SQUID signals are amplified by operational amplifiers and then read through digital-to-analog converters (DACs) [42]. Since their gain drifts with temperature, the signal and bias current are also modulated. The temperature effect related to readout electronics, $A_{\rm read}\Delta T_{\rm read}$

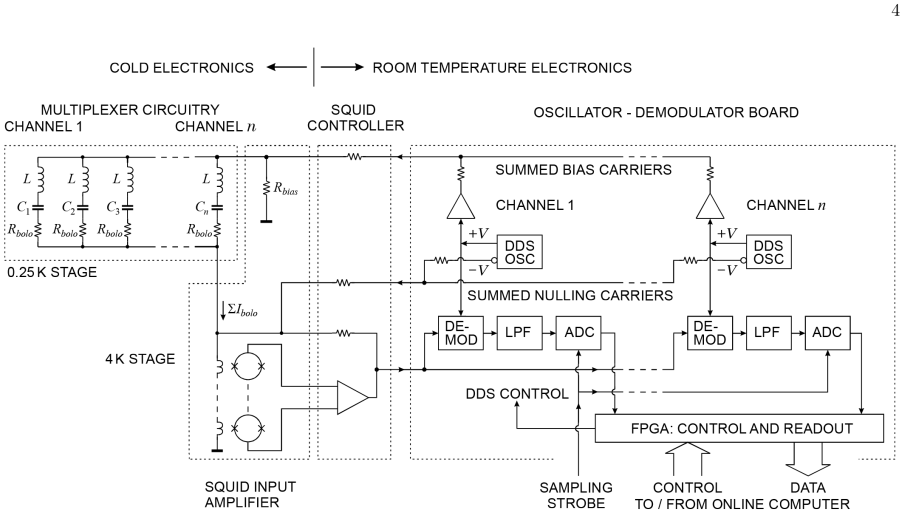

Figure 4.1: Schematic diagram of the Ice readout system. [10]

and $A_{\rm bias}\Delta T_{\rm read}$, can be decomposed to mezzanine and SQCB components as

$$A_{\rm read}\Delta T_{\rm read} = A_{\rm read,mezz}\Delta T_{\rm mezz} + A_{\rm read,SQCB}\Delta T_{\rm SQCB}, \tag{4.18}$$

$$A_{\rm bias}\Delta T_{\rm read} = A_{\rm bias,mezz}\Delta T_{\rm mezz} + A_{\rm bias,SQCB}\Delta T_{\rm SQCB}, \tag{4.19}$$

where the $T_{\rm mezz}$ and $T_{\rm SQCB}$ are temperature fluctuations of mezzanine and SQCB.

Mezzanine board

We measured fluctuations of carrier and nuller current dependent on temperature of the mezzanine board. Constant voltage with 1.6 MHz frequency was set to carrier or nuller and returned through loopback dongles instead of detectors. The ambient temperature was controlled by a thermal chamber PU-3KT provided by ESPEC Inc. Although the temperature in the thermal chamber varied merely from 0°C to 5°C, the temperature of the mezzanine board rose up to 30°C due to heat by itself. We attached a calibrated platinum resistance temperature detector PT103-14L (Serial No. P40816) provided by Lakeshore Inc. to the mezzanine board avoiding to make a short in the circuits. The photo image and temperature distribution of the powered mezzanine board is shown in Fig. 4.2.

We recorded the amplitudes of output signal with changing the ambient temperature, and normalized them by the injected signal. Since the output of one mezzanine board has 64 channels, we averaged them to obtain a typical output signal. The typical carrier and nuller signals are shown in Fig. 4.3 altogether with mezzanine temperature. Then we normalized it by

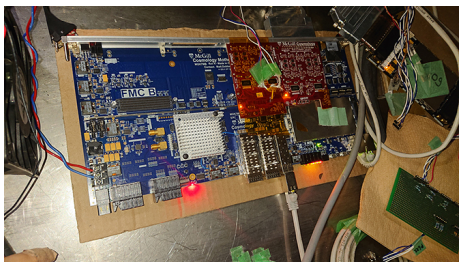

[1] Photo image of an IceBoard. A red mezzanine board is connected on the upper right. A thermometer is attached on the mezzanine.

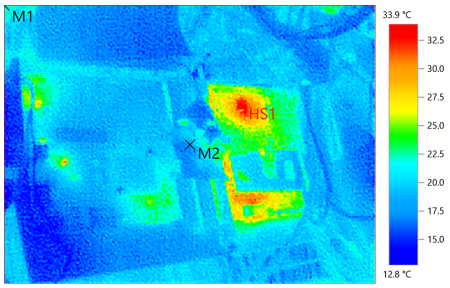

[2] Infrared image of the mezzanine board. A red hot spot indicates the heat dissipation of the mezzanine board.

Figure 4.2: Visible and infrared image of an IceBoard in the KEK thermal chamber. Both of the motherboard and the mezzanine board are turned on.

its mean value and fitted it by linear function of temperature to derive a temperature coefficient. The best-fit temperature coefficients were $A_{\mathrm{bias}} = -493.6 \pm 26.4\mathrm{ppm/K}$ for carrier and $A_{\mathrm{read}} = -484.9 \pm 28.1\mathrm{ppm/K}$. It is consistent with the result of $A_{\mathrm{read}} = -486 \pm 12\mathrm{ppm/K}$, which was measured with the integrated receiver system coupled with TESes in KEK. Therefore we determine the contribution of warm readout electronics as $A_{\mathrm{bias,mezz}} \approx A_{\mathrm{read,mezz}} \approx 5 \times 10^{-4}$.

SQUID controller board

The SQCB has three paths of signal; carrier, nuller and readout amplifier chain. Carrier generated by the mezzanine board is transformed on the SQCB and applied to the TESes. Also nuller is transformed and applied to the feedback coil close to the SQUID. Signal from a SQUID is amplified by two active low-pass filters per channel and handed to the mezzanine board.

We experimentally checked one-way transfer function of three signal paths on a SQCB. We located a SQCB in the thermal chamber and injected 100 mV (peak-to-peak) sinusoidal wave at 1.6 MHz by a function generator into input side of each path, and read the output with an oscilloscope. The power was supplied from the mezzanine board. We changed temperature in the chamber from 273 K to 293 K and recorded the waveforms at various temperature. Then we divided the waveform at each temperature into chunks with 2048 datapoints, calculated amplitude of the signal from the power spectra and averaged the amplitudes over chunks. We show the result in Fig. 4.4. The temperature dependences of carrier and nuller amplitude were consistent with zero, but that of the readout path

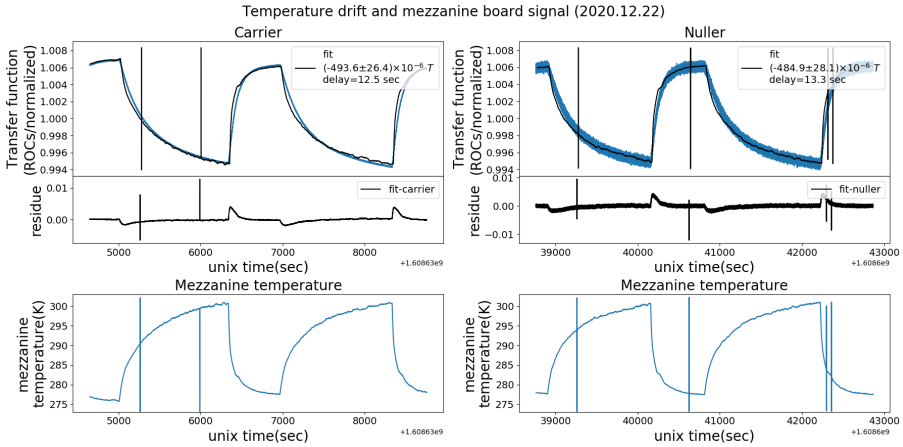

Figure 4.3: The TODs of readout signal returned back through the mezzanine dongle and board temperature. The left figures are for measurement of carrier and the right for nuller. (*top*) *blue line:* TOD normalized by input amplitude. *black line:* Linear fitting by the mezzanine temperature. (*middle*) Residues after subtracting fitting line from the TODs. (*bottom*) Mezzanine board temperature.

was 2324.9±858.5ppm/K.

We can compare the measurement and theoretical calculation of the temperature dependence of the amplifier chain using designed parameters of its components, particularly, resistors and capacitors which provide feedback to the amplifiers.

The two amplifiers on a SQCB form a chain of active low-pass filters (Fig. 4.5). The transfer function of an active low-pass filter is written as

$$\mathrm{TF} = \frac{R_2}{R_1} \frac{\dfrac{1}{R_2 C_1}}{\dfrac{1}{R_2 C_1} + i\omega}, \tag{4.20}$$

where R_1 and R_2 are input and feedback resistances, C is feedback capacitance and ω is input frequency. When we use temperature dependence of each component as systematic error from nominal value, the upper limit of temperature dependence of the transfer function is

$$\begin{aligned} \frac{\Delta|\mathrm{TF}|}{|\mathrm{TF}|} &= \frac{1}{|\mathrm{TF}|}\left|\frac{d|\mathrm{TF}|}{dR_1}\Delta R_1\right| + \frac{1}{|\mathrm{TF}|}\left|\frac{d|\mathrm{TF}|}{dR_2}\Delta R_2\right| + \frac{1}{|\mathrm{TF}|}\left|\frac{d|\mathrm{TF}|}{dC}\Delta C\right| \\ &= \left|-\frac{\Delta R_1}{R_1}\right| + \left|\frac{\Delta R_2}{R_2} - \frac{R_2 C^2\omega^2}{\sqrt{1+R_2^2C^2\omega^2}^3}\Delta R_2\right| + \left|-\frac{R_2^2 C\omega^2}{\sqrt{1+R_2^2C^2\omega^2}^3}\Delta C\right|, \end{aligned} \tag{4.21}$$

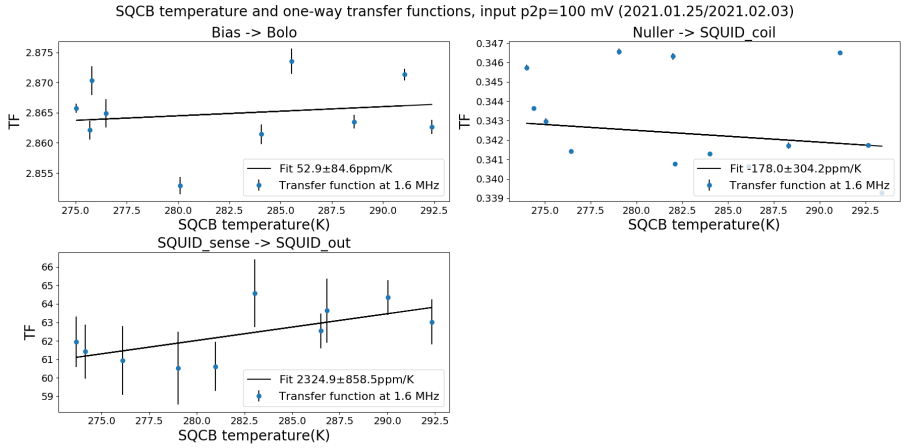

Figure 4.4: The TODs of readout signal returned back through the mezzanine dongle and board temperature. (*top left*) (*top right*) Residue after subtracting fitting line from carrier signal. (*bottom left*)

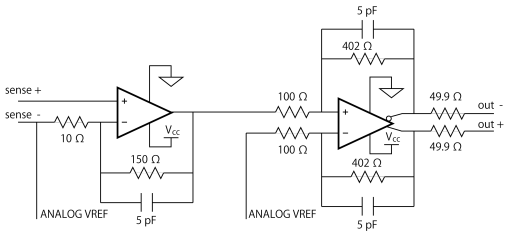

Figure 4.5: A simplified schematic of an amplifier chain of the readout path on a SQCB.

where ΔR_1, ΔR_2 and ΔC are fluctuation in physical units. In our SQCB, The R_1 and R_2 are 10 Ω and 150 Ω for the first amplifier. The second amplifier has positive and negative feedback, whose input resistances are 100 Ω and feedback resistances are 402 Ω. Temperature dependence of all resistors are ±100ppm/K. All capacitors are 5 pF with ±30ppm/K dependence.

When the input frequency is 1.6 MHz, the DC transfer function of the first amplifier is 15.0 and the second is 4.02 in according to Eq. (4.20). Therefore the total gain is 64.32. The maximum temperature dependence of the transfer function is calculated by Eq. (4.21) as 200ppm/K for each of three feedbacks, dominated by those of the resistors. Accounting the temperature dependence of resistors right before the output, which are 49.9 Ω with ±100ppm/K dependence, the fluctuation of the total transfer function becomes ±800ppm/K.

In addition to the temperature dependence of amplifier chain itself, there is a fluctuation of an analog reference voltage provided by a DAC. Assuming

temperature dependence of the DAC is same level as that of ADCs on the mezzanine board, namely ±500ppm/K, the fluctuation of the entire path becomes ±1300ppm/K at most. Remaining difference between measured and calculated temperature dependence can be caused by fluctuation of power supplied from the mezzanine board. However, the temperature dependence of the amplifier chain is possibly suppressed by DAN and does not appear in the demodulated signal [43].

4.3.2 Input sources

Emission and reflection from the mirror $B_{\mathrm{mirror,I}}$, $B_{\mathrm{mirror,P}}$

Reflection and absorption of radiation caused on the mirror surface is formulated based on Fresnel's law. The incident and reflection can be decomposed into two polarization direction; one is s-wave which is perpendicular to the plane of emission and the other is s-wave which is parallel to the plane. Strozzi et al [44] describes radiation with frequency ν and temperature T emitted from a mirror to vacuum. The emission power P_{emission} is described by absorption coefficient $\mathcal{A}$ and reflection coefficient $\mathcal{R}$ as

$$\begin{aligned} P_{\mathrm{emission}} = \mathcal{A}\frac{h\nu^3/c^2}{e^{h\nu/kT}-1} &= (1-\mathcal{R})\frac{h\nu^3/c^2}{e^{h\nu/kT}-1} \\ &\simeq (1-\mathcal{R})\frac{k_BT}{\lambda^2}. \end{aligned} \tag{4.22}$$

Here k is the Boltzmann's constant. The last transformation is Rayleigh-Jeans approximation which is valid for low-frequency radiation satisfying $h\nu \ll kT$. Under this approximation, we can regard k/λ^2 as a conversion coefficient from temperature to power.

When the reflection angle is θ $(0 < \theta < \pi/2)$ and resistivity of the mirror surface is ρ, the reflection coefficient of each polarization mode are

$$\mathcal{R}_s = 1 - 2\sqrt{4\pi\rho\nu\epsilon_0}\cos\theta, \quad \mathcal{R}_p = 1 - 2\sqrt{4\pi\rho\nu\epsilon_0}\frac{1}{\cos\theta}, \tag{4.23}$$

where ϵ_0 is permittivity of vacuum. These are reflective fraction of incident power. An absorption coefficient is the residual,

$$\mathcal{A}_s = 1 - \mathcal{R}_s = 2\sqrt{4\pi\rho\nu\epsilon_0}\cos\theta, \quad \mathcal{A}_p = 1 - \mathcal{R}_p = 2\sqrt{4\pi\rho\nu\epsilon_0}\frac{1}{\cos\theta}, \tag{4.24}$$

which is equal to emissivity. Since the polarization in total is the difference of these coeffcients, the polarized reflection observed by receiver is [45]

$$\begin{aligned} P_{\mathrm{reflection,P}} &= \frac{\mathcal{R}_s - \mathcal{R}_p}{2}\frac{k}{\lambda^2}T_{\mathrm{sky}} \\ &= \sqrt{4\pi\rho\nu\epsilon_0}\frac{\sin^2\theta}{\cos\theta}\frac{k}{\lambda^2}T_{\mathrm{sky}}. \end{aligned} \tag{4.25}$$

Eq. (4.25) indicates that the unpolarized sky radiation get polarized after it is reflected by the mirror. This effect is called optical leakage [46] and we denote the coefficient as $\mu_{\rm opt}$.

$$\mu_{\rm opt} \equiv \sqrt{4\pi\rho\nu\epsilon_0}\frac{\sin^2\theta}{\cos\theta}. \tag{4.26}$$

Substituting $\rho = 2.417\times10^{-8}\ \Omega\cdot$m at 273 K [47], $\nu = 85.2(143.9)$ GHz [48] and $\theta = 32.5°$[39], we obtain $\mu_{\rm opt} \sim 0.016(0.021)\%$.

The unpolarized reflection is the residual after subtracting polarization from the total reflection,

$$\begin{aligned} P_{\rm reflection,I} &= \frac{\mathcal{R}_s + \mathcal{R}_p - (\mathcal{R}_s - \mathcal{R}_p)}{2}\frac{k}{\lambda^2}T_{\rm sky} \\ &= \left(1 - \frac{2\sqrt{4\pi\rho\nu\epsilon_0}}{\cos\theta}\right)\frac{k}{\lambda^2}T_{\rm sky}. \end{aligned} \tag{4.27}$$

On the other hand, there is subtle polarization in the emission from the mirror with temperature $T_{\rm mirror}$. Using coefficients in Eq. (4.24),

$$\begin{aligned} P_{\rm emission,P} &= (\mathcal{A}_s - \mathcal{A}_p)\frac{1}{2}T_{\rm mirror} \\ &= -\sqrt{4\pi\rho\nu\epsilon_0}\frac{\sin^2\theta}{\cos\theta}\frac{k}{\lambda^2}T_{\rm mirror} \\ &= -\mu_{\rm opt}\frac{k}{\lambda^2}T_{\rm mirror}. \end{aligned} \tag{4.28}$$

The negative sign indicates that the direction of this polarization is perpendicular to the reflection of the sky radiation, due to difference of $\mathcal{R}s$ and $\mathcal{A}s$.

The unpolarized emission is the residual from the total emission like

$$\begin{aligned} P_{\rm emission,I} &= \frac{\mathcal{A}_s + \mathcal{A}_p - (\mathcal{A}_p - \mathcal{A}_s)}{2}\frac{k}{\lambda^2}T_{\rm mirror} \\ &= 2\sqrt{4\pi\rho\nu\epsilon_0}\cos\theta\frac{k}{\lambda^2}T_{\rm mirror}. \end{aligned} \tag{4.29}$$

Thus the polarized and unpolarized light from the mirror are

$$\begin{aligned} P_{\rm mirror,pol} &= |P_{\rm emission,P} + P_{\rm reflection,P}| \\ &= \mu_{\rm opt}\frac{k}{\lambda^2}\left(T_{\rm mirror} - T_{\rm sky}\right), \end{aligned} \tag{4.30}$$

$$\begin{aligned} P_{\rm mirror,unpol} &= P_{\rm emission,I} + P_{\rm reflection,I} \\ &= \left(1 - \frac{2\sqrt{4\pi\rho\nu\epsilon_0}}{\cos\theta}\right)\frac{k}{\lambda^2}T_{\rm sky} + 2\sqrt{4\pi\rho\nu\epsilon_0}\cos\theta\frac{k}{\lambda^2}T_{\rm mirror} \\ &= \left(1 - \frac{2}{\sin^2\theta}\mu_{\rm opt}\right)\frac{k}{\lambda^2}T_{\rm sky} + \frac{2}{\tan^2\theta}\mu_{\rm opt}\frac{k}{\lambda^2}T_{\rm mirror}. \end{aligned} \tag{4.31}$$

They are converged to temperature unit by factor of λ^2/k. Eq. (4.30) corresponds to DC polarization, $C_{\rm pol}$, shown in Eq. (4.5).

$$C_{\rm pol} \equiv \mu_{\rm opt} \left(T_{\rm mirror} - T_{\rm sky}\right). \tag{4.32}$$

Assuming $T_{\rm mirror} = 273$ K and $T_{\rm sky} = 10$ K, the $C_{\rm pol}$ is 43(56) mK and the unpolarized signal is 10.2(10.2) K.

The mirror temperature dependence of these emission and reflection are caused by the temperature dependence of resistivity ρ as well as the explicit $T_{\rm mirror}$ term. The resistivity of mirrors of POLARBEAR-2, which are made of aluminum, has slight temperature dependence. Therefore the temperature derivative of the optical leakage parameter is

$$\frac{d\mu_{\rm opt}}{dT_{\rm mirror}} = \sqrt{4\pi\rho\nu\epsilon_0}\frac{1}{2}\frac{d\ln\rho}{dT_{\rm mirror}}\frac{\sin^2\theta}{\cos\theta} = \frac{1}{2}\frac{d\ln\rho}{dT_{\rm mirror}}\mu_{\rm opt}. \tag{4.33}$$

The temperature dependence of aluminum resistivity is $d\ln\rho/dT \sim 0.004$.

Summarizing above, we obtain temperature coefficients $B_{\rm mirror,I}$, $B_{\rm mirror,P}$ and $B_{\rm leak}$ by temperature derivatives of Eqs. (4.30)(4.31).

$$B_{\rm mirror,P} = \frac{\lambda^2}{k}\frac{dP_{\rm mirror,pol}}{dT_{\rm mirror}} = \frac{1}{2}\frac{d\ln\rho}{dT_{\rm mirror}}\mu_{\rm opt}\left(T_{\rm mirror} - T_{\rm sky}\right) - \mu_{\rm opt} \sim 0.00025(0.00032), \tag{4.34}$$

$$B_{\rm leak} = \frac{\lambda^2}{k}\frac{dP_{\rm mirror,pol}}{dT_{\rm sky}} = -\mu_{\rm opt} \sim -0.00016(-0.00021), \tag{4.35}$$

$$\begin{aligned} B_{\rm mirror,I} = \frac{\lambda^2}{k}\frac{dP_{\rm mirror,unpol}}{dT_{\rm mirror}} &= -\frac{2}{\sin^2\theta}\frac{1}{2}\frac{d\ln\rho}{dT_{\rm mirror}}\mu_{\rm opt}T_{\rm sky} \\ &\quad + \frac{2}{\tan^2\theta}\mu_{\rm opt}\left(\frac{1}{2}\frac{d\ln\rho}{dT_{\rm mirror}}T_{\rm mirror} + 1\right) \sim 0.0012(0.0016), \end{aligned} \tag{4.36}$$

$$B_{\rm refl} = \frac{\lambda^2}{k}\frac{dP_{\rm mirror,unpol}}{dT_{\rm sky}} = 1 - \frac{2}{\sin^2\theta}\mu_{\rm opt} \sim 1.0(1.0). \tag{4.37}$$

Emission from the Lyot stop $B_{\rm Lyot}$

Emission from cold optical elements behaves as additional loading. An optical element emits radiation in proportion to its emissivity, and the emission is attenuated by other elements on the way to the detectors. The power from the i-th element, counted from the detector side, is [34]

$$P_i = \int \frac{\epsilon_i \eta_i^c h\nu}{\exp\left(h\nu/kT_i - 1\right)} d\nu, \tag{4.38}$$

where ϵ_i is the emissivity of the i-th element, η_i^c is the cumulative optical efficiency defined as $\eta_i^c \equiv \Pi_{j=1}^i \eta_j$ with j-th element's efficiency η_j, ν is the observation frequency and h is the Planck's constant. It is converged

to temperature unit by scaling from the black body spectrum at fiducial temperature T_0,

$$T_{\rm load} = \frac{T_0}{\displaystyle\int \frac{\eta^c_{\rm sky} h\nu}{\exp\left(h\nu/kT_0\right)-1} d\nu} P_i \equiv \zeta^{-1}_{TP} P_i. \tag{4.39}$$

In POLARBEAR-2, the frequency band width of detectors were measured to be 18.3(22.1) GHz centered at 85.2(143.9) GHz [48]. The cumulative efficiency between the sky and the detectors is $\eta^c_{\rm sky} = 0.24(0.31)$ at W(D) band [34]. We choose $T_0 = 300$ K to obtain the temperature-to-power coefficient $\zeta_{TP} \sim 0.12(0.14)$ pW/K. Then the temperature dependence of loading from cold optical element is

$$\begin{aligned} \frac{dT_{\rm load}}{dT} &= \zeta^{-1}_{TP} \frac{\partial P_i}{\partial T} \\ &= \zeta^{-1}_{TP} \epsilon_i \eta^c_i \int -\frac{h\nu}{T} \frac{\exp\left(h\nu/kT\right) - 1 - \frac{h\nu}{kT}\exp\left(h\nu/kT\right)}{\left(\exp\left(h\nu/kT\right)-1\right)^2}\Bigg|_T d\nu. \end{aligned} \tag{4.40}$$

In the cold optical elements of POLARBEAR-2, temperature of Lyot stop in the 4 K shield heavily contributes to the signal fluctuation because the Lyot stop is made of black body (KEK black) and defines beam edge. It means that the Lyot stop intercepts almost half of the light at W band. Its optical parameters were measured in the lab as $T_{\rm Lyot} = 5.8$ K, $\eta^c_{\rm Lyot} = 0.34(0.51)$ and $\epsilon_{\rm Lyot} = 1.0$ [34]. Numerical integration with these parameters gives us $T_{\rm load} \sim 5.7(6.5)$ K and $B_{\rm Lyot} \equiv dT_{\rm load}/dT_{\rm Lyot} \sim 0.13(0.40)$.

Power drop to the focal plane $B_{\rm drop}$

Temperature fluctuation of the focal plane also changes additive power to TES because dropped power per unit time fluctuates. The temperature derivative of dropped power described in Eq. (4.16) is

$$\frac{dP_{\rm bath}}{dT_{\rm bath}} = -ngT^{n-1}_{\rm bath}, \tag{4.41}$$

where $g \equiv G/(nT^{n-1})$ is a dynamic heat conductance. For TESes used in POLARBEAR-2, n is 4. The maximum of $P_{\rm bath}$, called saturation power, for the POLARBEAR-2 focal plane is experimentally measured as 10.8±1.77(22.9±2.58) pW for 90(150) GHz TESes, respectively [49]. From these results and Eq. (4.16), the thermal conductance G is calculated to be 136.3±22.3(289.0±32.6) pW/K. Then the g is 532±87(1129±127) pW/K^4. Substituting these value into Eq. (4.41), we obtain $\zeta^{-1}_{TP} dP_{\rm bath}/dT_{\rm bath} = -349.0 \pm 57.1(-740.7 \pm 83.3)$.

To estimate the spurious polarization in the pair-difference case later, we determine difference of dynamic thermal conductance between pair detectors as 20% based on the uncertainty of calculated g.

As we can see in these calculation and Eq. (4.17), the power drop from TES to the focal plane is more effective than the change of TES responsivity.

Component	notation	related temperature	value at 90/150 GHz and unit
Responsivity of TES	$A_{\rm resp}$	$T_{\rm bath}$	-0.64/K
Readout gain of mezzanine	$A_{\rm read}$	$T_{\rm read}$	-5×10^{-4}/K
Bias current to TES	$A_{\rm bias}$	$T_{\rm read}$	-5×10^{-4}/K
Intensity of emission from the mirror	$B_{\rm mirror,I}$	$T_{\rm mirror}$	0.0012(0.0016)
Polarization of emission from the mirror	$B_{\rm mirror,P}$	$T_{\rm mirror}$	0.00025(0.00032)
Intensity of reflection of the sky radiation	$B_{\rm refl}$	$T_{\rm sky}$	1.0(1.0)
Polarization of reflection of the sky radiation	$B_{\rm leak}$	$T_{\rm sky}$	-0.00016(-0.00021)
Emission from the Lyot stop	$B_{\rm Lyot}$	$T_{\rm Lyot}$	0.13(0.40)
Power drop from TES to focal plane	$B_{\rm drop}$	$T_{\rm bath}$	-349.0±57.1(-740.7±83.3)
DC polarization from the mirror	$C_{\rm pol}$	$T_{\rm sky},\ T_{\rm mirror}$	43(56) mK

Table 4.1: Temperature coefficients between instrumental temperature and the gain or the incident power. Also the DC polarization is shown here.

4.4 Requirements to temperature fluctuation

Now we have derived temperature coefficients between instrumental temperature and the gain or the incident power for major components. We summarize them in Table 4.1. The parameters we used are summarized in Table 4.2.

We can calculate the ultimate temperature coefficients which appears in the polarization signals in each case of with-HWP and without-HWP by substituting all the derived values into Eqs. (4.8)(4.11)(4.13). Then we derive requirements to the temperature stability or monitoring precision by Eq. (4.1). Since the array sensitivity to polarization is $\sqrt{2}$ times of sensitivity to temperature, we assume the designed sensitivity of POLARBEAR-2 is NEPol $\simeq 5\ \mu{\rm K}\sqrt{\rm s}$. All requirements are derived as a noise spectrum density and are imposed at 50 mHz frequency.

4.4.1 With HWP

With HWP and without gain reconstruction, we derive requirements by Eq. (4.8) as

$$\begin{aligned}{\rm NSD}\left[{\rm T_{bath}}\right] &< \frac{\rm NEPol}{\left|\left(A_{\rm resp}+g_1B_{\rm drop}\right)C_{\rm pol}-\dfrac{B_{\rm leak}+g_1C_{\rm pol}\left(B_{\rm refl}+B_{\rm leak}\right)}{\left(1+g_1C_{\rm pol}\right)B_{\rm refl}}B_{\rm drop}\right|}\\ &\simeq \frac{5\ \mu{\rm K}\sqrt{\rm s}}{|-8.3(-19.2)\times10^{-2}|}\simeq 60(26)\ \mu{\rm K}\sqrt{\rm s},\end{aligned} \tag{4.42}$$

$$\begin{aligned}{\rm NSD}\left[{\rm T_{Lyot}}\right] &< \frac{\rm NEPol}{\left|g_1B_{\rm Lyot}C_{\rm pol}-\dfrac{B_{\rm leak}+g_1C_{\rm pol}\left(B_{\rm refl}+B_{\rm leak}\right)}{\left(1+g_1C_{\rm pol}\right)B_{\rm refl}}B_{\rm Lyot}\right|}\\ &\simeq \frac{5\ \mu{\rm K}\sqrt{\rm s}}{|2.1(8.4)\times10^{-5}|}\simeq 240(60)\ {\rm mK}\sqrt{\rm s},\end{aligned} \tag{4.43}$$

Physical quantity	notation	value at 90(150) GHz and unit
Mirror temperature	$T_{\rm mirror}$	273 K
Sky temperature	$T_{\rm sky}$	10 K
Incident angle on the primary mirror	θ	32.5° [39]
Aluminum resistivity	ρ	$2.4 \times 10^{-8}\ \Omega \cdot$ m at 273 K [47]
Temperature dependence of Al resistivity	$d(\ln \rho)/dT$	4×10^{-3} K^{-1} at 273 K
Saturation power of TES	$P_{\rm sat}$	10.8±1.77(22.9±2.58) pW/K^4 [49]
Variation of dynamic thermal conductance	$\delta_{\rm cond}$	20% [49]
Thermal conduction index of TES	n	4 [32]
Temperature sensitivity of TES	α	200
Bias voltage for TES	$V_{\rm elec}$	2.3 μV
Loop gain of TES	$\mathcal{L}$	15
Transition temperature of TES	T_c	400 mK
Bath temperature of TES	T_b	270 mK
First-order non-linearity of TES	g_1	-1% K^{-1} [39]
Lyot stop temperature	$T_{\rm Lyot}$	5.8 K [34]
Cumulative efficiency from Lyot stop	$\eta^c_{\rm Lyot}$	0.34(0.51) [34]
Cumulative efficiency from the sky	$\eta^c_{\rm sky}$	0.24(0.31) [34]
Emissivity of Lyot stop	$\epsilon_{\rm Lyot}$	1.0 [34]
Bias power in temperature unit	$I_{\rm bias}/g_0$	20 K
Variation of bias power	$\delta_{\rm bias}/g_0$	1 K
Uncertainty of relative gain	$\delta g_{\rm pair}$	0.5% [8]
Center of observation frequency	ν	85.2±18.3(143.9±22.1) GHz [48]
Detector array sensitivity	$\mathrm{NET}_{\rm array}$	3.4 $\mu\mathrm{K}\sqrt{\mathrm{s}}$ [14]

Table 4.2: Parameters used to calculate the temperature coefficients.

$$\begin{aligned}
\mathrm{NSD}\left[\mathrm{T_{read}}\right] &< \frac{\mathrm{NEPol}}{\left| A_{\rm read} C_{\rm pol} - \frac{B_{\rm leak} + g_1 C_{\rm pol}\left(B_{\rm refl} + B_{\rm leak}\right)}{\left(1 + g_1 C_{\rm pol}\right) B_{\rm refl}} A_{\rm bias} \frac{I_{\rm bias}}{g_0} \right|} \\
&\simeq \frac{5\ \mu\mathrm{K}\sqrt{\mathrm{s}}}{|-2.7(-3.6) \times 10^{-5}|} \simeq 186(139)\ \mathrm{mK}\sqrt{\mathrm{s}},
\end{aligned} \tag{4.44}$$

$$\begin{aligned}
\mathrm{NSD}\left[\mathrm{T_{mirror}}\right] &< \frac{\mathrm{NEPol}}{\left| B_{\rm mirror,P} + g_1 C_{\rm pol}\left(B_{\rm mirror,I} + B_{\rm mirror,P}\right) - \frac{B_{\rm leak} + g_1 C_{\rm pol}\left(B_{\rm refl} + B_{\rm leak}\right)}{\left(1 + g_1 C_{\rm pol}\right) B_{\rm refl}} B_{\rm mirror,I} \right|} \\
&\simeq \frac{5\ \mu\mathrm{K}\sqrt{\mathrm{s}}}{|2.5(3.2) \times 10^{-4}|} \simeq 20(16)\ \mathrm{mK}\sqrt{\mathrm{s}}.
\end{aligned} \tag{4.45}$$

With gain construction, we use Eq. (4.11) to derive

$$\begin{aligned}
\mathrm{NSD}\left[\mathrm{T_{bath}}\right] &< \frac{\mathrm{NEPol}}{\left| -2 g_1 C_{\rm pol}^2 \left(A_{\rm resp} - g_1 B_{\rm drop} \frac{B_{\rm leak}}{B_{\rm refl}} \right) - B_{\rm leak}\left(1 - g_1 C_{\rm pol}\right) \frac{B_{\rm drop}}{B_{\rm refl}} \right|} \\
&\simeq \frac{5\ \mu\mathrm{K}\sqrt{\mathrm{s}}}{|-5.6(-15.6) \times 10^{-2}|} \simeq 90(32)\ \mu\mathrm{K}\sqrt{\mathrm{s}},
\end{aligned} \tag{4.46}$$

$$\begin{aligned}
\mathrm{NSD}\left[\mathrm{T_{Lyot}}\right] &< \frac{\mathrm{NEPol}}{\left| 2 g_1^2 C_{\rm pol}^2 B_{\rm Lyot} \frac{B_{\rm leak}}{B_{\rm refl}} - B_{\rm leak}\left(1 - g_1 C_{\rm pol}\right) \frac{B_{\rm Lyot}}{B_{\rm refl}} \right|} \\
&\simeq \frac{5\ \mu\mathrm{K}\sqrt{\mathrm{s}}}{|2.1(8.4) \times 10^{-5}|} \simeq 240(60)\ \mathrm{mK}\sqrt{\mathrm{s}},
\end{aligned} \tag{4.47}$$

$$\begin{aligned}\mathrm{NSD}\left[\mathrm{T_{read}}\right] &< \frac{\mathrm{NEPol}}{\left|-2g_1C_{\mathrm{pol}}^2\left\{A_{\mathrm{read}} - g_1\left(B_{\mathrm{leak}}+B_{\mathrm{refl}}\right)\frac{A_{\mathrm{bias}}}{B_{\mathrm{refl}}}\frac{I_{\mathrm{bias}}}{g_0}\frac{1}{1+g_1C_{\mathrm{pol}}}\right\} - B_{\mathrm{leak}}\frac{1-g_1C_{\mathrm{pol}}}{1+g_1C_{\mathrm{pol}}}\frac{A_{\mathrm{bias}}}{B_{\mathrm{refl}}}\frac{I_{\mathrm{bias}}}{g_0}\right|} \\ &\simeq \frac{5\ \mu\mathrm{K}\sqrt{\mathrm{s}}}{|-1.6(-2.1)\times 10^{-6}|} \simeq 3.2(2.4)\ \mathrm{K}\sqrt{\mathrm{s}},\end{aligned} \tag{4.48}$$

$$\begin{aligned}\mathrm{NSD}\left[\mathrm{T_{mirror}}\right] &< \frac{\mathrm{NEPol}}{\left|B_{\mathrm{mirror,P}}\left(1-g_1C_{\mathrm{pol}}\right) - 2g_1^2C_{\mathrm{pol}}^2\left(B_{\mathrm{mirror,P}} - \frac{B_{\mathrm{leak}}}{B_{\mathrm{refl}}}B_{\mathrm{mirror,I}}\right) - B_{\mathrm{leak}}\left(1-g_1C_{\mathrm{pol}}\right)\frac{B_{\mathrm{mirror,I}}}{B_{\mathrm{refl}}}\right|} \\ &\simeq \frac{5\ \mathrm{mK}\sqrt{\mathrm{s}}}{|2.5(3.2)\times 10^{-4}|} \simeq 20(16)\ \mathrm{mK}\sqrt{\mathrm{s}}.\end{aligned} \tag{4.49}$$

$$\mathrm{NSD}\left[\mathrm{g_{meas}}\right] < \frac{\mathrm{NEPol}}{\left(1+g_1C_{\mathrm{pol}}\right)C_{\mathrm{pol}}} \simeq 116(89)\mathrm{ppm}\sqrt{\mathrm{s}}. \tag{4.50}$$

The precision of gain calibration is actually limited by the intensity stability of the stimulator, so that the requirements above are very ideal.

4.4.2 Without HWP

When we do not use a HWP and obtain polarized signal by taking difference of orthogonal detectors in the same pixel, the requirements are derived by Eq. (4.13) as

$$\mathrm{NSD}\left[\mathrm{T_{bath}}\right] < \frac{\mathrm{NEPol}}{\left|\left(\delta_{\mathrm{cond}}+\delta_{\mathrm{pair}}\right)B_{\mathrm{drop}}\right|} \simeq \frac{5\ \mu\mathrm{K}\sqrt{\mathrm{s}}}{|-71.5(-151.8)|} \simeq 0.07(0.03)\ \mu\mathrm{K}\sqrt{\mathrm{s}}, \tag{4.51}$$

$$\mathrm{NSD}\left[\mathrm{T_{Lyot}}\right] < \frac{\mathrm{NEPol}}{\left|\delta_{\mathrm{pair}}B_{\mathrm{Lyot}}\right|} \simeq \frac{5\ \mu\mathrm{K}\sqrt{\mathrm{s}}}{|6.5(20)\times 10^{-4}|} \simeq 7.7(2.5)\ \mathrm{mK}\sqrt{\mathrm{s}}, \tag{4.52}$$

$$\mathrm{NSD}\left[\mathrm{T_{read}}\right] < \frac{\mathrm{NEPol}}{\left|A_{\mathrm{read}}\delta_{\mathrm{bias}}\right|} \simeq \frac{5\ \mu\mathrm{K}\sqrt{\mathrm{s}}}{|-0.5(-0.5)\times 10^{-4}|} \simeq 0.1(0.1)\ \mathrm{K}\sqrt{\mathrm{s}}, \tag{4.53}$$

$$\mathrm{NSD}\left[\mathrm{T_{mirror}}\right] < \frac{\mathrm{NEPol}}{\left|B_{\mathrm{mirror,P}}+\delta_{\mathrm{pair}}B_{\mathrm{mirror,I}}\right|} \simeq \frac{5\ \mathrm{mK}\sqrt{\mathrm{s}}}{|2.6(3.3)\times 10^{-4}|} \simeq 20(15)\ \mathrm{mK}\sqrt{\mathrm{s}}. \tag{4.54}$$

4.5 Summary of temperature requirement

We described the signal models for wth- and without- HWP in Sec. 4.2. Then we calculated the dependence of the signal on each instrument in Sec. 4.3 and finally obtained requirements to temperature stability or monitoring precision in Sec. 4.4. The parameters we assumed are listed in Table 4.2. The "raw" temperature coefficients in the gain and input, which intended to distinguish multiple effects from an instrument, are shown in Table 4.1. The "ultimate" temperature coefficients which appear in the detector signals are summarized in Table 4.3 and Table 4.4.

	With HWP 90(150) GHz	
Component	without gain cal.	with gain cal.
focal plane	$-8.3(-19.2) \times 10^{-2}$	$-5.6(-15.6) \times 10^{-2}$
Lyot stop	$+2.1(+8.4) \times 10^{-5}$	$+2.1(+8.4) \times 10^{-5}$
readout	$-2.7(-3.6) \times 10^{-5}$	$-1.6(-2.1) \times 10^{-6}$
primary mirror	$+2.5(+3.2) \times 10^{-4}$	$+2.5(+3.2) \times 10^{-4}$

Table 4.3: Instrumental temperature dependence of the polarization signal of detector with HWP. Dimensionless coefficients between signal after PCA reduction in the Kelvin unit and instrumental temperature are shown.

	Without HWP 90(150) GHz	
Component	without gain cal.	with gain cal.
focal plane	$-71.5(-151.8)$	$-71.5(-151.8)$
Lyot stop	$+6.5(+20) \times 10^{-4}$	$+6.5(+20) \times 10^{-4}$
readout	$-0.5(-0.5) \times 10^{-4}$	$-0.5(-0.5) \times 10^{-4}$
primary mirror	$+2.6(+3.3) \times 10^{-4}$	$+2.6(+3.3) \times 10^{-4}$

Table 4.4: Instrumental temperature dependence of the polarization signal of detector without HWP. Dimensionless coefficients between signal in the Kelvin unit and instrumental temperature are shown.

The requirements calculated in half-wave plate case and pair-difference case are compared in Table 4.5 and Table 4.6. While the requirement for mirror only change by factor smaller than one, those of other elements are significantly loosened by a HWP. A polarization modulation by HWP reduces optical leakage of the sky radiation and mitigates instrumental spurious polarization caused by the uncertainty of relative gain. We see that the contribution of bias power amplified by the readout temperature is mitigated by PCA.

Temperature fluctuation of the Lyot stop and focal plane has been measured in the lab to be 5 mK$\sqrt{\text{s}}$ and 9 μK$\sqrt{\text{s}}$, respectively. Both of them satisfied the requirements for with-HWP case. As for warm components, the calculated requirements show us that we need temperature monitor with precision better than 15 mK$\sqrt{s}$ at 50 mHz for inflation study.

	With HWP 90(150) GHz	
Component	without gain cal.	with gain cal.
focal plane NET_{bath}	60(26) $\mu K\sqrt{s}$	90(32) $\mu K\sqrt{s}$
Lyot stop NET_{Lyot}	240(60) $K\sqrt{s}$	240(60) $K\sqrt{s}$
readout NET_{elec}	0.19(0.14) $K\sqrt{s}$	3.2(2.4) $K\sqrt{s}$
primary mirror NET_{mirror}	20(16) $mK\sqrt{s}$	20(16) $mK\sqrt{s}$

Table 4.5: Requirements to either NSD of temperature instability or NSD of measurement noise when a HWP is used. Requires the signal fluctuation not to exceed the array sensitivity at the time scale of interest.

	Without HWP 90(150) GHz	
Component	without gain cal.	with gain cal.
focal plane NET_{bath}	0.07(0.03) $\mu K\sqrt{s}$	0.07(0.03) $\mu K\sqrt{s}$
Lyot stop NET_{Lyot}	7.7(2.5) $mK\sqrt{s}$	7.7(2.5) $mK\sqrt{s}$
readout NET_{elec}	0.1(0.1) $K\sqrt{s}$	0.1(0.1) $K\sqrt{s}$
primary mirror NET_{mirror}	20(15) $mK\sqrt{s}$	20(15) $mK\sqrt{s}$

Table 4.6: Requirements to either NSD of temperature instability or NSD of measurement noise when a HWP is not used. Requires the signal fluctuation not to exceed the array sensitivity at the time scale of interest.

5

Temperature monitoring of the warm components

5.1 Design concept of warm temperature monitor

The temperature monitor for 300 K components consist of thermometers, a scanner, a measuring instrument and a control computer. The schematic view is shown in Fig. 5.1.

A warm temperature monitor is required to measure the 300 K temperature with an order of 10 mK$\sqrt{\text{s}}$ precision. Since we concern rather the relative fluctuation than the absolute temperature value, the hardware design is mainly constrained by thermometer sensitivity and measurement noise. The resolution of the monitoring device has to be sufficiently high to detect a thermometer response against $O(10)$ μK fluctuation. Moreover, the measurement noise must not exceed the sensor response.

In addition, the sampling rate is constrained by the angular scale which we aim to observe and the scan strategy of the experiment. As described in Sec. 4.1, it is necessary for the inflation study to investigate the large angular B-mode power spectrum down to $\ell \sim 50$ (3.6°) scale. The azimuthal scan speed of POLARBEAR was $0.4^\circ/s$ so that it takes 10 seconds to scan this angular scale [38]. In order to let this scale be below the Nyquist frequency, the sampling rate of temperature monitors should be larger than 0.2 Hz.

A large mirror or a large amount of readout electronics require to sense multiple thermometers simultaneously. In this case, a combination of small-scale, low-price thermometers and a fast-sampling multiplexer is suitable.

We designed two types of warm temperature monitoring system because the one used for readout electronics needs a special consideration for electromagnetic compatibility. It is shielded by a Faraday cage not to induce excess noise to the readout through its emission.

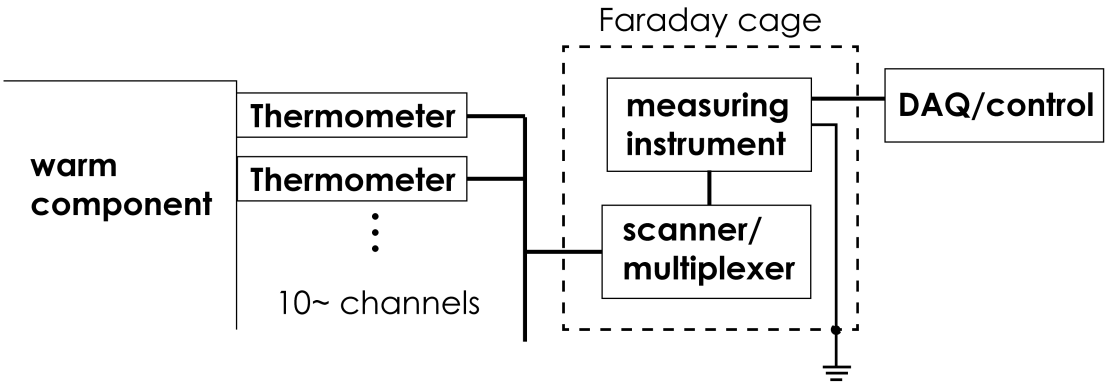

Figure 5.1: A schematic view of the temperature monitoring system for reflectors.

5.2 Measurement device

5.2.1 Device selection

We chose two instruments to readout thermometers; a LTC2983 temperature measurement system provided by Analog Devices Inc and a 34980A multifunction switching and measurement unit provided by Keysight Technologies Inc. Their images are shown in Fig. 5.2. The former was prepared for reflectors and the latter was for readout electronics.

The 34980A can multiplex up to 40 channels of two-wire system connected via an optional 34925A FET multiplexer and a 34925T terminal block [50]. The sampling rate was 0.2 Hz when we read 40 channels. It has unlimited relay lifetime so that it is appropriate to be used for years-long observation. Its nominal measurement uncertainty is $\pm 0.0020\%$ (reading, *stat*) 0.0005% (range, *sys*) in a sequential measurement within 24 hours. Assuming that we read a 3 kΩ resistor with 10 kΩ resistance range, the uncertainty becomes $\pm 0.06(stat) \pm 0.05(sys)\Omega$.

The LTC2983 is a relatively small measurement board so that it can be stored in a metal box to shield its electromagnetic emission. It can multiplex up to 10 channels with an optional DC2210 terminal board and can be controlled by a Linduino One single-board computer [51]. We controlled whole of them with Raspberry Pi 3B+ single-board computer provided by Raspberry Pi Foundation. The sampling rate is 0.7 Hz. We can estimate its measurement uncertainty by that of voltage measurement. The uncertainty of voltage is $\sim 1\ \mu V_{\rm rms}$ nominally. When 100 μA current is applied, the uncertainty of resistance is 0.01 Ω.

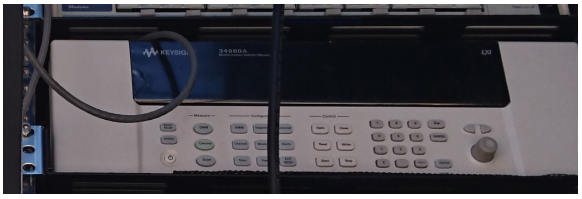

(a)

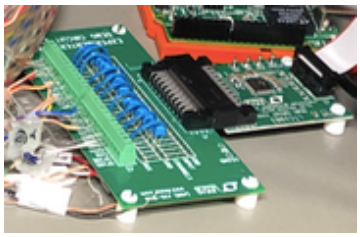

(b)

Figure 5.2: Images of temperature measuring instruments. (a) 34980A. (b) LTC2983.

5.2.2 Setup of internal noise measurement

We evaluated the measurement noise of the two instruments using a reference resistor. We used a PTF563K0000BYEK metal film resistor provided by Vishay Intertechnology Inc, whose the resistance at 298 K was 3 kΩ, as a reference. Since the resistance of the circuits inside the instruments could fluctuate with temperature, we shorted a channel per an instrument to measure internal resistances. We measured their resistance for an hour with each instrument, subtracted the internal resistance from the reference, then calculated noise spectrum density (NSD) for every 1000 seconds cuts of time-ordered data and averaged them. In the resistance measurement, the excitation current was set on 100 μA for both instruments. The NSDs are shown in Fig. 5.3. Finally we read the NSD value at 50 mHz as a conservatively lower frequency than required sampling rate.

5.2.3 Result of internal noise

The measurement noise at 50mHz was 0.06 $\Omega\sqrt{s}$ for the combination of 34980A plus 34925A, and 0.04 $\Omega\sqrt{s}$ for LTC2983. Conversion from the resistance unit to temperature depends on sensitivity of thermometer. For a 3 kΩ NTC thermistor with the temperature coefficient -150 Ω/K, they are 0.4 mK$\sqrt{s}$ and 0.26 mK$\sqrt{s}$. These are consistent with nominal uncertainty, and sufficiently low to monitor warm components.

5.3 Thermometer selection

5.3.1 thermometer types

We compared sensitivies of four types of thermometers; thermistor, platinum resistance temperature detector (RTD), thermocouple and 1-wire temperature sensor. All of them have linear responsivity at the room temperature.

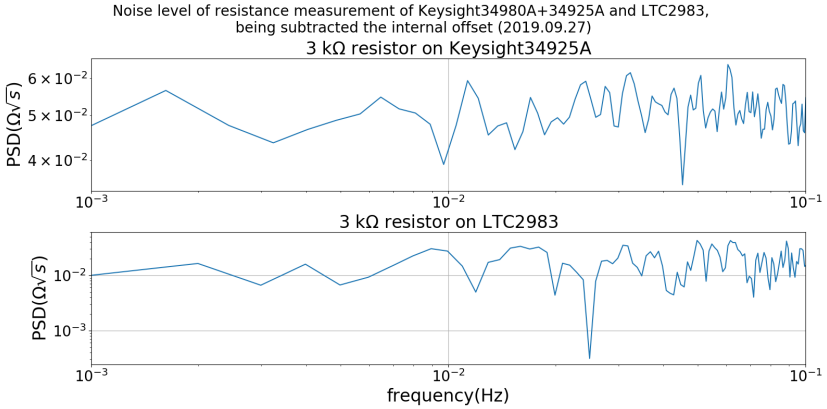

Figure 5.3: Measurement noise of resistance with two instruments; 34980+34925A and LTC2983+DC2210.

The temperature coefficient, which is a ratio between change of sensor's observable and temperature fluctuation, of each thermometer determines the measurement precision. The larger the temperature coefficient is, the smaller the effect of internal measurement noise of the measuring instruments be.

Thermistor is a resistor made from metal. We tested a PS302J2 thermistor provided by Littelfuse Inc, whose the resistance value was 3 kΩ at 298 K [52]. Its width is 2.4 mm and the cost was 3 USD per a sensor. Thermistor's response is expressed as a B-coefficient. It is determined by $B = \ln(R/R_0)/(T^{-1} - T_0^{-1})$, using two temperatures T, T_0 and corresponding resistances R, R_0. For our thermistor, B= 3892 K where $T = 323$ K and $T_0 = 273$ K. It leads a temperature coefficient ~ -150 Ω/K at 273 K.

Platinum RTD changes its resistance with temperature as well as a thermistor. We tested a NB-PTCO-011 platinum metal film sensor provided by TE Connectivity Inc, whose the resistance was 100 Ω at 273 K [53]. Its dimension is 2 mm width, 2.3 mm depth and 1.1 mm height. Its cost was 4 USD per a sensor. The temperature coefficient was 3850ppm/K in the range of 273∼373 K, corresponding to 0.385 Ω/K at 273 K.

Thermocouple is a temperature sensor taking advantage of the Seebeck effect caused at a junction of two different metals. We tested a T-type (copper-constantan) thermocouple 621-2209 provided by RS Components Inc [54]. The probe diameter was 0.3 mm. Its cost was 10 USD per a sensor. The temperature coefficient was 42 μV/K at 273 K.

1-wire temperature sensor is a device which transfer digitized temperature data to the computer through only one lead in addition to a ground line. We tested DS18B20 thermal probe sensor with water-resistant stainless sheath, provided by Maxim Integrated Inc [55]. It measures temperature by taking difference of voltages across two semiconductors with different tem-

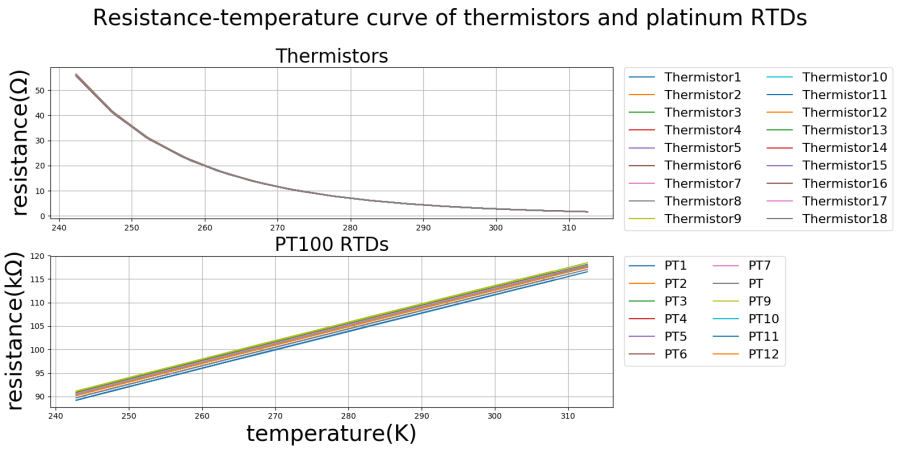

Figure 5.4: Resistance-temperature curve of (*top*) thermistors and (*bottom*) platinum RTDs.

perature coefficients, and immediately digitize it at an ADC. Its precision is 0.5 K in according to the data sheet, so it is apparently inappropriate for the sensitivity we require. We show it just as a reference since it was already used by POLARBEAR to monitor the telescope's thermal deformation.

It is easy to be readout and does not require any external conversion curve. Its dimension was 50 mm depth and 6 mm height. Its cost was 2 USD per a sensor.

5.3.2 Setup of thermometer noise measurement

First we calibrated the resistance-temperature relationship of the thermistor and the platinum RTD using Keysight34980+34925A devices. As for the thermocouple, the voltage was translated with a standard curve installed in the measuring instrument. We calibrated its thermoelectromotive force with cold junction compensation, using ice water. The resistance-temperature curves of the thermistor and the platinum RTD is shown in Fig. 5.4. We measured the resistance of thermometers at every 5 °C in the range from -30 °C to 30 °C in a thermal chamber. As a reference thermometer, we used a calibrated PT103-14L-P40816, a platinum RTD provided by Lakeshore Inc.

Then we measured the temperature noise of each thermometer. We connected the thermistor, platinum RTD, thermocouple to the LTC2983. Only the 1-wire temperature sensor was read by a Raspberry Pi 3B+. We located these sensors in the room atmosphere and measured their temperature for an hour. After this measurement we calculated NSD for every 1000 seconds cut from the time-ordered data and averagaed them. The NSDs that

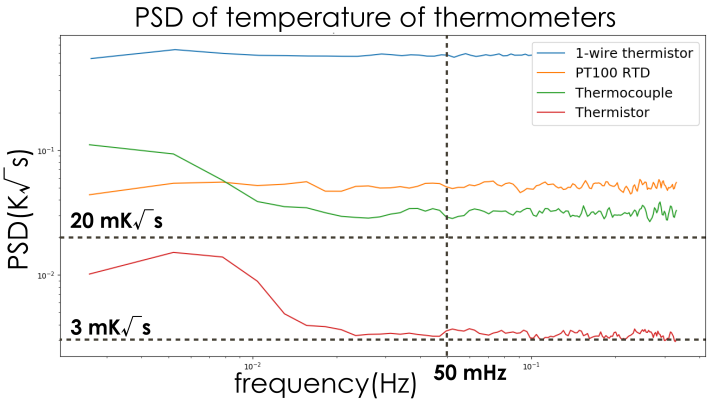

Figure 5.5: Temperature measurement noise of thermistor, platinum RTD, T-type thermocouple and 1-wire temperature sensor.

Thermometer	sensitivity (at 273 K)	price (USD)	noise with LTC2983 (mK$\sqrt{s}$ at 50mHz)
Thermistor PS302J2	150 Ω/K	3	3.4
Platinum RTD NB-PTCO-011	0.385 Ω/K	4	46.8
Thermocouple 621-2209	42 μV/K	10	25.5
1-wire temperature sensor DS18B20	-	2	89.7

Table 5.1: Properties of four thermometers.

we obtained were summations of temperature instability and measurement noise.

5.3.3 Result of thermometer noise measurement

The temperature measurement noise of the four types of thermometer is shown in Fig. 5.5). The fluctuations of thermistor, platinum RTD, thermocouple and 1-wire sensor at 50 mHz was 3.4 mK$\sqrt{s}$, 46.8 mK$\sqrt{s}$, 25.5 mK$\sqrt{s}$, 89.7 mK$\sqrt{s}$, respectively. Properties of these thermometers are shown in Table. 5.1.

This result shows that the thermistor has the lowest noise. It is sufficient to monitor readout electronics. The reflector requires furthermore lower noise but it can be achieved by attaching to the metal material and applying the wind protection. We adopted the combination of 34980A plus 34925A as temperature measurement devices for reflectors. For readout electronics, we adopted LTC2983. Thermistor was chosen as a thermometer for both targets.

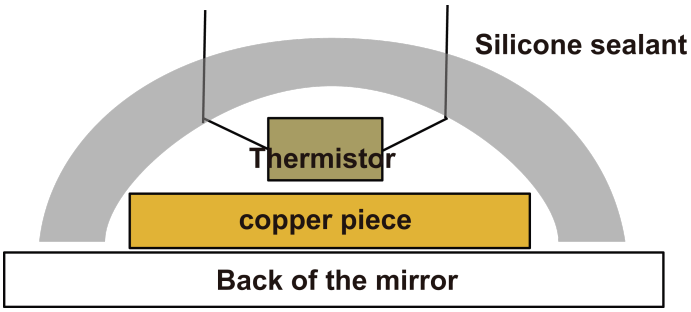

Figure 5.6: The scheme of thermistor covered with silicone wind protection and attached on the reflector.

5.4 Installation to the site

We installed the temperature measurement devices and calibrated thermistors to the observational site of POLARBEAR-2. At the mountainside site, wind and sunlight is hard. These two spatially non-uniform factors are serious source of systematic error because we need to estimate temperature of the front of the mirror from the its back. Before attaching thermometers to the telescope system, we applied windproof and sun shading to the sensors in order to mitigate excess temperature fluctuation.

5.4.1 Windproof

Setup of windproof

In order to cut down the temperature fluctuation caused by hard wind of the site, we applied wind proof to the thermistors. We bonded a thermistor to a small and thin copper piece (W 10 mm $\times$ D 10 mm $\times$ 1 mm) with varnish and covered it with silicone sealant. The schematic view is shown in Fig. 5.6. It also reduces the temperature fluctuation caused by the wind.

Result of windproof

We measured the thermal noise of this covered thermistor with the 34980A digital multimeter at KEK laboratory. The group of thermistors were located in a thermal chamber where hot wind circulates to control temperature. Half of the thermistors were covered with silicone and the other half was not. All of them were contacting with the metal floor of the thermal chamber through the copper piece. We calculated NSDs from 1000 seconds cuts of time-orderd data.

We obtained temperature fluctuation as 2.5$\pm$0.4 mK$\sqrt{s}$ at 50 mHz for without-sealant group and 0.8$\pm$0.2 mK$\sqrt{s}$ for with-sealant group. The NSDs

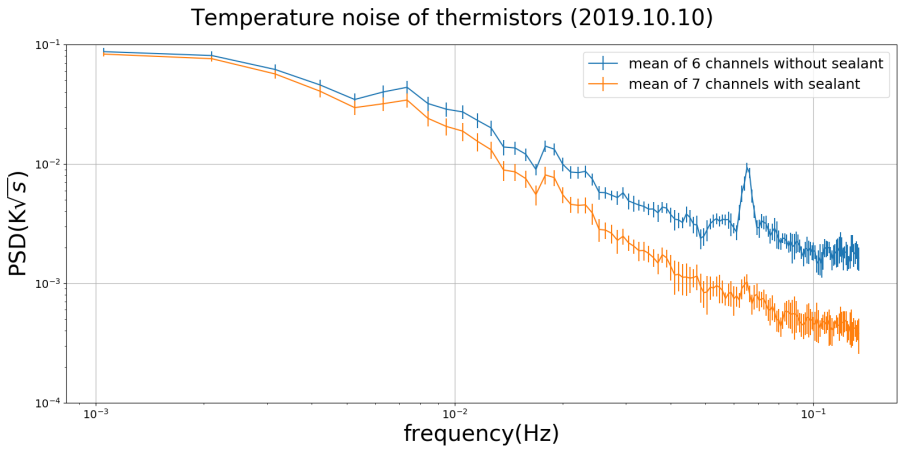

Figure 5.7: The thermal noise of thermistors with- and without- silicone wind protection, measured with 34980A+34925A.

are shown in Fig. 5.7. Without active control by the wind, the noise of with-sealant group was further reduced to 0.6±0.2 mK$\sqrt{s}$. It satisfies the requirement to the temperature monitor for mirror. We also adopted this wind protection to the temperature monitor for electronics.

5.4.2 Sun shading

Setup of sun shading

As well as wind, the sunlight is hard at the site because of its high altitude. The direct sunlight may raise temperature of a thermometer and make displacement of measured temperature from the true temperature of the target instrument. The thermometers for the mirrors, which are exposed to the ambient air, needs this care. We covered the thermistors with aluminum foil to reflect sunlight (Fig. 5.8). Thermistors for readout electronics does not need this application because they are settled in closed saddlebags.

Result of sun shading

We measured temperature of back and front of the mirrors with covered and uncovered thermistors at the site. In each condition, we attached thermistors on the bottom edge and slightly lower from the center. Then we checked the measured temperature difference between back and front.

We found large temperature difference during the daytime without sun shading. The temperature difference was $\sim$ 8 K at most for the primary mirror and $\sim$ 4 K for the secondary mirror (Fig. 5.9). After applying sun shading, it reduced to $\sim$ 1 K (Fig. 5.10).

Figure 5.8: Photo of a sun-shaded thermistor attached on the bottom of back of the primary mirror. An onewire sensor is at the left of the thermistor for cross check of absolute temperature.

We plan to attach white back panels on the POLARBEAR-2 telescope before the science observation starts. After they are installed, we will no longer need the aluminium foils for back of the primary mirror. However, this brief sun shade can be still useful to attach thermometers on other ambient parts of the telescope.

5.4.3 Emission shielding for readout electronics

The system for readout electronics needs special care to shield its electromagnetic emission. We located the measuring system include LTC2983 in an aluminum box. Its schematic view and the photograph are shown in Fig. 5.11. A Raspberry Pi 3B+ controls two LTC2983 systems. A Linduino One communicates to a LTC2983 and a DC2210 multiplex to the thermistors outside. The box chassis is grounded through power ground.

5.4.4 Thermometer location

We attached 12 thermistors on each of two mirrors, and 2 thermistors on each of two saddlebags. The sensor locations on the mirrors and electronics crates are drawn in Fig. 5.12.

Eight sensors surround each mirror on the edge of reflection region and four gathers at the center. All sensors for the mirrors are attached on its back with silicone sealant. They are connected to Keysight 34980A+34925A measurement devices by insulated copper leads.

We did not attach sensors directly on the mezzanine boards not to cause short. Instead, we screwed copper chips on which thermistors are glued to

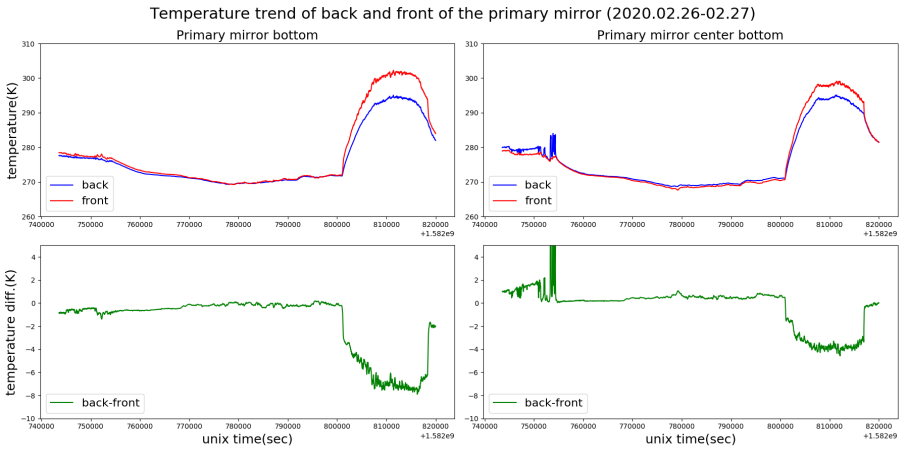

Figure 5.9: Temperature trends of the primary mirror for 24 hours without sun shading. (*top left*) Temperature at the bottom. *blue line:* Back of the mirror. *red line:* Front of the mirror. (*top right*) Temperature at the center bottom. *blue line:* Back of the mirror. *red line:* Front of the mirror. (*bottom left*) Temperature difference between back and front at the bottom. (*bottom right*) Temperature difference between back and front at the center bottom.

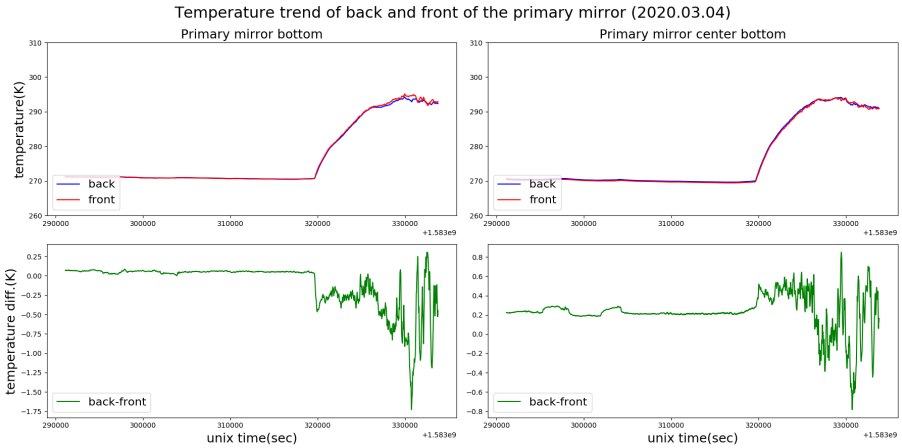

Figure 5.10: Temperature trends of the primary mirror for 24 hours with sun shading. The left column is for bottom of the primary mirror and right for the center bottom. (*top*) Temperature TODs. *blue line:* Back of the mirror. *red line:* Front of the mirror. (*middle*) Temperature difference between back and front of the mirror. (*bottom*) Difference between fluctuations from respective mean value of the board and the wall.

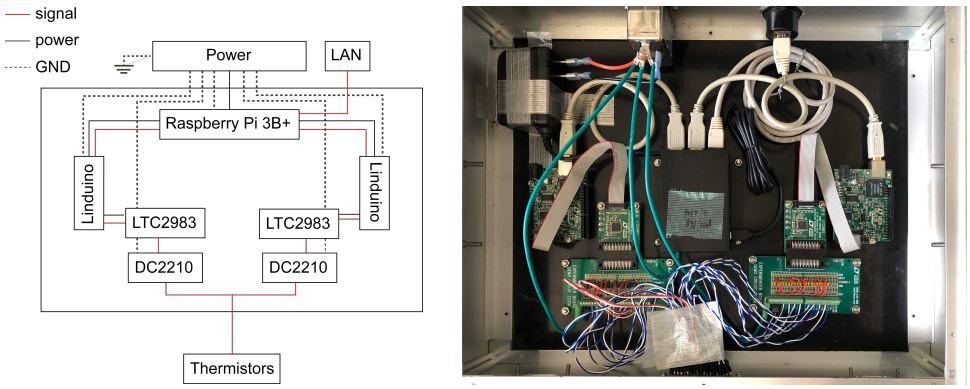

(a) (b)

Figure 5.11: The temperature monitoring system for readout electronics. (a) schematic view. (b) photograph. The measuring system is located in a metal box for RF shielding.

the metal chassis of the crate. We have additional temperature sensors built in each readout board. They monitor temperature of mezzanine, SQCB and FPGA on an IceBoard with resolution of 0.25 K.

5.5 Monitoring temperature fluctuation at the site

5.5.1 Temperature fluctuation of reflectors

We combined our temperature monitoring system to the "slowdaq" housekeeping DAQ and started to monitor the warm instruments. The TODs of 12 thermistors attached on the primary mirror for 24 hours are shown altogether in Fig. 5.13. Their NSDs at night are in Fig. 5.14. The noise at 50 mHz is below 1 mK$\sqrt{s}$ over all channels, which is lower than the requirement. The noise in the daytime at 50 mHz is 7 mK$\sqrt{s}$ at most (Fig. 5.15), which corresponds to 1.6(2.3) μK$\sqrt{s}$ as the polarization signal at 90(150) GHz. During the sunrise, this noise can become larger.

5.5.2 Temperature fluctuation of readout electronics

We started to monitor temperature of the crate in which IceBoards and mezzanine boards are installed. Two LTC2983 measurement devices and a Raspberry Pi were packaged in a metal box, and one box were installed in each MUX saddlebag.

The temperature TODs of 4 thermistors distributed into two saddlebags are shown altogether in Fig. 5.16. It was during an azimuthal scan at a constant elevation, and the bolometer readout was working. The temper-

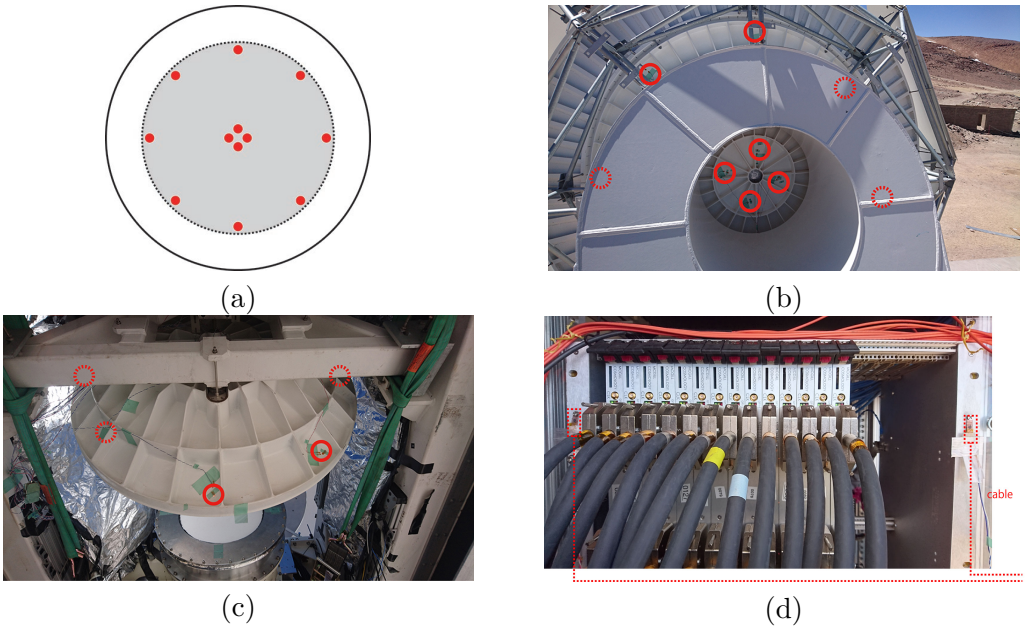

Figure 5.12: The locations of thermistors on the warm instruments. (a) Drawing of distribution of the thermistors on each mirror. Red circles represent thermistors. (b) Back of the primary mirror. (c) Back of the secondary mirror. (d) A crate of the readout electronics.

ature NSDs are shown in Fig. 5.17. The noise at 50 mHz is around 10 mK$\sqrt{s}$ over all channels, which is comparable with the requirement for case without HWP. Only in the MUX2 saddlebag, a cooling fan for temperature regulation was spinning at the bottom of the saddlebag. It prevents the IceBoard from thermal runaway but degrades the temperature stability. The harmonic peaks at high frequency of the NSD of MUX2 right edge are due to vibration of the thermometry cables.

5.6 Systematic errors of temperature measurement

In this section, we discuss the uncertainty of temperature measurement. Statistical uncertainty on each datapoint is determined by the measurement noise of devices. Systematic uncertainty rises from calibration error of thermistors, resistance of lead wires between a device and sensors, self heating of thermistors, distance from sensors and target instruments.

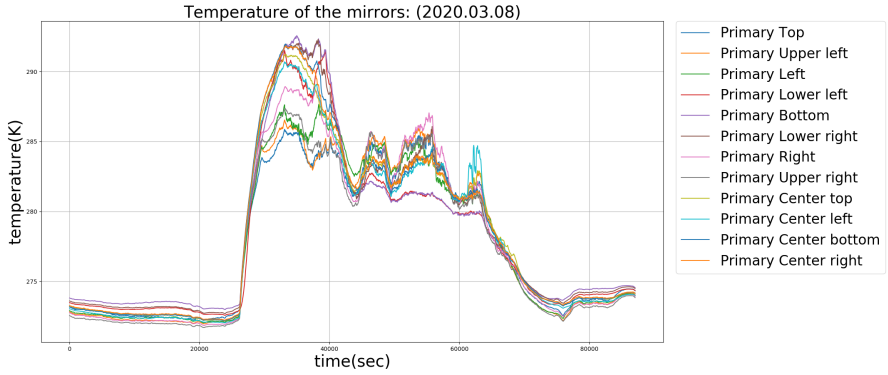

Figure 5.13: Temperature TOD of the primary mirror. 12 channels are named after the location seen from the front.

Uncertainty due to thermometer calibration and the measurement devices

As we mentioned in Sec. 5.2, we can calculate nominal error of Keysight 34980A and LTC2983. A Keysight 34980A has uncertainty of ±0.0020%(reading) ±0.0005%(range) on resistance measurement in 24 hours as we estimated in Sec. 5.2. Resistance of our thermistors are $3{\times}10^3 \sim 2 \times 10^4$ Ω at 262∼302 K. This temperature range is the typical ambient temperature at the site. Fixing the resistance range to 10 kΩ and regarding, the uncertainty is $\pm 0.06 \sim 0.4(stat) \pm 0.05(sys)$ Ω for 302∼262 K. The uncertainty of a shorted channel is added to this because we subtract the internal resistance of the device to compensate the temperature dependence of the device. The internal resistance is 6×10^2 Ω and its uncertainty is $\pm 0.012(stat) \pm 0.05(sys)$ Ω. The total uncertainty is $\pm 0.06 \sim 0.4(stat) \pm 0.07(sys)$ Ω. On the other hand, a LTC2983 for readout temperature has ±0.01 Ω uncertainty.

Temperature difference has $\sqrt{2}$ times of these uncertainties because it uses two datapoints.

Thermometer calibration and measurement noise

The calibration error of thermistors originated to both of the temperature and resistance. The Lakeshore PT103-14L-P40816 platinum RTD, which was used as a reference thermometer, was calibrated in a temperature range from 12 k to 330 K. Its calibration data can be downloaded from the website of Lakeshore [56]. From 100 K to 310 K, calibration was performed at every 10 K. There was ±24 mK uncertainty around 300 K.

A resistance of PT103 measured by a Lakeshore 218 diode temperature monitor is translated to temperature by this calibration curve. The linear

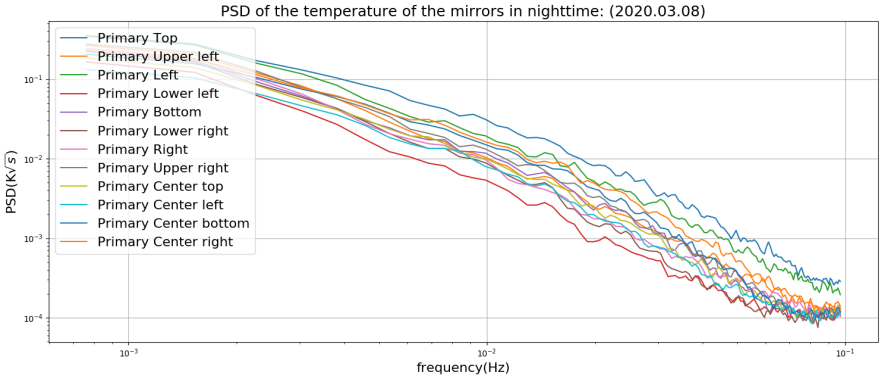

Figure 5.14: Temperature NSD of the primary mirror at night.

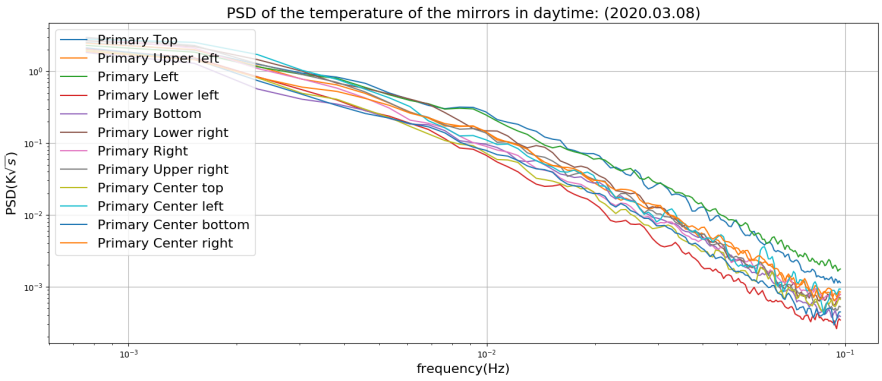

Figure 5.15: Temperature NSD of the primary mirror at daytime.

spline between two points $(R_{\mathrm{cal},1}, T_{\mathrm{cal},1})$ and $(R_{\mathrm{cal},2}, T_{\mathrm{cal},2})$ is expressed as

$$T = \frac{T_{\mathrm{cal},2} - T_{\mathrm{cal},1}}{R_{\mathrm{cal},2} - R_{\mathrm{cal},1}} \left(R_{\mathrm{meas}} - R_{\mathrm{cal},1}\right) + T_{\mathrm{cal},1}. \tag{5.1}$$

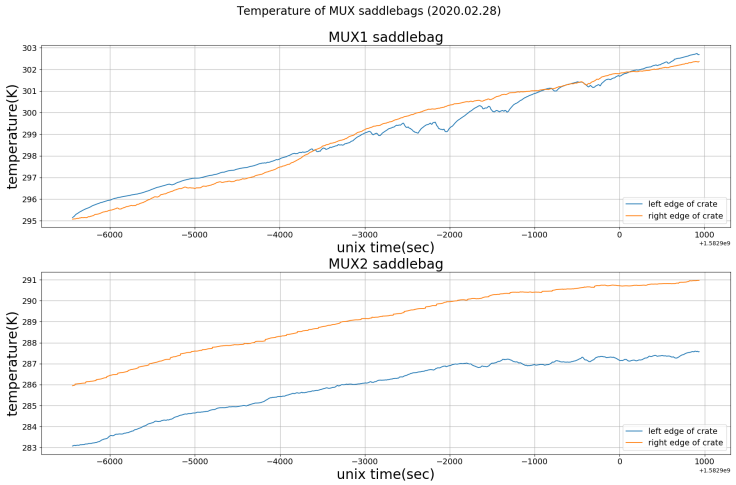

Figure 5.16: Temperature TOD of the MUX saddlebags. Each saddlebag has 2 thermistors.

Its statistical uncertainty is

$$
\begin{aligned}
(\delta T)^2 &= \left(\frac{dT}{dT_{\mathrm{cal},1}}\delta T_{\mathrm{cal},1}\right)^2 + \left(\frac{dT}{dT_{\mathrm{cal},2}}\delta T_{\mathrm{cal},2}\right)^2 + \left(\frac{dT}{dR_{\mathrm{cal},1}}\delta R_{\mathrm{cal},1}\right)^2 \\
&\quad + \left(\frac{dT}{dR_{\mathrm{cal},2}}\delta R_{\mathrm{cal},2}\right)^2 + \left(\frac{dT}{dR_{\mathrm{meas}}}\delta R_{\mathrm{meas}}\right)^2 \\
&= \left(\frac{R_{\mathrm{cal},2}-R_{\mathrm{meas}}}{R_{\mathrm{cal},2}-R_{\mathrm{cal},1}}\delta T_{\mathrm{cal},1}\right)^2 + \left(\frac{R_{\mathrm{meas}}-R_{\mathrm{cal},1}}{R_{\mathrm{cal},2}-R_{\mathrm{cal},1}}\delta T_{\mathrm{cal},2}\right)^2 \\
&\quad + \left(\frac{(T_{\mathrm{cal},2}-T_{\mathrm{cal},1})\,(R_{\mathrm{meas}}-R_{\mathrm{cal},2})}{(R_{\mathrm{cal},2}-R_{\mathrm{cal},1})^2}\delta R_{\mathrm{cal},1}\right)^2 \\
&\quad + \left(\frac{(T_{\mathrm{cal},2}-T_{\mathrm{cal},1})\,(R_{\mathrm{cal},1}-R_{\mathrm{meas}})}{(R_{\mathrm{cal},2}-R_{\mathrm{cal},1})^2}\delta R_{\mathrm{cal},2}\right)^2 \\
&\quad + \left(\frac{T_{\mathrm{cal},2}-T_{\mathrm{cal},1}}{R_{\mathrm{cal},2}-R_{\mathrm{cal},1}}\delta R_{\mathrm{meas}}\right)^2,
\end{aligned}
\tag{5.2}
$$

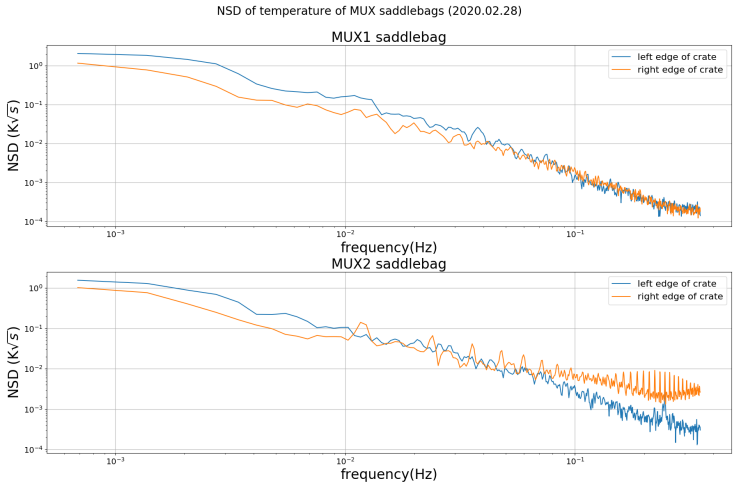

Figure 5.17: Temperature NSD of the MUX saddlebags.

and its systematic uncertainty is

$$\begin{aligned}\delta T \;=\; & \left|\frac{R_{\mathrm{cal},2}-R_{\mathrm{meas}}}{R_{\mathrm{cal},2}-R_{\mathrm{cal},1}}\delta T_{\mathrm{cal},1}\right| + \left|\frac{R_{\mathrm{meas}}-R_{\mathrm{cal},1}}{R_{\mathrm{cal},2}-R_{\mathrm{cal},1}}\delta T_{\mathrm{cal},2}\right| \\ & + \left|\frac{(T_{\mathrm{cal},2}-T_{\mathrm{cal},1})\,(R_{\mathrm{meas}}-R_{\mathrm{cal},2})}{(R_{\mathrm{cal},2}-R_{\mathrm{cal},1})^2}\delta R_{\mathrm{cal},1}\right| \\ & + \left|\frac{(T_{\mathrm{cal},2}-T_{\mathrm{cal},1})\,(R_{\mathrm{cal},1}-R_{\mathrm{meas}})}{(R_{\mathrm{cal},2}-R_{\mathrm{cal},1})^2}\delta R_{\mathrm{cal},2}\right| \\ & + \left|\frac{T_{\mathrm{cal},2}-T_{\mathrm{cal},1}}{R_{\mathrm{cal},2}-R_{\mathrm{cal},1}}\delta R_{\mathrm{meas}}\right|. \end{aligned} \tag{5.3}$$

The nominal uncertainty of Lakeshore 218 is $\delta R_{\mathrm{meas}} = \pm 0.06\ \Omega \pm 0.02\%$(reading) [57]. When it reads a $\sim$110 Ω resistor at 300 K, the error is $\pm 0.02(stat) \pm 0.06(sys)\ \Omega$. If we substitute to Eqs. (5.2)(5.3) the $(R_{\mathrm{cal},1}, T_{\mathrm{cal},1}) = (106.619, 290.035)$ and $(R_{\mathrm{cal},2}, T_{\mathrm{cal},2}) = (114.385, 310.029)$ from the datasheet of PT103, with the uncertainty $\delta T_{\mathrm{cal},1} = \delta T_{\mathrm{cal},2} = 24\ mK(sys)$ and $\delta R_{\mathrm{meas}} = \pm 0.02(stat) \pm 0.06(sys)\ \Omega$ and $\delta R_{\mathrm{cal},1} = \delta R_{\mathrm{cal},2} = 0$, the temperature uncertainty around 300.000 K is $\pm 0.03(stat) \pm 0.2(sys)$ K. Once a calibration curve made from the PT103 temperature, the statistical uncertainty is "fixed" as a systematic error and propagates to the uncertainty of thermistor temperature. Error at each point is the sum of quadrature of statistical and systematic uncertainty, namely $\pm 0.2(sys)$ K.

Then the uncertainty of thermistor temperature can be calculated. Recalling the measurement uncertainty of resistance with Keysight 34980A was $\pm 0.0020\%$(reading) $\pm 0.0005\%$(range), the resistance uncertainty around 3300 Ω ($\sim$300 K) is $\delta R_{\mathrm{meas}} = \pm 0.07(stat) \pm 0.05(sys)\ \Omega$. It is converted

to temperature using the neighbor points, $(R_{\rm cal,1}, T_{\rm cal,1}) = (3600, 297)$ and $(R_{\rm cal,2}, T_{\rm cal,2}) = (3000, 302)$. Each temperature's uncertainty is $\delta T_{\rm cal,1} = \delta T_{\rm cal,2} = \pm 0.2(sys)$ K. Then the uncertainty in translation from resistance to temperature is calculated by Eqs. (5.2)(5.3) as $\pm 0.0007(stat) \pm 0.2(sys)$ K.

The same calculation for LTC2983 with $\delta R_{\rm cal,1} = \delta R_{\rm cal,2} = \delta R_{\rm meas} = 0.01(stat)$ Ω leads $\pm 0.0001(stat)$ K.

Once we configure the resistance range of each measurement device, this systematic error does not appear in measurements of temperature fluctuation because of taking difference. Only statistical uncertainty times $\sqrt{2}$, namely $\pm 0.0009(stat)$ K for Keysight 34980A and $\pm 0.0001(stat)$ K for LTC2983, remains.

Resistance of a lead wire

Resistance of lead wires between a device and thermistors on the primary mirror is below 1 Ω including a connector. It corresponds to < 7 mK at 300 K.The wires to other instruments are shorter than this. This additional resistance is purely systematic and time-independent. Temperature coefficient of the lead has been measured to be ~ 0.01 Ω/K, which corresponds to 83 μK/K in temperature unit with the temperature coefficient of our thermistors. Assuming that the temperature of the leads fluctuates at the same extent as the mirrors and readout electronics, namely 10 mK$\sqrt{s}$ near the mirror and 20 mK$\sqrt{s}$ in the readout crate at 50 mHz, the temperature noise induced by the wire resistance becomes 0.83 μK$\sqrt{\rm s}$ for the mirror and 1.7 μK$\sqrt{\rm s}$ for the readout. In the case of taking difference of two points, noise becomes $\sqrt{2}$ times as above. It leads 1.2 μK$\sqrt{\rm s}$ for the mirror and 2.4 μK$\sqrt{\rm s}$ for the readout.

Self heating of a thermometer

The self heating of the thermistors are calculated by measuring rapid change of resistance right after connecting them to the measurement device. We set excitation current of a Lakeshore 218 diode temperature monitor to 10 μA±0.05% or 1 mA±0.3% and started to measure voltage. After that, we connected the thermistors to the monitor. With 1 mA current, we could see that the temperature of thermistors increased by the excitation. We calculated their resistance from voltage and constant current and fitted it to determine an equilibrium temperature. The heat dissipation constant, $\delta_{\rm heat}$, is defined as

$$\delta_{\rm heat} \equiv \frac{V_{\rm end} I}{T_{\rm end} - T_{\rm init}}, \tag{5.4}$$

where the $V_{\rm end}$ is voltage at equilibrium, I is a constant current, $T_{\rm end}$ and $T_{\rm init}$ are initial and equilibrium temperature, respectively. We derived a

mean heat dissipation constant of two silicone-sealed thermistor as 4.90 ± 0.006 mW/K in the 290 K atmosphere. In actual observations, an excitation current applied by Keysight 34980A at the site is 100 μA. It means that the typical power generated at a 3 kΩ thermistor is 0.03 mW. Therefore the temperature offset by the self heating is $\sim$6 mK. Assuming the ripple of the excitation current is $\pm$0.3% as same as the Lakeshore 218, it corresponds to $\pm$37 μK. The $\sqrt{2}$ times value, $\pm$52 μK, is accounted to fluctuation.

Mirror thickness

The temperature difference between back and front of the mirror is below 1 K, described in Sec. 5.4.2. We estimate the error of relative fluctuation by taking difference of fluctuations from mean value of each TOD as shown in the bottom row of Fig. 5.10. The standard deviation of the differential fluctuation between front and back of the bottom of the primary mirror is 43 mK at night and 333 mK in the daytime. At the center of the mirror, it is smaller but is at the same order. Uncertainty in difference of two points is 61 mK at night and 471 mK in the daytime. It includes the residual effect of the direct sunlight irradiating the thermometers on the front surface, although the sunshade is applied.

The simplest way to correct this temperature difference is to evaluate it in terms of delay of the back from the front. As a reference, Fig. 5.18 shows the time lag taken for back temperature to reach to the front temperature on sunrise. There is 80 sec delay for bottom of the mirror and 40 sec forward for center bottom. However, this can be easily change by the weather condition and the relative direction of the mirror to the sun. Actually the back temperature does not reach to the front temperature at its peak. It is more important to model the temperature difference in terms of environmental conditions.

Temperature distribution on the mirror

Another systematic related to the mirror is the temperature distribution on the surface. An example of the temperature distribution on the back of the primary mirror is shown in Fig. 5.19. There is temperature difference up to 4 K between edge and the center of the mirror. It is because of the sun direction and the supporting structure which prevents wind from reaching to the center of the back surface. Timestreams of the temperature difference between edge and center in day and night are shown in Fig. 5.20. Standard deviation of the difference of the temperature fluctuation is at most 140 mK at night and 1.5 K in the daytime. Uncertainty in difference of two points is 198 mK at night and 2.1 K in the daytime.

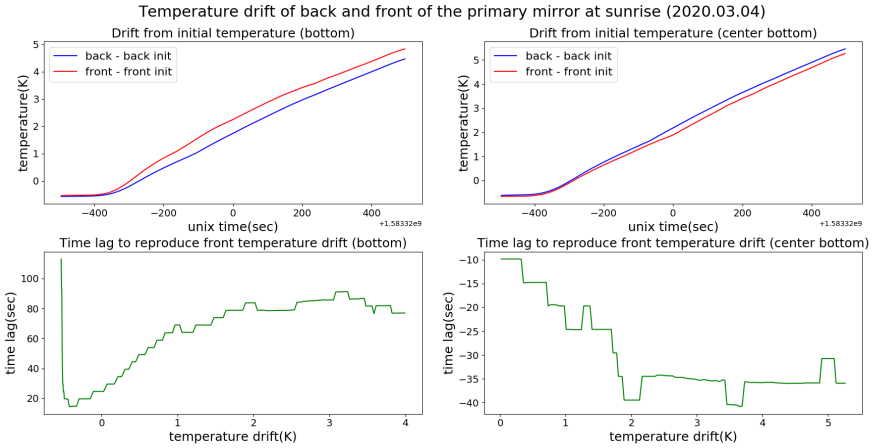

Figure 5.18: TODs of temperature difference between edge and center of the primary mirror. "Center" is the mean of four thermometers on the center. The top row shows temperature difference and the bottom shows difference of fluctuation from the mean value of each location. The left column is data in the daytime and the right is at night.

Temperature distribution in the readout crate

For readout electronics, temperature distribution in the saddlebag is an apparent source of systematic. We imitated the readout crate by the thermal chamber in KEK laboratory and measured temperature difference between mezzanine board and the metal wall. The distance from the board to the wall was 35 cm (Fig. 5.21), which was close to the condition at the site. In spite of the risk of short by a copper chip, we measured temperatures of the board and the wall with a thermistor to make the noise level same along the two. The board was turned on and the air was circulated by a fan, and the temperature was not regulated.

The temperature TODs and their difference for 9 hours are shown in Fig. 5.22. Trend of the wall temperature roughly followed the board as well as its fluctuation. However, the board temperature fluctuates more than the wall because of Joule heat and cooling fan. The temperature of the wall linearly follows the board (Fig. 5.23) but there is up to 1.5 K difference in the absolute values, and the standard deviation of differential fluctuation is 25 mK. Uncertainty in difference of two points is 55 mK. The error in the absolute value can be calibrated using the built-in temperature sensor on the boards and the error in the relative fluctuation will be compensated by constructing a specific model of heat convection between the board and the wall.

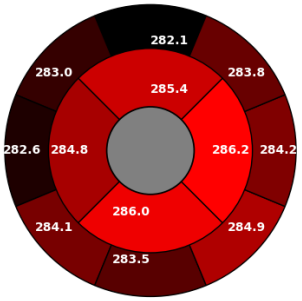

Figure 5.19: A slice of temperature distribution on the back of the primary mirror in the morning at the site.

Source	Error on the mirror	Error on the readout
Calibration&measurement	$\pm$0.9 mK (2.0 mK$\sqrt{s}$)	$\pm$0.1 mK (0.1 mK$\sqrt{s}$)
Resistance of a lead wire	1.2 μK$\sqrt{s}$ at 50 mHz	2.4 μK$\sqrt{s}$ at 50 mHz
Self heating of a thermometer	$\pm$52 μK (74 μK$\sqrt{s}$)	$\pm$52 μK (52 μK$\sqrt{s}$)
Mirror thickness	471 mK (1053 K$\sqrt{s}$) in daytime 61 mK (136 mK$\sqrt{s}$) at night	-
Distribution on the mirror	2.1 K (4.7 K$\sqrt{s}$) in daytime 198 mK (443 mK$\sqrt{s}$) at night	-
Distribution in the readout crate	-	$\pm$25 mK (25 mK$\sqrt{s}$)
Total	$\pm$745 mK$\sqrt{s}$	$\pm$25 mK$\sqrt{s}$

Table 5.2: Uncertainty on the relative temperature fluctuation of the mirror measured by warm temperature monitors.

5.7 Summary of warm temperature monitors

We summarize the uncertainty of relative temperature fluctuation discussed above in Tables. 5.2. The random noise in the unit of K is translated to K$\sqrt{s}$ by multiplying square root of the sampling rate, 5 sec for the mirror and 1 sec for the readout electronics. The uncertainty of absolute temperature is also shown in Tables. 5.3, but note that its systematic error does not appear in the measurement of temperature fluctuation.

Judging based on the night NSDs of the mirror or the NSDs of MUX1 saddlebag, we have achieved the sufficiently low measurement noise for temperature correction. It satisfies the requirements to PB2 whether we use HWP or not, and a realistic improvement may enable us to perform temperature correction in Simons Array and other more sensitive experiments

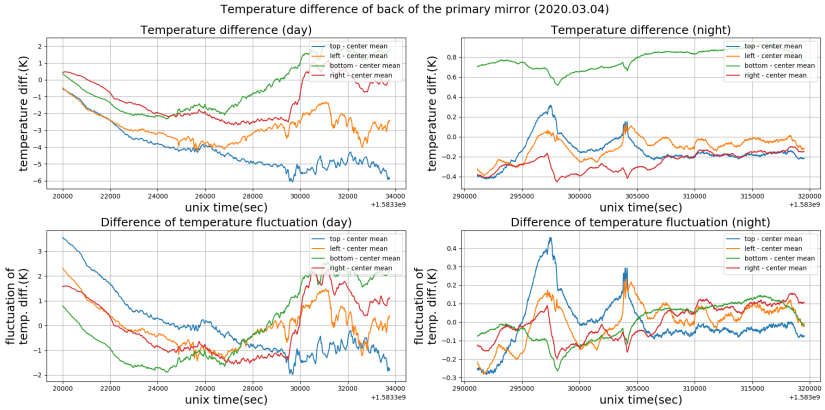

Figure 5.20: TODs of temperature difference between edge and center of the primary mirror. "Center" is the mean of four thermometers on the center. The top row shows temperature difference and the bottom shows difference of fluctuation from the mean value of each location. The left column is data in the daytime and the right is at night.

in future.

Furthermore, there is a large systematic error originates to the distance between thermometers and target instruments. Detailed understanding of these temperature distribution is necessary for more sensitive experiments or other analysis using absolute temperature. We will translate them into the uncertainty of tensor-to-scalar ratio in Sec. 7.1.

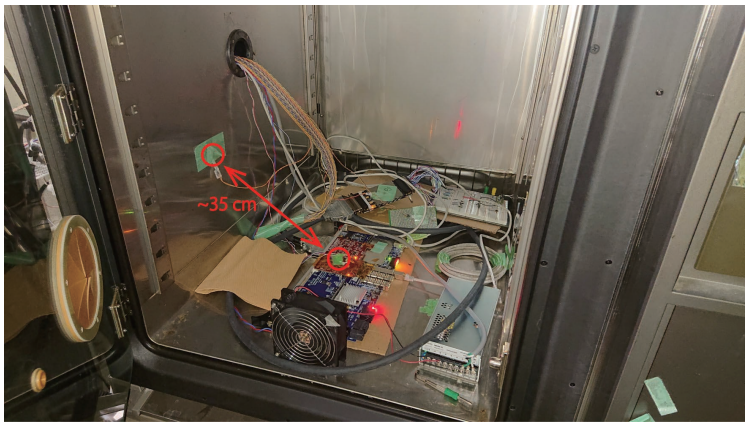

Figure 5.21: Laboratory setup to measure temperature difference between the mezzanine board and the neighboring wall.

Source	Error on the mirror	Error on the readout
Calibration&measurement	$\pm 0.0007(stat) \pm 0.2(sys)$ K	$\pm 0.0001(stat)$ K
Resistance of a lead wire	$-7(sys)$ mK	$-7(sys)$ mK
Self heating of a thermometer	$+6(sys)$ mK	$+6(sys)$ mK
Mirror thickness	$\pm 1(sys)$ K	-
Distribution on the mirror	$\pm 4(sys)$ K	-
Distribution in the readout crate	-	$\pm 1.5(sys)$ K
Total	$\pm 0.0007(stat) \pm 4(sys)$ K	$\pm 0.0001(stat) \pm 1.5(sys)$ K

Table 5.3: Uncertainty on the absolute value of one data point of warm temperature monitors.

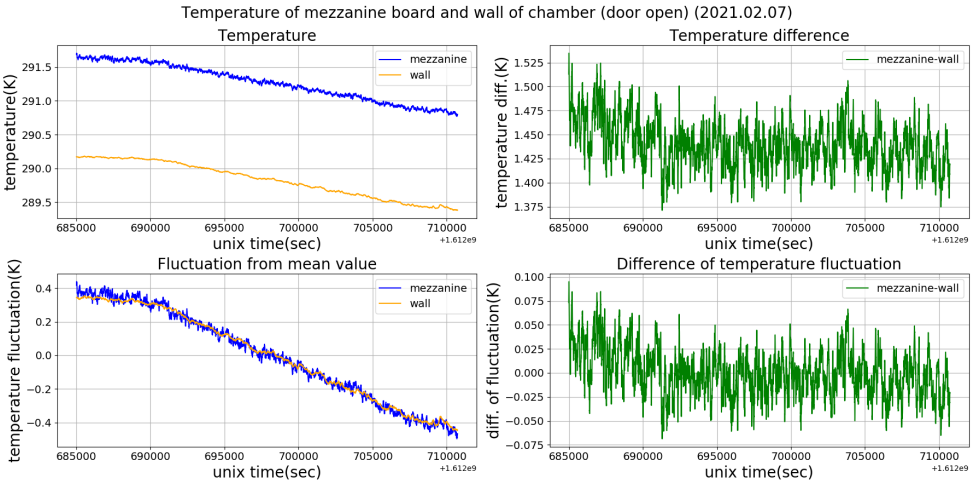

Figure 5.22: Temperatures of the mezzanine board and the metal wall, and their difference.(*top left*) Temperature TODs. (*top right*) Temperature difference. (*bottom left*) Fluctuation from the mean temperature. (*bottom right*) Difference between fluctuations from respective mean value of the board and the wall.

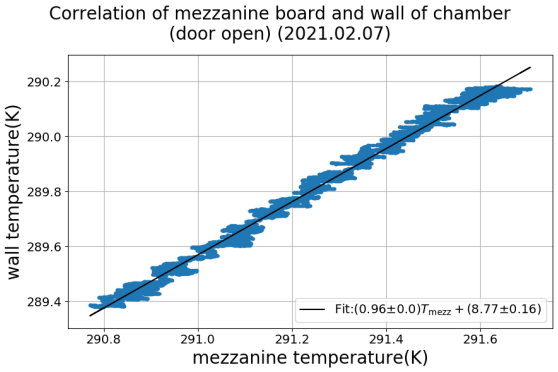

Figure 5.23: Correlation plot of the board temperature and the wall temperature. *blue cirle:* Measured temperature. *black line:* Linear fitting.

6

Demonstration of temperature correction

6.1 Preparation of temperature-modulated data

This chapter demonstrates the correction of temperature modulation on the detector signal, using the mezzanine board as an example. We monitor the instrument temperatures in parallel with the detectors and subtract them by already derived temperature coefficients. Then we discuss the improvement of the low-frequency noise spectrum by this correction.

We prepared model data in which the instrumental effects other than the temperature modulation of mezzanine boards were canceled. We separated IceBoards for the full TES array into two groups and set them in independent racks. Then we tuned the TESes and injected reference millimeter waves modulated by a chopper rotating at 14 Hz. Here we used a beam mapper, a device for originally characterizing detector beam, as a reference light source. In parallel, we changed the temperature in the two readout racks to modulate the TES signal (Fig. 6.1). We attached the thermometers directly on the mezzanine board located close to the center of each crate. In this measurement, we used PT103-14L platinum resistors provided by Lakeshore Inc. as thermometers because they were covered with ceramic so that they would not cause short. We read them with a Lakeshore 218 diode temperature monitor.

For each TES group which is read by electronics in each rack, we calculated the weighted-mean of signals. We determined the weighted-mean TOD as

$$d_* \equiv \frac{\sum_i^N \langle \mathcal{F}_i(f)|_{12.0<f<13.0,14.5<f<15.5}\rangle^{-1} d_{*,i}}{\sum_i^N \langle \mathcal{F}_i(f)|_{12.0<f<13.0,14.5<f<15.5}\rangle^{-1}}, \tag{6.1}$$

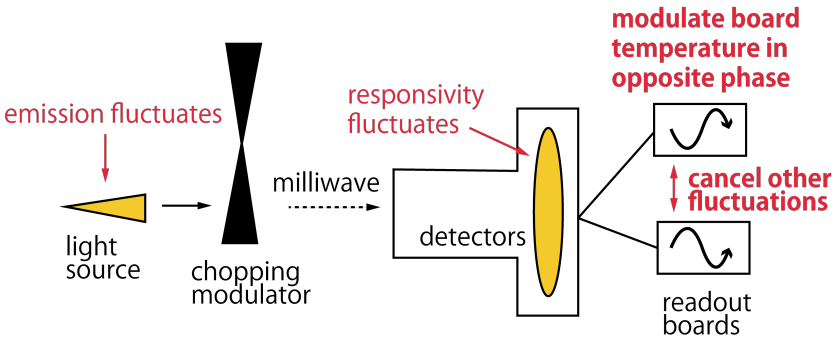

Figure 6.1: Setup to prepare the TES signal modulated by mezzanine temperature. A light source with a 14 Hz chopper for beam characterization was used as a reference light. The readout boards were divided into two groups, and their temperature was modulated independently.

where $d_{*,i}$ indicates the i-th TES read by $*$-th ($* \in (1,2)$) crate. We used the inverse of the mean noise floor around the 14 Hz peak as the weight.

The weighted-mean TODs from the crate 1 and 2 are described by simplifying Eq. (4.6) like

$$P_{\rm in} \equiv (b + \Delta b) \sin 2\pi f_b t + B_{\rm drop} \Delta T_{\rm bath}, \tag{6.2}$$

$$\begin{aligned} d_* \simeq\ & g_0 \left\{1 + A_{\rm resp}\Delta T_{\rm bath} + A_{\rm read,SQCB}\Delta T_{\rm SQCB} + A_{\rm read,mezz}\Delta T_{\rm mezz,*} + g_1 P_{\rm in}\right\} \cdot P_{\rm in} \\ & + A_{\rm bias,SQCB}\Delta T_{\rm SQCB} I_{\rm bias} + A_{\rm bias,mezz}\Delta T_{\rm mezz,*} I_{\rm bias} + \Delta N, \end{aligned} \tag{6.3}$$

where $* \in (1,2)$, $b + \Delta b$ is the time-dependent amplitude of the reference light and f_b is its chopping frequency. The last ΔN is white noise.

We demodulated the two weighted-mean TODs at 14 Hz to derive input signal, b, and its temperature modulation. The demodulated signal is

$$\begin{aligned} d_{\rm demod,*} =\ & g_0 \left\{1 + (A_{\rm resp} + 2 g_1 B_{\rm drop})\, \Delta T_{\rm bath} + A_{\rm read,SQCB}\Delta T_{\rm SQCB} \right. \\ & \left. + A_{\rm read,mezz}\Delta T_{\rm mezz,*}\right\} (b + \Delta b) + \Delta N. \end{aligned} \tag{6.4}$$

The demodulated signals of two crates are shown in *top left* of Fig. 6.2, and the board temperatures are in *top right* of the same figure.

Then we normalized the weighted-mean TODs by their mean value and took their difference in order to cancel other effects such as temperature fluctuation of the focal plane and variation of the intensity of light. The difference of two racks is

$$\frac{d_{\rm demod,1}}{\langle d_{\rm demod,1}\rangle} - \frac{d_{\rm demod,2}}{\langle d_{\rm demod,2}\rangle} \simeq A_{\rm read,mezz}\left(\Delta T_{\rm mezz,1} - \Delta T_{\rm mezz,2}\right) + \Delta N. \tag{6.5}$$

Here we ignored the square terms of fluctuations indicated by Δ. This Eq. 6.5 is what is shown in *middle left* of Fig. 6.2. The temperature difference $\Delta T_{\rm mezz,1} - \Delta T_{\rm mezz,2}$ is shown in *middle right* of the figure.

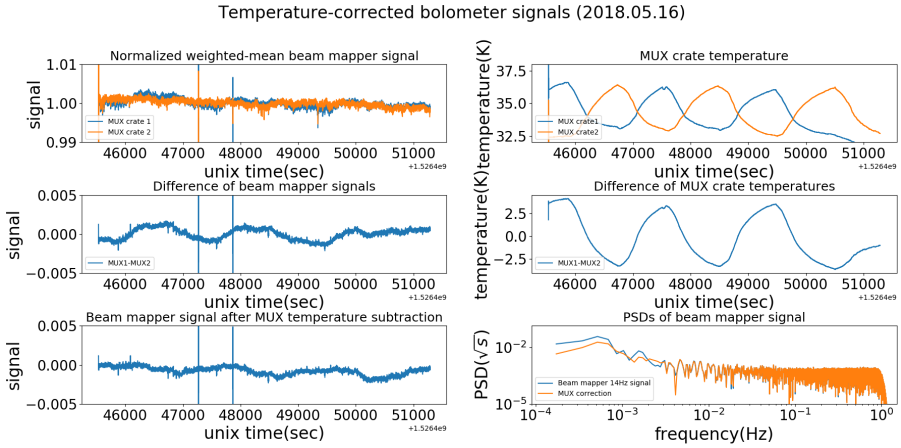

Figure 6.2: TES time-stream and power spectra. (*top left*) Demodulated reference signal read by boards in two racks. (*top right*) Saddlebag temperature. (*middle left*) Difference of TOD of boards in two racks. (*middle right*) Difference of saddlebag temperature. (*bottom left*) Differential TOD after subtraction of saddlebag temperature. (*bottom right*) NSDs of the signal before and after the temperature correction.

We converted the temperature drift to signal fluctuation by multiplying it by the temperature coefficient which we measured in Sec. 4.3.1, approximately -500ppm/K. Then we subtracted it from the differential weighted-mean signal (From *middle left* to *bottom left* in Fig. 6.2). Ideally it leaves only white noise.

$$\frac{d_{\mathrm{demod},1}}{\langle d_{\mathrm{demod},1}\rangle} - \frac{d_{\mathrm{demod},2}}{\langle d_{\mathrm{demod},2}\rangle} - A_{\mathrm{read,mezz}}\left(\Delta T_{\mathrm{mezz},1} - \Delta T_{\mathrm{mezz},2}\right) \simeq \Delta N. \quad (6.6)$$

Noise spectrum densities before and after this subtraction are shown as *bottom right* in Fig. 6.2. We can see the noise at a lower frequency than 5 mHZ was reduced by factor of 2. Here we determined the correction factor ξ as

$$\xi \equiv \sqrt{\left(\sum_f^{f_c} \mathrm{NSD}^2_{\mathrm{before}}\right) \Big/ \left(\sum_f^{f_c} \mathrm{NSD}^2_{\mathrm{after}}\right)}, \quad (6.7)$$

where f_c is the maximum frequency of correction determined by sampling rate of a temperature monitor, and $\mathrm{NSD}_{\mathrm{before/after}}$ is noise spectrum before and after correction, respectively. In our correction, $\xi = 1.8$ at $f_c = 50$ mHz.

The noise spectrum densities of temperature measurement were 20 $\mathrm{mK}\sqrt{\mathrm{s}}$ at 50 mHz in this measurement (Fig. 6.3), so that this result is not limited by the measurement precision. Cause of remained $1/f$ noise is

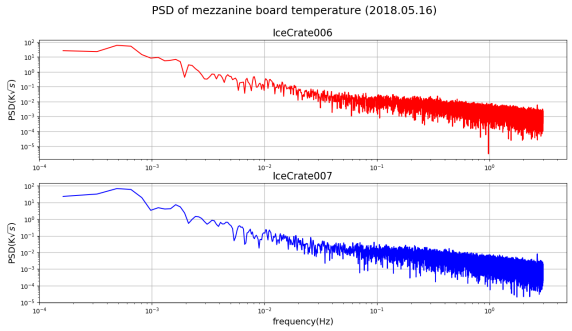

Figure 6.3: Noise spectrum density of temperature of the readout board in each crate.

supposed to be temperature variation in the readout crate and on the focal plane.

6.2 Bias by error of temperature coefficient

When we perform temperature coefficient, we multiply temperature TOD by a specific coefficient evaluated before. The error in this coefficient induces systematic bias into the detector TOD.

We evaluated the noise induced by the error of temperature coefficient by simulating the temperature correction for many subscans. First we generated "true" mezzanine temperature TODs from a $1/f$ noise spectrum derived by fitting the on-site data. Then we sampled it with a sampling rate of temperature monitor, typically 5 seconds. The length of the TOD was 50 seconds, which corresponds to the time to scan 20 degree scale by 0.4°/s. We interpolated the "measured" temperature by bicubic interpolation in order to make it match the sampling rate of detector readout. For simplicity of computing, we set the detectors' sampling rate to f_c =10 Hz. In parallel, we multiplied the "true" temperature by a temperature coefficient without HWP evaluated in Sec. 4.3.1 and added it to a TOD of 5 $\mu\mathrm{K}\sqrt{\mathrm{s}}$ white noise. After that, we subtracted "measured and interpolated" temperature TOD from detector signal.

We repeated these to 41697 realizations. This is the approximate number of subscan, determined by dividing total observation time by duration of one subscan. The scan parameters are almost same as POLARBEAR, namely the project period is 3 years, scan efficiency is 18%, width of a sky patch is 20 degrees, scan speed is 0.4°/s [39] but only the total sky coverage is 65% [34]. Then the observation time is 1.7×10^7 seconds and the white noise spectra of averaged TOD should be NET $= 5\ \mu\mathrm{K}\sqrt{\mathrm{s}}/\sqrt{41697} \sim 2.4 \times 10^{-2}\ \mu\mathrm{K}\sqrt{\mathrm{s}}$.

We show the result of simulation in Fig. 6.4. The coefficient with −100%

error corresponds to not doing correction. The total noise of the averaged TOD is parameterized as

$$n(f) = \mathrm{NET}_{\mathrm{array}} + \mathrm{NET}_{\mathrm{temp}} \left(\frac{f}{f_c} \right)^{-\alpha}. \tag{6.8}$$

In our case, $f_c = 0.1$. The error of temperature coefficient multiplies $\mathrm{NET}_{\mathrm{temp}}$. From the simulation results, $\alpha = -2.3$ and $\mathrm{NET}_{\mathrm{temp}} = 0.024\ \mu K\sqrt{s}$ at -100% error. We need to determine the coefficient correction with accuracy of briefly -100%∼+80% of the true value to avoid that the correction adds excess noise larger than temperature fluctuation itself. Being more strictly, to suppress the temperature noise component over all frequency range in $0.02 \leq f \leq f_c$ below array sensitivity, the coefficient error should be determined with accuracy of $\pm 2.5\%$.

We performed the same simulation with a spectrum of the primary mirror (Fig. 6.5) and it gives -100%∼80% to suppress bias to be comparable to temperature fluctuation. Since the parameters are $\alpha = -0.8$ and $\mathrm{NET}_{\mathrm{temp}} = 0.103\ \mu K\sqrt{s}$ at -100% error, the requirement to make the bias below array sensitivity is 6.4%.

6.3 Summary of temperature correction

We corrected actual TES time-stream data with the mezzanine board temperature and confirmed that the noise spectrum was reduced by factor of two in low frequency below 5 mHz. The impact of correction should become more apparent in higher frequency when the temperature fluctuation has a more complicated waveform.

We also performed simulation to check the behavior in a long-term observation. With observations for three years, error of estimation of a temperature coefficient makes residual $1/f$ noise in the averaged TOD. The least requirement to the coefficient error is from -100% to +80%, and more strictly we can impose 2.5% for the mezzanine board and 6.5% for the primary mirror. Our current temperature coefficient of nuller current on the mezzanine board satisfies this strict requirement but the one for bias current of TES is not. The coefficient of mirror should be measured with the actual setup at the site.

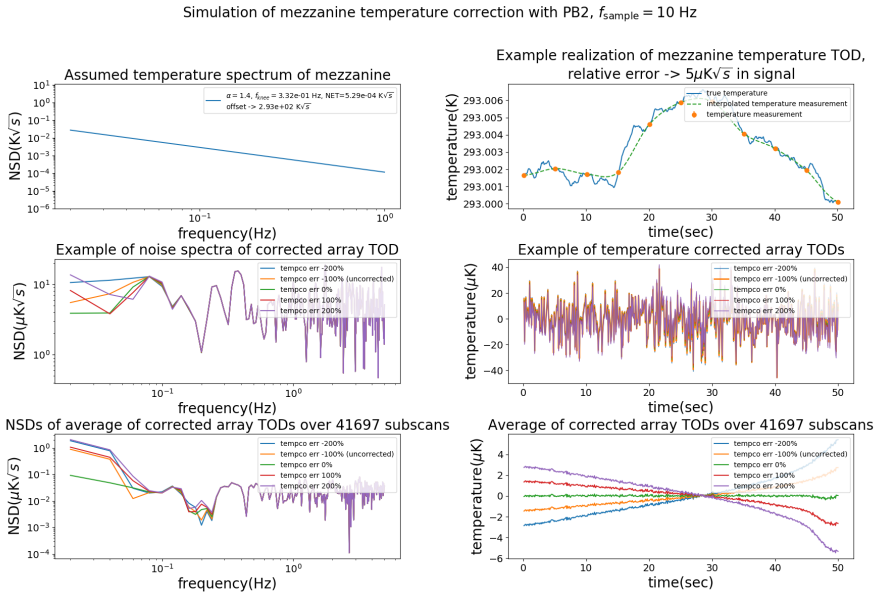

Figure 6.4: Simulation of temperature correction to 41697 realization. (*top left*) Assumed $1/f$ noise spectrum of mezzanine temperature. (*top right*) *blue solid line:* True temperature TOD generated by the assumed spectrum. *orange points:* Simulated measurement data with slower sampling rate. *blue dashed line:* Bicubic interpolation of measurement data. (*middle left*) Noise spectra of temperature-corrected detector TODs with various error of the temperature coefficient. (*middle right*) Temperature-corrected detector TODs with various error of the temperature coefficient. One realization is shown here. (*bottom left*) NSDs of average of 41697 corrected TOD. (*bottom right*) Average of 41697 corrected TOD.

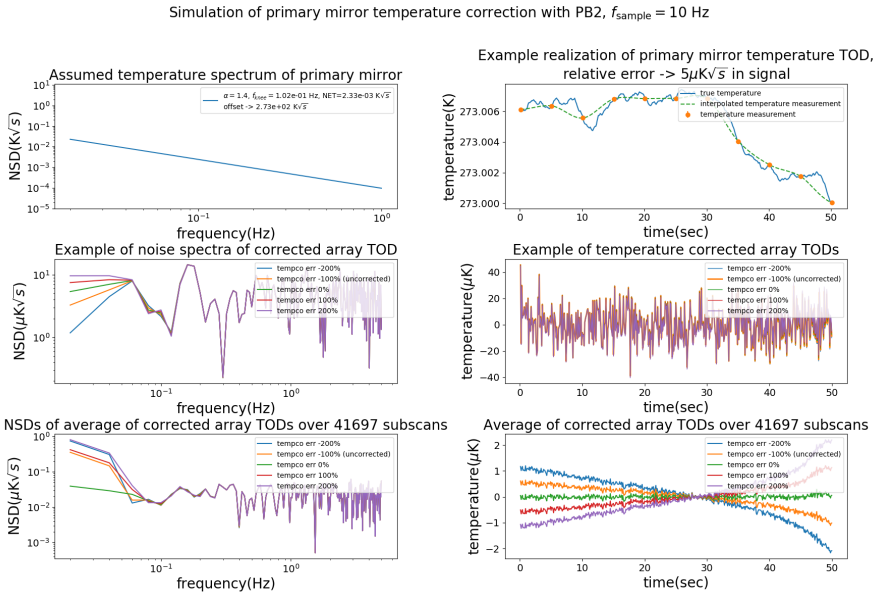

Figure 6.5: Simulation of temperature correction to 41697 realization. (*top left*) Assumed $1/f$ noise spectrum of primary mirror temperature. (*top right*) *blue solid line:* True temperature TOD generated by the assumed spectrum. *orange points:* Simulated measurement data with slower sampling rate. *blue dashed line:* Bicubic interpolation of measurement data. (*middle left*) Noise spectra of temperature-corrected detector TODs with various error of the temperature coefficient. (*middle right*) Temperature-corrected detector TODs with various error of the temperature coefficient. One realization is shown here. (*bottom left*) NSDs of average of 41697 corrected TOD. (*bottom right*) Average of 41697 corrected TOD.

7

Future forecasts

7.1 Analytical estimation of uncertainty of the cosmological parameters

Temperature correction described in Sec. 6 reduces the $1/f$ noise at specific frequencies depending on the sampling rate of the temperature monitors. It results in the reduction of statistical uncertainty of r if the noise of temperature measurement is lower than $1/f$ fluctuation and array sensitivity. This chapter describes the improvement of accuracy of r realized by various correction levels and sampling rates.

The statistical uncertainty of r, here denoted as $\sigma(r)$, is calculated by Eqs. (2.1)(2.2)(2.12). Here we write them down again,

$$w_P = \frac{1}{\mathrm{NEPol}^2} \frac{t_{\mathrm{obs}}}{4\pi f_{\mathrm{sky}}}, \tag{7.1}$$

$$W_\ell = \exp\left[-\ell\left(\ell+1\right)\frac{\theta^2_{\mathrm{FWHM}}}{8\log 2}\right], \tag{7.2}$$

$$\sigma\left(r=0\right) = \left[\sum_\ell \frac{\left(2\ell+1\right) f_{\mathrm{sky}}}{2}\left(\frac{\bar{C}^{BB}_\ell\left(r=1\right)}{w_P^{-1}W_\ell^{-1}}\right)^2\right]^{-\frac{1}{2}}. \tag{7.3}$$

Here NEPol$\equiv\sqrt{2}$NET is a noise-equivalent polarization temperature of the detector array, f_{sky} is a fraction of sky coverage, t_{obs} is an observation time, θ_{FWHM} is a FWHM of beam of each detector. $\bar{C}^{BB}_\ell$ is B-mode spectrum without foreground or lensing. To include effects of foreground removal, we define r_{eff} as an effective contribution to r from foreground residual and Δ_{fg} as noise term induced by removal [27]. They modify the forecast as

$$\sigma\left(r=0\right) = \left[\sum_\ell \frac{\left(2\ell+1\right) f_{\mathrm{sky}}}{2}\left(\frac{\bar{C}^{BB}_\ell\left(r=1\right)}{\Delta_{\mathrm{fg}}\cdot w_P^{-1}W_\ell^{-1} + r_{\mathrm{eff}}\bar{C}^{BB}_\ell\left(r=1\right)}\right)^2\right]^{-\frac{1}{2}}. \tag{7.4}$$

We use typical values for Simons Array, $r_{\rm eff} = 0.005$ and $\Delta_{\rm fg} = 3.0$.

Assuming that there is only NEPol and no $1/f$ noise in POLARBEAR-2 and using designed values on Table 3.2, we obtain $\sigma(r=0) \simeq 0.009$. Here the observation efficiency is 18% and the sky coverage is 65% [34], and $\bar{C}_\ell^{BB}$ at $r=1$ was calculated by `CAMB` [58].

A noise spectrum consists of white noise and $1/f$ noise can be fitted by

$$\mathrm{NSD} = \mathrm{NET}_{\rm temp}\left[1 + \left(\frac{\ell}{\ell_{\rm knee}}\right)^{-\alpha}\right], \tag{7.5}$$

where $\mathrm{NET}_{\rm temp}$ is a level of white noise, α is a slope of $1/f$ noise and $\ell_{\rm knee}$ is a frequency where the contribution of $1/f$ noise become equal to the white noise. Since our discussion is based on noise spectrum density, the unit of NSD is $\mu\mathrm{K}\sqrt{\mathrm{s}}$.

In our estimation of $\sigma(r)$, a basic white noise is that of the TESes. It is what was introduced as total statistical noise N_ℓ in Sec. (2.5). Using the map depth w_P and the window function W_ℓ, the polarization noise with $1/f$ component is

$$N_\ell = \mathrm{NSD}^2 w_P^{-1} W_\ell^{-1}. \tag{7.6}$$

Note that this represents the array-averaged noise of co-added observations. Since all the detectors are affected by almost the same temperature fluctuation, the $1/f$ noise is correlated over all detectors and not mitigated by averaging.

Here we estimate the uncertainty of r induced by the temperature correction. We treat the systematic errors in the measurement of temperature fluctuation discussed in Sec. 5.6 as excess noise added to NEPol. First we converted them into the signal fluctuation using the temperature coefficient shown in Table. 4.3 and Table. 4.4. Then we translated them to $\sigma(r)$ by

$$\sigma_{\rm sys}\left(r=0\right) = \left[\sum_\ell \frac{\left(2\ell+1\right) f_{\rm sky}}{2}\left(\frac{\bar{C}_\ell^{BB}\left(r=1\right)}{\Delta_{\rm fg}\cdot\left(\delta\Delta T\right)^2 \frac{4\pi f_{\rm sky}}{t_{\rm obs}} W_\ell^{-1}}\right)^2\right]^{-\frac{1}{2}}, \tag{7.7}$$

where $\delta\Delta T$ is a systematic error in the unit of signal. We summarized $\delta\Delta T$ and $\sigma_{sys}(r=0)$ in Table. 7.1 and Table. 7.2. We used temperature coefficient of the without-HWP case at 150 GHz to show the upper limit of the $\sigma_{\rm sys}(r=0)$.

The largest systematic source is the temperature distribution on the mirror. It will be suppressed by constructing temperature gradient maps and assign different temperature TOD to respective detectors or wafers.

The second largest systematic raises from temperature difference between back and front of the mirror. As we can see in Fig. 5.10, It is time-dependent even at night. We can suppose that it is caused by the different condition of wind and sunlight between back and front. The thickness of the

Source	Error in the temperature unit	Error in the signal unit at 150 GHz	$\sigma_{\rm sys}(r=0)$
Calibration&measurement	2.0 mK$\sqrt{s}$	0.66 μK$\sqrt{\rm s}$	1.1×10^{-4}
Resistance of a lead wire	1.2 μK$\sqrt{\rm s}$	4.0×10^{-4} μK$\sqrt{\rm s}$	4.1×10^{-11}
Self heating of a thermometer	74 μK$\sqrt{s}$	0.24 μK$\sqrt{\rm s}$	1.5×10^{-5}
Mirror thickness	1053 mK$\sqrt{s}$ in daytime	347 μK$\sqrt{\rm s}$	31
Distribution on the mirror	4.7 K$\sqrt{s}$ in daytime	1551 μK$\sqrt{\rm s}$	612

Table 7.1: Uncertainty of r induced by the systematic error of the mirror temperature measurement.

Source	Error in the temperature unit	Error in the signal unit	$\sigma_{\rm sys}(r=0)$
Calibration&measurement	0.1 mK$\sqrt{s}$	5×10^{-3} $\mu K\sqrt{s}$	6.4×10^{-9}
Resistance of a lead wire	2.4 μK$\sqrt{\rm s}$	1.2×10^{-4} μK$\sqrt{\rm s}$	3.7×10^{-12}
Self heating of a thermometer	52 μK$\sqrt{s}$	2.6×10^{-3} μK$\sqrt{\rm s}$	1.7×10^{-9}
Distribution in the readout crate	25 mK$\sqrt{s}$	1.3 μK$\sqrt{\rm s}$	4.3×10^{-4}

Table 7.2: Uncertainty of r induced by the systematic error of the readout temperature measurement.

mirror is only 1 cm but the heat is carried away by the heavy wind on the front surface before it is transferred to the back. Constructing a model to describe the thermal transfer in the mirror in terms of the solar radiation, sun direction and wind speed will suppress this error.

7.2 Forecast of $\sigma(r)$ with temperature correction

In this section, we provide forecasts of $\sigma(r)$ with an ideal temperature correction. For the simplicity of estimation, we fix the correction level, i.e., the residual white noise remaining after correction, to 5 μK$\sqrt{\rm s}$. The precision of most of our temperature monitoring systems is better than that. When the noise is still larger than the correction level at ℓ_c, it just remains uncorrected. On the other hand, when the noise gets smaller than the correction level at a certain frequency below ℓ_c, the correction does not go further. This situation is conceptually shown in Fig. 7.1.

All instrumental temperatures have different noise properties. In Fig. 7.2, we show noise spectra of temperatures of various instruments discussed in Chapter 4. The measurement noise is sufficiently lower than the temperature noise spectra (See Sec. 5.6 for mirror and readout). Note that the temperatures of the focal plane and the Lyot stop were measured in laboratory so that their contributions should change at the site because of instability of cooling or vibration during observations. However, if the temperature offset

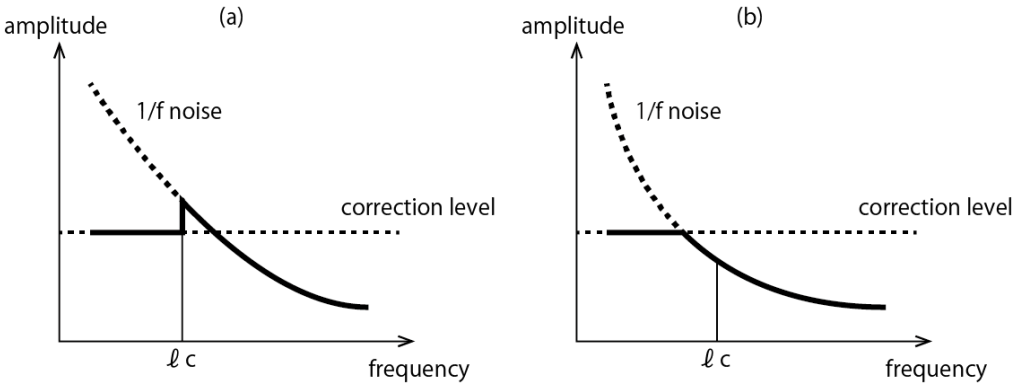

Figure 7.1: Concept of an ideal temperature correction on noise spectra. (a) Noise in the range of correction is only corrected. (b) The noise smaller than the correction level is not corrected even if it is in the correction range.

Instrument	α	$f_{\rm knee}$ [Hz] ($\ell_{\rm knee}$)	NET [K$\sqrt{\rm s}$]
focal plane	1.1	0.75 (678)	2.03×10^{-7}
Lyot stop	0.8	0.15 (133)	1.52×10^{-3}
primary mirror	1.4	0.10 (92)	2.33×10^{-3}
mezzanine board	1.4	0.33 (299)	5.29×10^{-4}

Table 7.3: Fitted $1/f$ noise parameters of instrumental temperature.

and optical efficiency are not changed, we can expect the same temperature coefficients.

By fitting the temperature noise spectra with Eq. (7.5), We obtain α and $\ell_{\rm knee}$, which are summarized in Table 7.3. The frequency is translated to an observed ℓ through the scan speed as

$$\ell_{\rm obs} = 180^\circ \frac{2f\ [\rm Hz]}{v_{\rm scan}\ [\rm deg/s]}. \tag{7.8}$$

The scan speed for large-patch observations at POLARBEAR-2 is 0.4°/s.

We also fitted the total noise spectra of temperature fluctuation plus detector noise (Fig. 7.3). We converged the temperature fluctuation to signal fluctuation by the temperature coefficients of without-HWP case at 90 GHz shown in Table. 4.4 and added polarization white noise of detectors. We assumed 500 μK$\sqrt{\rm s}$ for single detector, 5 μK$\sqrt{\rm s}$ for PB2 array and 3.4 μK$\sqrt{\rm s}$ for Simons Array. The fitted parameters are shown in Table. 7.4.

For example, the temperature fluctuation of the mezzanine board has $\alpha = 1.5$ and $f_{\rm knee} > 0.1$ Hz, corresponding to $\ell_{\rm knee} > 90$. When the array noise of PB2 is added, the $\ell_{\rm knee}$ becomes 107.

In Chapter 4, we calculated the requirements to the precision of temperature monitoring under a condition that temperature noise should be

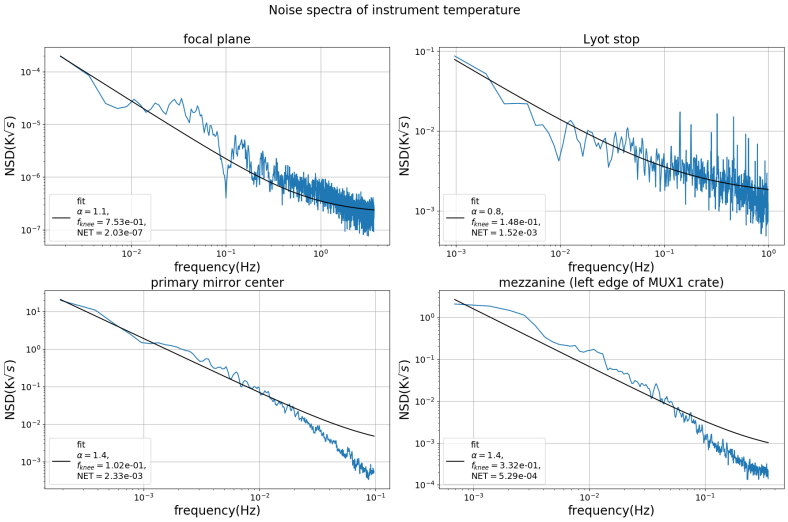

Figure 7.2: Noise spectral density (NSD) of temperature of six components of PB2. Blue lines are measured temperature noise and black lines are fitting with power law. (*top left*) Focal plane, (*top right*) Lyot stop, (*bottom left*) average of 4 thermometers at the center of primary mirror, (*bottom right*) mezzanine board.

reduced down to statistical array sensitivity to polarization. Since our requirements are imposed at 50 mHz, which corresponds to $\ell \sim 50$, an ideal correction makes the temperature noise in $25 \leq \ell \leq 50$ the same level as array NEPol. We write the maximum ℓ that we can correct, typically 50, as ℓ_c. The minimum ℓ, 25 for PB2 and Simons Array, is determined by each sub-scan's azimuthal length. If the corrected temperature noise with the amplitude of NEPol is added to the NEPol white noise, the total noise level becomes $\sqrt{2}$NEPol.

We reconstructed corrected temperature noise spectrum of each instrument by substituting $1/f$ parameters in Table 7.3 into Eq. 7.5. Then we

	PB2/SA		
Instrument	α	$\ell_{\rm knee}$	NET [μK$\sqrt{\rm s}$]
focal plane	1.0/1.0	777/777	25.3/25.2
Lyot stop	0.8/1.0	15/15	4.61/3.46
primary mirror	1.3/1.3	45/55	3.69/2.93
mezzanine board	1.1/1.1	107/127	5.73/3.98

Table 7.4: Fitted $1/f$ noise parameters of instrumental temperature added to detector array noise of POLARBEAR-2 (5.0 μK$\sqrt{\rm s}$ for polarization) or Simons Array (3.4 μK$\sqrt{\rm s}$ for polarization).

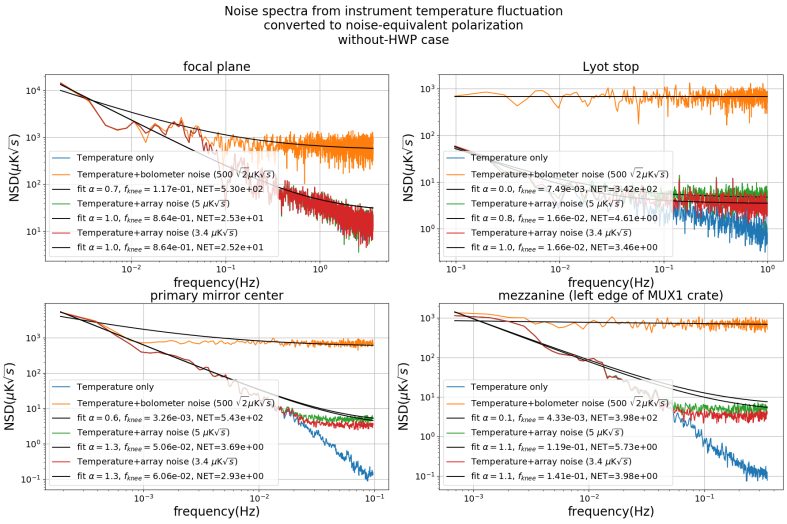

Figure 7.3: Noise spectral density (NSD) of the temperature of six components converged to signal fluctuation by temperature coefficients without HWP. Detector noise for polarization is added to the converged temperature noise. Blue lines are temperature only, orange lines are with single TES noise, green lines are with PB2 array noise, and red lines are with Simons Array. (*top left*) Focal plane, (*top right*) Lyot stop, (*bottom left*) average of 4 thermometers at the center of the primary mirror, (*bottom right*) mezzanine board.

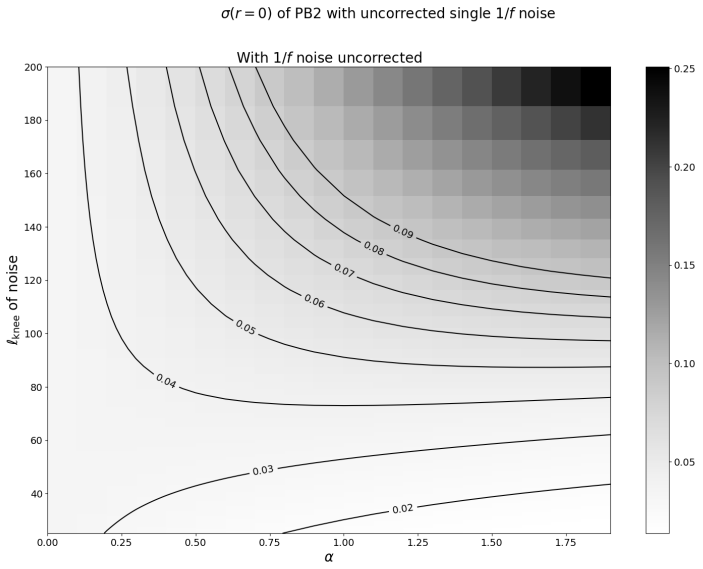

Figure 7.4: Forecasts of $\sigma(r = 0)$ with POLARBEAR-2 when the temperature fluctuation of single component is added as $1/f$ noise and is uncorrected.

replaced the noise level in the correction range to $\sqrt{2}$NEPol to determine N_ℓ, and calculated $\sigma(r = 0)$. Fig. 7.4 shows contribution of α and $\ell_{\rm knee}$ to the $\sigma(r = 0)$ when the correction is not performed. In Fig. 7.5, we show the impact of ℓ_c with the correction in case of having higher-sampling temperature monitors. In the situation that most of temperature fluctuations have their $\ell_{\rm knee}$ at order of ten, the variation of α does not contribute to $\sigma(r = 0)$ significantly. We can confirm our initial motivation that the noise reduction up to $\ell \sim 100$, where the bump of inflationary B-mode is lying, significantly contributes to the constraint of r.

Finally, we discuss the contribution of multiple noise sources. We corrected some of the reconstructed temperature noise spectra and added them to the detector array's white noise. Only the Lyot stop temperature was not corrected because its fluctuation was lower than our correction level at every frequency in $25 \leq \ell \leq 2500$. Note that the sky radiation fluctuation is added as another $1/f$ noise source in the case without HWP. It is modeled by the data from POLARBEAR as [39]

$$\mathrm{NSD}^2_{\rm sky} = \left[23\ \mu\mathrm{K}\sqrt{s} \left\{ \frac{1}{2} \left(\frac{\ell}{\ell_Q} \right)^{-\alpha_{\rm sky}} + \frac{1}{2} \left(\frac{\ell}{\ell_U} \right)^{-\alpha_{\rm sky}} \right\} \right]^2 , \tag{7.9}$$

where ℓ_Q and ℓ_U are knee frequency in the real and imaginary part of the signal, and $\alpha_{\rm sky} = 2$. This noise is added to NSD^2 when there is no HWP. The shape of noise spectra and $\sigma(r = 0)$ after correction are shown in

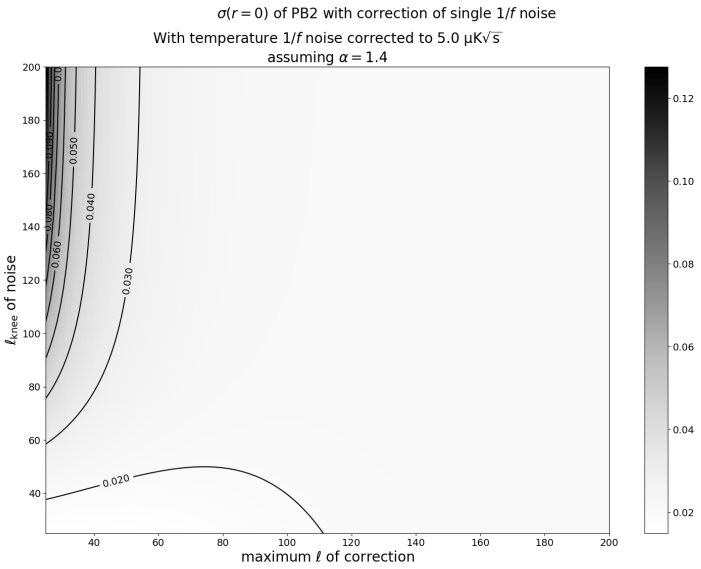

Figure 7.5: Forecasts of $\sigma(r = 0)$ with POLARBEAR-2 when the temperature fluctuation of single component is corrected to 5 $\mu\mathrm{K}\sqrt{\mathrm{s}}$ level at frequency below ℓ_c. The power law of $1/f$ noise is fixed to $\alpha = 1.4$.

Fig. 7.6. Due to the focal plane's huge temperature coefficient, the $\sigma(r = 0)$ became much larger than the latest constraint from CMB experiments. We could correct such large fluctuation by conventional polynomial fitting, but our correction based on monitoring data has an advantage in temperature resolution and component separation.

If we use a half-wave plate, temperature coefficients become much smaller so that the $\sigma(r)$ should be improved. We show the total noise spectra of temperature fluctuation plus detector noise for the with-HWP case in Fig. 7.7. We converged the temperature fluctuation to signal fluctuation by the temperature coefficients of the with-HWP case shown in Table. 4.3 and added polarization white noise of detectors. The instruments' contributions except for the readout electronics become below white noise in the range of $\ell \geq 25$. Correction for multiple sources is shown in Fig. 7.8. The focal plane only remains above white noise, and even a contribution of the focal plane becomes negligible.

7.3 Forecast for more sensitive experiments

Here we discuss the case of applying a better temperature monitoring system to a more sensitive experiment. Our temperature monitoring systems for warm instruments have a lower noise level than assumed above. As we saw

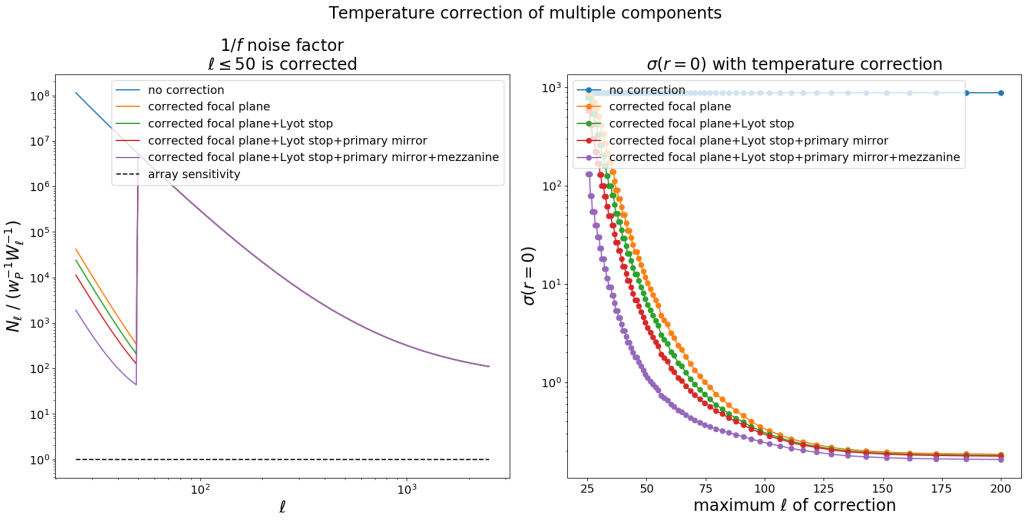

Figure 7.6: Correction of multiple temperature noise sources with POLARBEAR-2 without HWP. Only components exceeding the array sensitivity are shown. (*left*) Illustration of noise spectra normalized by white noise of long term observation, $w_P^{-1}W_\ell^{-1}$. (*right*) $\sigma(r = 0)$ after correction of each temperature noise of four instruments. Lyot stop was not corrected because of its small fluctuation.

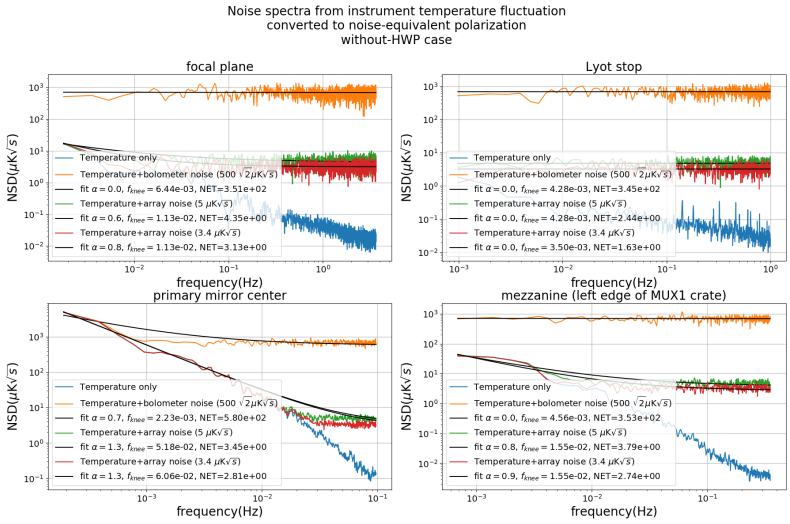

Figure 7.7: Noise spectral density (NSD) of the temperature of six components converged to signal fluctuation by temperature coefficients with HWP. Detector noise for polarization is added to the converged temperature noise. Blue lines are temperature only, orange lines are with single TES noise, green lines are with PB2 array noise, and red lines are with Simons Array. (*top left*) Focal plane, (*top right*) Lyot stop, (*bottom left*) average of 4 thermometers at the center of the primary mirror, (*bottom right*) mezzanine board.

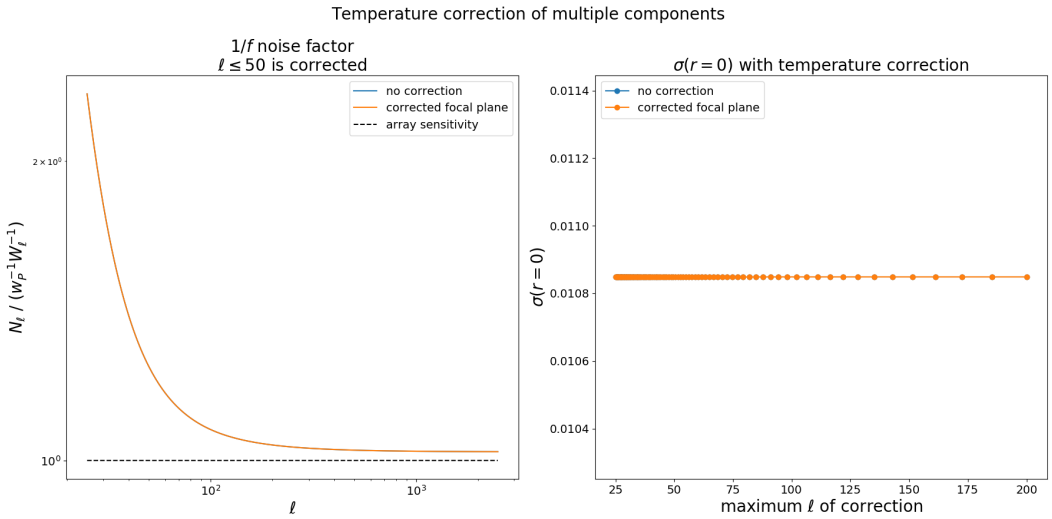

Figure 7.8: Correction of multiple temperature noise sources at 5 μK$\sqrt{\text{s}}$ precision with POLARBEAR-2 with HWP. (*left*) Illustration of noise spectra normalized by white noise of long-term observation, $w_P^{-1}W_\ell^{-1}$. (*right*) $\sigma(r = 0)$ after correction of each temperature noise of four instruments. No Lyot stop correction is applied because of its small fluctuation.

in Sec. 5.5, the temperature noise of the primary mirror at night is below 1 μK$\sqrt{\text{s}}$ and the sampling rate is around 10 sec, corresponding to $\ell \sim 90$. Forecasts of $\sigma(r = 0)$ with POLARBEAR-2, without- and with HWP, after correction to 1 μK$\sqrt{\text{s}}$ noise level are shown in Fig. 7.9 and Fig. 7.10. Suppose we assume that we corrected the focal plane's temperature fluctuation by a conservative polynomial fitting and others by temperature monitoring data with $\ell_c = 90$. In that case, the temperature correction in the without-HWP case reduces $\sigma(r = 0)$ from 0.4 to 0.04.

In the with-HWP case, correction of the primary mirror's temperature reduces $\sigma(r = 0)$ from 0.011 to 0.009. This forecast suggests that the temperature correction can greatly impact when combined with an HWP and targets to explore the $r \sim 0.001$ region.

Simons Array is designed to have much better sensitivity and aims to search r with $\sigma(r)$=0.006. We show a forecast of $\sigma(r = 0)$ with a single $1/f$ noise in Fig. 7.11. The impact of correcting temperature fluctuation from a single source is shown in Fig. 7.12. Improvement by correcting multiple sources is shown in Fig. 7.13 and Fig. 7.14, respectively for the without- and with-HWP case. With a HWP, temperature correction improves sensitivity from 0.0048 to 0.0035.

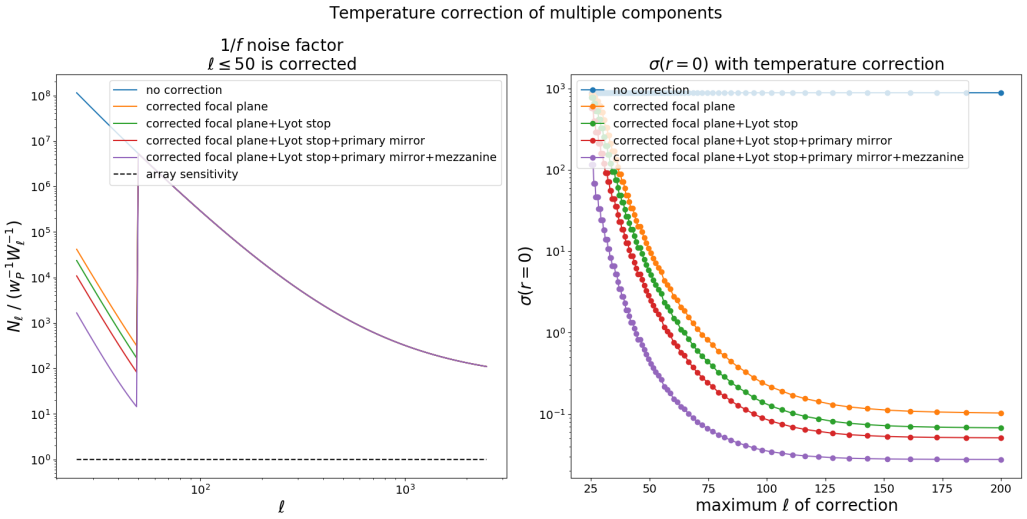

Figure 7.9: Correction of multiple temperature noise sources at 1 μK$\sqrt{\text{s}}$ precision with POLARBEAR-2 without HWP. (*left*) Illustration of noise spectra normalized by white noise of long-term observation, $w_P^{-1}W_\ell^{-1}$. (*right*) $\sigma(r = 0)$ after correction of each temperature noise of four instruments. Lyot stop was not corrected because of its small fluctuation.

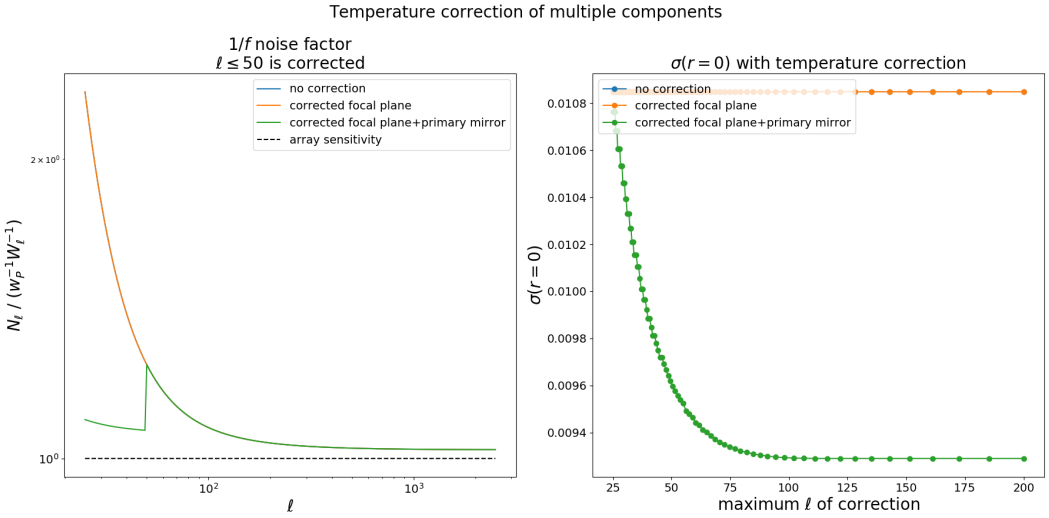

Figure 7.10: Correction of multiple temperature noise sources at 1 μK$\sqrt{\text{s}}$ precision with POLARBEAR-2 with HWP. (*left*) Illustration of noise spectra normalized by white noise of long-term observation, $w_P^{-1}W_\ell^{-1}$. (*right*) $\sigma(r = 0)$ after correction of each temperature noise of four instruments. Lyot stop was not corrected because of its small fluctuation.

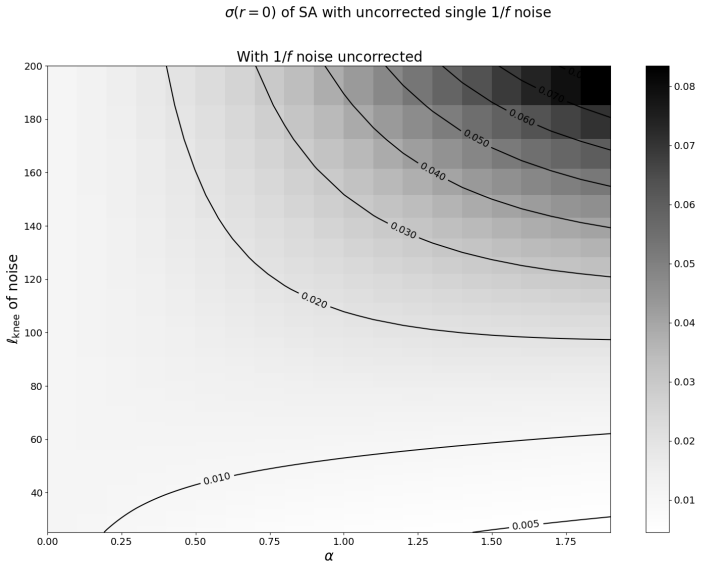

Figure 7.11: Forecasts of $\sigma(r = 0)$ with Simons Array when the temperature fluctuation of single component is added as $1/f$ noise and is uncorrected.

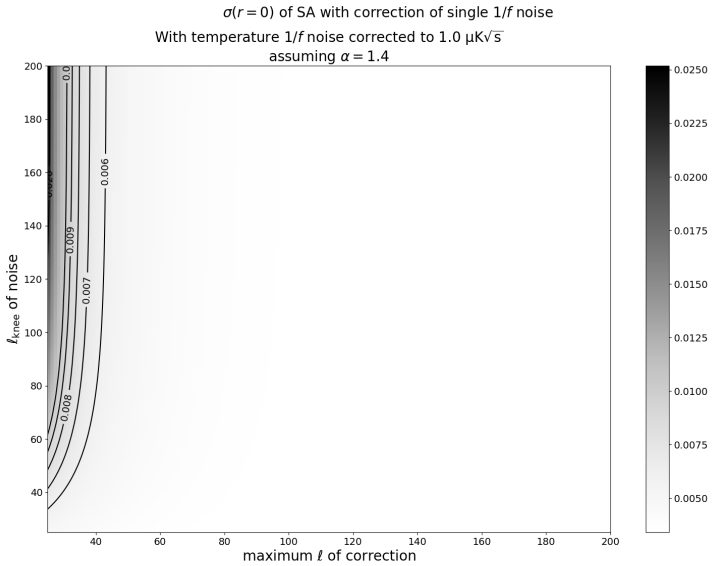

Figure 7.12: Forecasts of $\sigma(r = 0)$ with Simons Array when the temperature fluctuation of single component is corrected to 1 $\mu\mathrm{K}\sqrt{\mathrm{s}}$ level at frequency below ℓ_c. The power law of $1/f$ noise is fixed to $\alpha = 1.4$.

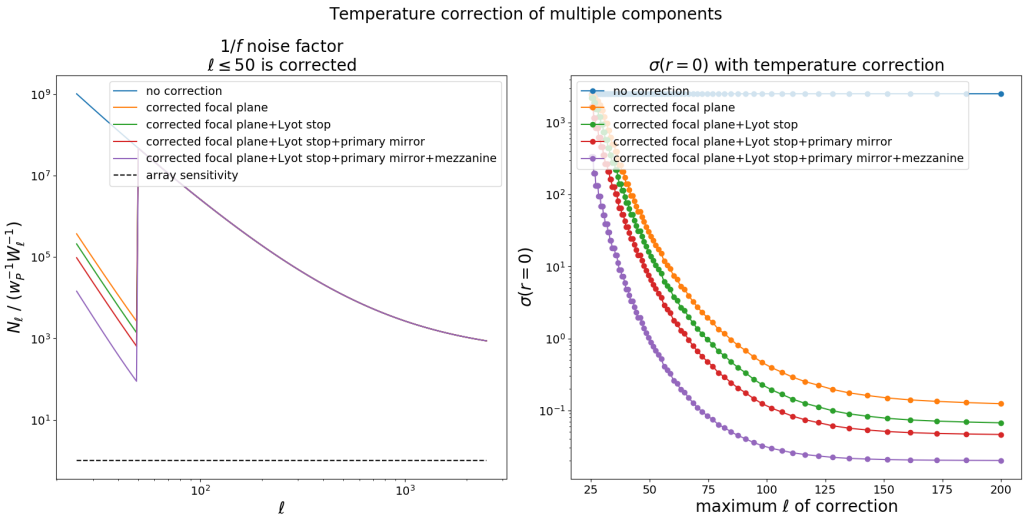

Figure 7.13: Correction of multiple temperature noise sources at 1 μK$\sqrt{\text{s}}$ precision with Simons Array without HWP. (*left*) Illustration of noise spectra normalized by white noise of long-term observation, $w_P^{-1}W_\ell^{-1}$. (*right*) $\sigma(r = 0)$ after correction of each temperature noise of four instruments. Lyot stop was not corrected because of its small fluctuation.

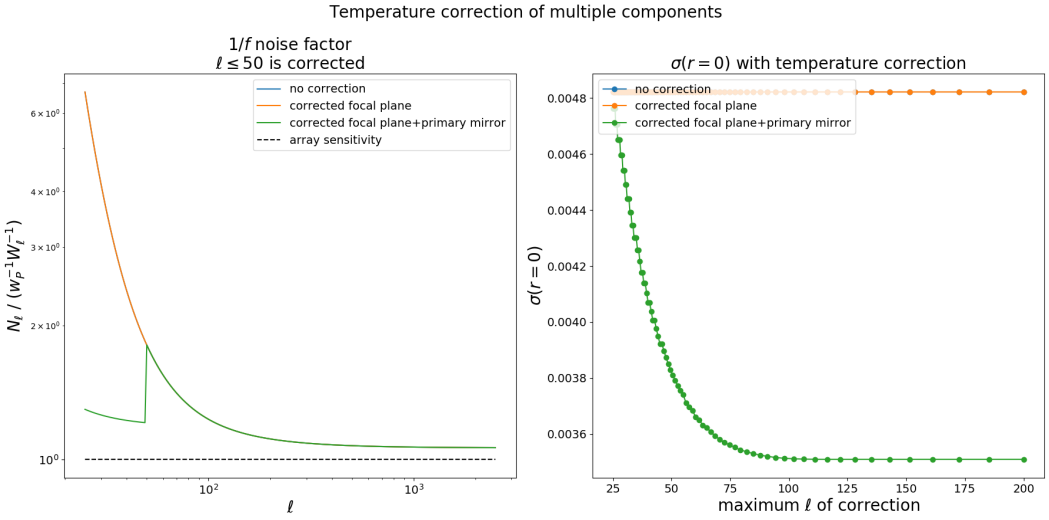

Figure 7.14: Correction of multiple temperature noise sources at 1 μK$\sqrt{\text{s}}$ precision with Simons Array with HWP. (*left*) Illustration of noise spectra normalized by white noise of long-term observation, $w_P^{-1}W_\ell^{-1}$. (*right*) $\sigma(r = 0)$ after correction of each temperature noise of four instruments. Lyot stop was not corrected because of its small fluctuation.

7.4 Summary of forecasts

We evaluated systematic errors in $\sigma(r = 0)$ originated from the uncertainty of temperature fluctuation measurement. The systematics related to the readout electronics are sufficiently small to perform temperature correction to achieve better sensitivity. However, in an experiment with a more sensitive array, the systematics from temperature distribution in the readout crate becomes non-negligible. Solutions to compensate for this systematics are to model the temperature distribution or investigate how to attach thermometers closer to the board with a guarantee not to cause short. For a future project, it is also effective to improve the precision of the built-in temperature sensor on the board.

On the other hand, We found large systematics raised from the distance between thermometers and target instruments, particularly for the mirror. Temperature correction must compensate these systematics by both of (1) modeling the temperature conduction from the front surface to thermometers on the back and (2) applying different temperature TOD to individual TES based on temperature gradient maps and the location on the mirror to where each TES illuminates. Although we cannot attach thermometers larger than the wavelength of the CMB on the front surface of the mirror, it is worth thinking to embed thermometers in a mirror for a future experiment.

8

Summary

We evaluated the effects of temperature fluctuation in the POLARBEAR-2 experiment. We pointed out that the mirrors and the readout electronics at ambient temperature become a non-negligible source of $1/f$ noise in the next-generation CMB experiments. Then we developed a temperature monitoring system for warm instruments with the lowest noise level among what has been reported by present radio-astronomical experiments. We presented a method for signal correction using temperature data monitored continuously in parallel with science observations.

To find evidence for the cosmic inflation beyond the current constraint by measurements of B-mode polarization of the CMB, we need to mitigate $1/f$ noise that increases at frequencies lower than typically 0.1 Hz. We focused on the temperature fluctuation of the instruments as sources of $1/f$ noise. The temperature fluctuation of an instrument modulates the detector signal by a specific coefficient. We evaluated the temperature coefficients of the focal plane, Lyot stop, primary mirror, and readout electronics by calculating and measuring the cases with- and without a half-wave plate (HWP). Comparing the temperature coefficient with the designed array sensitivity of POLARBEAR-2, we calculated requirements for temperature fluctuation in terms of noise spectral density at 50 mHz. The requirements for the primary mirror and the readout electronics were 15 mK$\sqrt{s}$ and 9 mK$\sqrt{s}$, respectively in the without-HWP case. Since their temperature fluctuations at the site exceed these values, they induce noise larger than the array sensitivity, although they were negligible in previous experiments. We suggested monitoring their temperature with sufficient precision during observation and correcting relative fluctuation of signal in the off-line analysis.

To correct temperature fluctuation of warm instruments, we constructed temperature monitoring systems whose measurement noise is below the requirement derived above. We focused on relative fluctuation instead of absolute temperature to achieve measurement noise below 10 mK$\sqrt{s}$. We chose commercially available products to build the monitoring systems so

that other next-generation CMB experiments can adopt our systems quickly. For the mirrors, we selected Keysight 34980A digital multimeter and 34925A opt-isolator. On the other hand, we chose the LTC2983 temperature measurement system for the readout electronics for its compactness in RF shielding. We compared the sensitivities of four types of thermometers and selected thermistors. We measured temperature noise, which is the summation of temperature fluctuation and measurement noise, of the combinations of thermistors and measurement devices above and confirmed it was below 1 mK$\sqrt{s}$.

We installed our system to the telescope at the observational site of POLARBEAR-2. We attached 12 thermistors on each of two mirrors and two on each of two crates of readout electronics. We applied windproof and sun-shading to the thermometers to mitigate temperature fluctuation and systematic error caused by the mirrors' thickness. We achieved temperature noise below 1 mK$\sqrt{s}$ on the primary mirror at night, which is the lowest level among all reported ambient temperature monitoring systems from radio-astronomical experiments. We evaluated systematic errors of temperature measurement, including calibration error of thermometers, reading uncertainty of measurement devices, the resistance of lead wires, self-heat dissipation of thermistors, temperature difference between back and front of the mirror, and temperature distribution in crates of the readout electronics.

We then demonstrated signal correction using the mezzanine board's temperature data, a part of the readout electronics. We prepared a sample TOD whose other drift sources were canceled by taking the difference of two groups of readout boards. We converged temperature fluctuation into the detector signal unit by multiplying the measured temperature coefficient, and we subtracted it from the signal. With this correction, the low-frequency noise below 4 mHz was reduced by factor of two. We also estimated the systematic error induced by the misestimation of the temperature coefficient. Briefly within -100%$\sim$80% of the true value is required to the accuracy of coefficient in order not to add bias larger than the temperature fluctuation. If we determine the coefficient with accuracy of 2.5% for the readout or 6.5% for the primary mirror, we can suppress the bias of correction below the array sensitivity.

Finally, we calculated statistical uncertainty of tensor-to-scalar ratio r, a parameter that characterizes theoretical models of the inflation, with corrected noise spectra. When $1/f$ noise from a single source is added to the array white noise, the statistical uncertainty $\sigma(r = 0)$ degrades from the designed value of 0.01 to 0.03 or more. Furthermore, when we add contributions from four sources, i.e. the sky radiation, the Lyot stop, primary mirror, and readout electronics, $\sigma(r = 0)$ becomes 0.4. Here we used measured $1/f$ parameters for the estimation and apply no temperature corrections. We can reduce the uncertainty to 0.04 if we perform temperature correction that makes signal fluctuation due to temperature fluctuation below 50 mHz

down to the equal level to the array sensitivity of POLARBEAR-2. With a half-wave plate, we can reach to 0.009. We concluded that a HWP to mitigate the sky fluctuation and temperature monitor to correct the instrumental noise have a great synergy. If we perform correction with 1 $\mu\mathrm{K}\sqrt{\mathrm{s}}$ precision for Simons Array, which is an upgrade of POLARBEAR-2, the $\sigma(r = 0)$ becomes 0.0035. This level is sufficient for ruling out many single-field models with large field variations. These results support that warm instruments' temperature fluctuation becomes an apparent noise source for today's CMB experiment, and temperature correction with precise monitors is an effective solution to mitigate the $1/f$ noise.

Bibliography

[1] D. J. Fixsen et al. Cosmic microwave background dipole spectrum measured by the COBE FIRAS. *Astrophys. J.*, 420:445, 1994.

[2] Eiichiro Komatsu. *Cosmic Microwave Background Radiation.* Nippon Hyoron Sha co.,Ltd, 2018.

[3] Yoshiki Akiba. Development of TES bolometer evaluation system for POLARBEAR-2, 2015. Master's thesis, Graduate University for Advanced Studies.

[4] R. Adam, P. A. R. Ade, N. Aghanim, et al. Planck 2015 results i. overview of products and scientific results. *Astronomy and Astrophysics*, 594:A1, 2016.

[5] Shaul Hanany, Michael Niemack, and Lyman Page. CMB Telescopes and Optical Systems. 2012.

[6] Sean McHugh, Benjamin A. Mazin, Bruno Serfass, et al. A readout for large arrays of Microwave Kinetic Inductance Detectors. *Rev. Sci. Instrum.*, 83:044702, 2012.

[7] P. A. R. Ade, Z. Ahmed, R. W. Aikin, and others. Constraints on primordial gravitational waves using planck, wmap, and new bicep2/keck observations through the 2015 season. *Physical Review Letters*, 121(22), Nov 2018.

[8] P. A. R. Ade et al. A Measurement of the Cosmic Microwave Background B-Mode Polarization Power Spectrum at Sub-Degree Scales from 2 years of POLARBEAR Data. 2017.

[9] J. Choi, H. Ishitsuka, S. Mima, S. Oguri, K. Takahashi, and O. Tajima. Radio-transparent multi-layer insulation for radiowave receivers. *Rev. Sci. Instrum.*, 84:114502, 2013.

[10] M. A. Dobbs, M. Lueker, K. A. Aird, and others. Frequency multiplexed superconducting quantum interference device readout of large bolometer arrays for cosmic microwave background measurements. *Review of Scientific Instruments*, 83(7):073113–073113–24, Jul 2012.

[11] P. A. R. Ade et al. Planck 2015 results. XIII. Cosmological parameters. *Astron. Astrophys.*, 594:A13, 2016.

[12] Z. Kermish et al. The POLARBEAR Experiment. *Proc. SPIE Int. Soc. Opt. Eng.*, 8452:1C, 2012.

[13] Y. Inoue et al. POLARBEAR-2: an instrument for CMB polarization measurements. *Proc. SPIE Int. Soc. Opt. Eng.*, 9914:99141I, 2016.

[14] A. Suzuki et al. The POLARBEAR-2 and the Simons Array Experiment. *J. Low. Temp. Phys.*, 184(3-4):805–810, 2016.

[15] D. Lyth and A. Liddle. *The primordial density perturbation.* Cambridge University Press, 2012.

[16] Robert M. Wald. *General relativity.* The University of Chicago Press, 1984.

[17] C. Dragone. A first-order treatment of aberrations in cassegrainian and gregorian antennas. *IEEE Transactions on Antennas and Propagation*, 30(3):331–339, May 1982.

[18] C. Dragone. First-order correction of aberrations in cassegrainian and gregorian antennas. *IEEE Transactions on Antennas and Propagation*, 31(5):764–775, September 1983.

[19] C. Dragone. Unique reflector arrangement with very wide field of view for multibeam antennas. *Electronics Letters*, 19(25):1061–1062, December 1983.

[20] W. A. Imbriale, J. Gundersen, and K. L. Thompson. The 1.4-m telescope for the q/u imaging experiment. *IEEE Transactions on Antennas and Propagation*, 59(6):1972–1980, June 2011.

[21] C. Bischoff, A. Brizius, I. Buder, et al. The q/u imaging experiment instrument. *The Astrophysical Journal*, 768(1):9, 2013.

[22] J. A. Chervenak, K. D. Irwin, E. N. Grossman, J. M. Martinis, C. D. Reintsema, and M. E. Huber. Superconducting multiplexer for arrays of transition edge sensors. *Appl. Phys. Lett.*, 74:4043, 1999.

[23] K. D. Irwin, M. D. Niemack, J Beyer, et al. Code-division multiplexing of superconducting transition-edge sensor arrays. *Superconductor Science and Technology*, 23(3):034004, 2010.

[24] Lloyd Knox. Determination of inflationary observables by cosmic microwave background anisotropy experiments. *Physical Review D*, 52(8):4307–4318, Oct 1995.

[25] Andrew H. Jaffe, Marc Kamionkowski, and Limin Wang. Polarization pursuers' guide. *Physical Review D*, 61(8), Mar 2000.

[26] Yuji Chinone. *Measurement of Cosmic Microwave Background Polarization Power Spectra at 43 GHz with Q/U Imaging ExperimenT*. PhD thesis, Tohoku University, 2010.

[27] Josquin Errard, Stephen M. Feeney, Hiranya V. Peiris, and Andrew H. Jaffe. Robust forecasts on fundamental physics from the foreground-obscured, gravitationally-lensed cmb polarization. *Journal of Cosmology and Astroparticle Physics*, 2016(03):052–052, Mar 2016.

[28] Arno A. Penzias and Robert Woodrow Wilson. A Measurement of excess antenna temperature at 4080-Mc/s. *Astrophys. J.*, 142:419–421, 1965.

[29] E. L. Wright et al. Interpretation of the Cosmic Microwave Background radiation anisotropy detected by the COBE differential microwave radiometer. *Astrophys. J.*, 396:L13–L18, 1992.

[30] J. M. Kovac, E. M. Leitch, C. Pryke, et al. Detection of polarization in the cosmic microwave background using DASI. *Nature*, 420:772–787, 12 2002.

[31] Mikhail M. Ivanov, Marko Simonović, and Matias Zaldarriaga. Cosmological parameters and neutrino masses from the final planck and full-shape boss data. *Physical Review D*, 101(8), Apr 2020.

[32] Aritoki Suzuki. *Multichroic Bolometric Detector Architecture for Cosmic Microwave Background Polarimetry Experiments*. PhD thesis, University of California, Berkeley, 2013.

[33] Satoru Takakura et al. Performance of a continuously rotating half-wave plate on the POLARBEAR telescope. *JCAP*, 1705(05):008, 2017.

[34] Yuki Inoue. *Development of POLARBEAR-2 receiver system for cosmic microwave background polarization experiment*. PhD thesis, Graduate University for Advanced Studies, 2016.

[35] Peter A. R. Ade, Pisano Giampaolo, Tucker Carole, and Weaver Samuel. A review of metal mesh filters, 2006.

[36] B. Westbrook, A. Cukierman, A. Lee, A. Suzuki, C. Raum, and W. Holzapfel. Development of the Next Generation of Multi-chroic Antenna-Coupled Transition Edge Sensor Detectors for CMB Polarimetry. *J. Low. Temp. Phys.*, 184(1-2):74–81, 2016.

[37] Tijmen de Haan, Graeme Smecher, and Matt Dobbs. Improved Performance of TES Bolometers using Digital Feedback. *Proc. SPIE Int. Soc. Opt. Eng.*, 8452:84520E, 2012.

[38] S. Adachi et al. A Measurement of the Degree Scale CMB B-mode Angular Power Spectrum with POLARBEAR. 10 2019.

[39] Satoru Takakura. *Characterization of a continuous polarization modulator using a half-wave plate for measurements of degree-scale cosmic microwave background with the POLARBEAR experiment.* PhD thesis, Osaka University, 2017.

[40] Joel N Ullom and Douglas A Bennett. Review of superconducting transition-edge sensors for x-ray and gamma-ray spectroscopy. *Superconductor Science and Technology*, 28(8):084003, 2015.

[41] K. Bandura, A. N. Bender, J. F. Cliche, et al. Ice: a scalable, low-cost fpga-based telescope signal processing and networking system, 2016.

[42] A. N. Bender, P. A. R. Ade, A. J. Anderson, et al. Integrated performance of a frequency domain multiplexing readout in the SPT-3G receiver. In Wayne S. Holland and Jonas Zmuidzinas, editors, *Millimeter, Submillimeter, and Far-Infrared Detectors and Instrumentation for Astronomy VIII*, volume 9914, pages 321 – 331. International Society for Optics and Photonics, SPIE, 2016.

[43] Author and J. Montgomery. personal communication, 2021.

[44] David J, Strozzi, and Kirk T. McDonald. Polarization dependence of emissivity, 2000.

[45] D. Barkats, C. Bischoff, P. Farese, et al. Cosmic microwave background polarimetry using correlation receivers with the pique and capmap experiments. *The Astrophysical Journal Supplement Series*, 159(1):1–26, Jul 2005.

[46] D. Barkats, C. Bischoff, P. Farese, and others. Cosmic microwave background polarimetry using correlation receivers with the PIQUE and CAPMAP experiments. *The Astrophysical Journal Supplement Series*, 159(1):1–26, jul 2005.

[47] P. D. Desai, H. M. James, and C. Y. Ho. Electrical resistivity of aluminum and manganese. *Journal of Physical and Chemical Reference Data*, 13(4):1131–1172, 1984.

[48] Daisuke Kaneko et al. Deployment of Polarbear-2A. *J. Low Temp. Phys.*, 199(3-4):1137–1147, 2020.

[49] B. Westbrook, P. A. R. Ade, M. Aguilar, and others. The polarbear-2 and simons array focal plane fabrication status. *Journal of Low Temperature Physics*, (5).

[50] Keysight Technologies. 34980a multifunction switch / measure unit | keysight, Viewed in 2021. https://www.keysight.com/en/pd-429828-pn-34980A/.

[51] Analog Devices. Ltc2983 datasheet and product info | analog devices, Viewed in 2021. https://www.analog.com/en/products/ltc2983.html.

[52] Littelfuse. Ps302j2 - ps series - interchangeable thermistors leaded thermistors - littelfuse, Viewed in 2021. https://www.littelfuse.co.jp/products/temperature-sensors/leaded-thermistors/interchangeable-thermistors/standard-precision-ps/ps302j2.

[53] TE Connectivity. Nb-ptco-011 : Meas rtd platinum thin film element | te connectivity, Viewed in 2021. https://www.te.com/usa-en/product-NB-PTCO-011.html.

[54] RS Components. Rs pro type t thermocouple, 0.3mm diameter, Viewed in 2021. https://jp.rs-online.com/web/p/thermocouples/6212209/.

[55] Maxim Integrated. Comparison of the ds18b20 and ds18s20 1-wire digital thermometers, Viewed in 2021. https://www.maximintegrated.com/jp/design/technical-documents/app-notes/4/4377.html.

[56] Inc. Lake Shore Cryotronics. Temperature sensor information, 2019. https://www.lakeshore.com/resources/sensors.

[57] Inc. Lake Shore Cryotronics. Model 218 temperature monitor, 2019. https://www.lakeshore.com/products/categories/overview/temperature-products/cryogenic-temperature-monitors/model-218-temperature-monitor.

[58] National Aeronautics and Space Administration. Lambda - camb web interface, 2019. https://lambda.gsfc.nasa.gov/toolbox/tb_camb_form.cfm.